Direct Numerical Simulations on the Development of Boundary Layer with Heat Transfer under the Effects of External and Internal Disturbances

by

XIA Shuang

Department of Mechanical Science and Engineering,
Graduate School of Engineering, Nagoya University

July, 2014

Contents

Nomenclature

C : The gap between the square bar and the bottom wall

C_f : Skin friction coefficient

C_p : Specific heat at a constant pressure

D : Thickness of the grid

d : Side length of the square bar

$E(k)$: Energy spectrum

H : Height of the computational domain

H_r : Height of the roughness

H_{12} : Shape factor

h : Heat transfer coefficient

k : Spanwise spacing between the small cubes

L_x, L_y, L_z : Computational domain size in the streamwise, wall-normal, and spanwise directions

L_∞ : Integral length of grid turbulence

M : Mesh size of the grid

N_x, N_y, N_z : Mesh number in the streamwise, wall-normal, and spanwise directions

P : Mean pressure

p : Instantaneous pressure

Pr : Prandtl number

Q : Second invariant of velocity gradient tensor

Q_S : Invariant of the rate-of-strain tensor

Q_W : Invariant of the rate-of-rotation tensor

Re_d : Reynolds number ($=U_\infty d/\nu$)

Re_H : Reynolds number ($=U_\infty H/\nu$)

Re_M : Reynolds number ($=U_\infty M/\nu$)

Re_x : Reynolds number ($=U_\infty x/\nu$)

Re_θ : Reynolds number ($=U_\infty \theta/\nu$)

St : Stanton number

S_{ij} : Rate-of-strain tensor

T : Instantaneous temperature

T_w : Wall temperature

T_∞ : Free-stream temperature

$\overline{T}$: Mean temperature

$T^{'}$: Temperature fluctuation

t : Time

t_a : Time-averaging period

Tu : Turbulence intensity of the grid turbulence

U : Mean streamwise velocity

U_C : Convective velocity

U_∞ : Free-stream velocity

u_i : Instantaneous velocity ($=(u,v,w)$)

$u_i^{'}$: Velocity fluctuation ($=(u^{'},v^{'},w^{'})$)

$u_{i,rms}^{'}$: Root-mean-square value of velocity fluctuation ($=(u_{rms}^{'},v_{rms}^{'},w_{rms}^{'})$)

u_τ : Friction velocity

W_{ij} : Fate-of-rotation tensor

x_i : Streamwise, wall-normal, and spanwise directions ($=(x,y,z)$)

Δ : Mesh spacing

Δt : Time step

Δx_i : Spatial resolution ($=(\Delta x, \Delta y, \Delta z)$)

δ	: Boundary layer thickness
δ^*	: Displacement thickness of the boundary layer
$\delta / \delta x_i$	: Finite difference operator
ε	: Dissipation rate of turbulent kinetic energy
ϕ	: Arbitrary variable
η	: Kolmogorov length scale
κ	: Thermal conductivity of the fluid
μ	: Dynamic viscosity of the fluid
ν	: Kinematic viscosity of the fluid
θ	: Momentum thickness of the boundary layer
ρ	: Density of the fluid
σ	: Blockage ratio of the grid
τ_w	: Wall shear stress
ω_z	: Instantaneous spanwise vorticity
$+$	: Normalized by wall units
$-$	: Time average
$'$	: Fluctuation

Chapter 1

Introduction

1.1 Background

A boundary layer is a very thin layer of fluid adjacent to a bounding surface where the effects of viscosity are significant and the velocity increases from zero at the surface and approaches the free-stream velocity at the edge. It is one of the canonical wall-bounded shear flows and exists widely in both nature and industry. The detailed flow structure in a pure boundary layer without any disturbance has been investigated over decades [1-8]. However, there are many situations in practice that the flow is unsteady and contains disturbances (hereafter referred to as the external disturbance in this thesis) or the surface is unsmooth and it significantly disturbs the flow (hereafter referred to as the internal disturbance in this thesis). This point is actually very important in a scalar field such as heat transfer across the surface. In heat exchangers, for instance, the flow is usually turbulent to modify the thermal boundary layer and affect heat transfer. Thus, from viewpoints of flow control and improvement in such engineering devices, it is of importance to clarify the effects of external and internal disturbances on a boundary layer with heat transfer. In particular, such disturbances significantly influence in the developing region of a boundary layer rather than in the developed region.

1.2 Boundary Layer Transition

Based on the characteristics of the environmental disturbances, transition of boundary layer from laminar to turbulence is classified into two scenarios. One is the natural transition, which is observed when the environmental disturbances are rather small. The other is the bypass transition, which is observed when the environmental disturbances (such as free-stream turbulence, surface roughness, etc.) are of high level.

1.2.1 Natural transition

Traditionally, the study of natural transition originates from the linear stability theory, describing the linear two-dimensional mode of disturbances to a viscous parallel flow by using the Orr-Sommerfeld equation. It is generally accepted that natural transition is connected with the growth of Tollminen-Schlichting (T-S) waves. When the T-S waves grow above a threshold amplitude (1% of the free-stream velocity), the flow in the boundary layer develops three-dimensional secondary instabilities and then breakdown to turbulence. Such growth of T-S waves is so weak that they typically attain the amplitude required for secondary instability to set in only when the Reynolds number, $Re_x = U_\infty x / \nu$, is of order 10^{6} [9] (U_∞ is the free-stream velocity, x is the streamwise distance away from the leading edge, and ν is the kinematic viscosity of the fluid). Two main modes of natural transition are known: the K-type transition proposed by Klebanoff et al. [10] and the N-type transition proposed by Knapp and Roache [11].

Figure 1.1 shows the schematic of K-type transition. The instability T-S waves are generated at a certain distance away from the leading edge. Then it propagates downstream, which are either amplified, and develops into three-dimensional secondary stabilities. Such structure is characterized by the spanwise alternating peaks and valleys, i.e. regions of enhanced and reduced amplitude. Rows of Λ-shaped vortices aligned in the streamwise direction, as shown in Fig. 1.2, develop simultaneously with the peaks and valleys. These Λ-shaped vortices lead to a localized high shear layers, followed by a sudden appearance of spikes which are multiplied, doubled and tripled in number. Finally, turbulent spots are formed and the flow transitions to turbulence. In the N-type transition scenario, on the other hand, the Λ-shaped vortices are observed in a staggered arrangement as shown in Fig. 1.3. No spikes are present. Comparing to the K-type scenario, the N-type scenario is likely to occur at lower initial amplitude of T-S waves. As T-S waves being amplified, three-dimensional secondary instabilities, characterized by the subharmonic disturbances, develop downstream. These subharminic disturbances are of half the frequency of the fundamental T-S waves, but of random amplitude and constant phase [11]. Consequently, staggered Λ-shaped vortices appear as the result of amplification of three-dimensional subhamonic disturbances. Finally, they break down into turbulence.
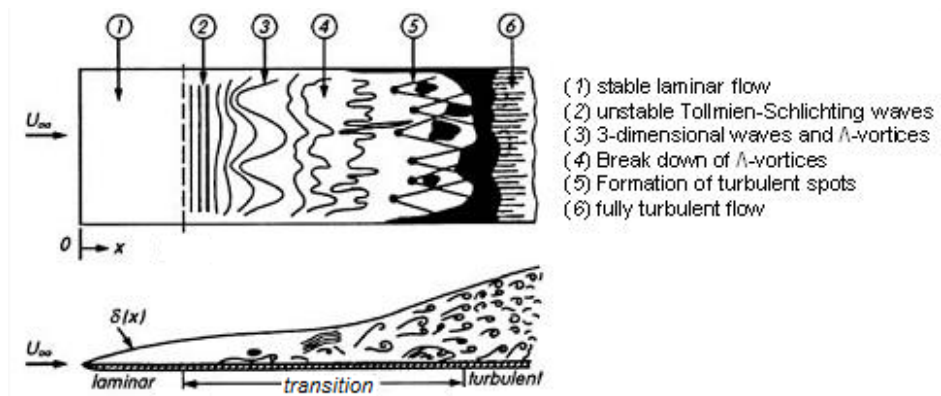
Fig. 1.1 Schematic of K-type transition [12]
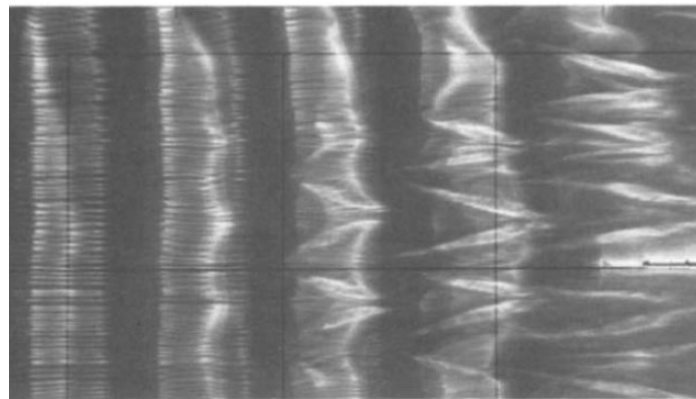
Fig. 1.2 Aligned Λ-shaped vortices [13]
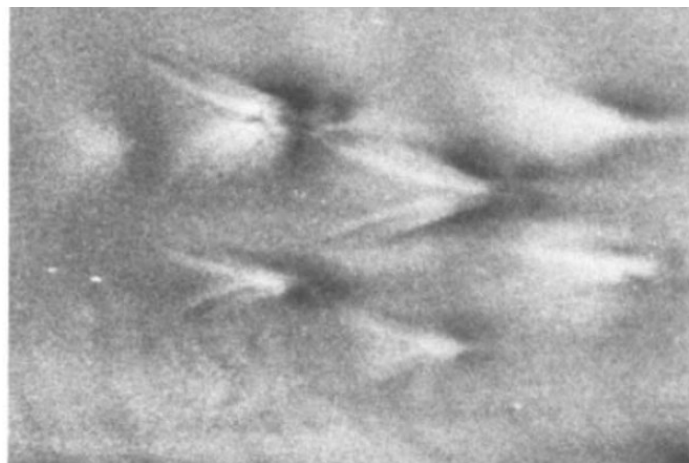
Fig. 1.3 Staggered Λ-shaped vortices [13]

1.2.2 Bypass transition

In many fluid flows, the transition of a boundary layer from laminar to turbulence is forced by free-stream disturbances, which is called bypass transition. In this case, the T-S waves observed in natural transition appear to be absent. Instead, it is characterized by the growth and breakdown of the streamwise elongated streaky structures with high and low streamwise velocity alternating in spanwise direction. An overall picture of the bypass transition is shown in Fig. 1.4. The contours correspond to the instantaneous streamwise velocity in a plane parallel to the wall. The flow is initially laminar and characterized by streamwise elongated streaks. Turbulent spots are observed downstream, followed by the fully developed turbulent boundary layer. Comparing to the natural transition, the bypass transition is more rapid, i.e. at a lower Reynolds number ($Re_x \sim 10^5$ [9]).

Among the numerous studies on the boundary layer transition, Klebanoff [15] was the first to identify the streamwise elongated streaky structures. Later, Kendall [16] denoted such structure as Klebanoff mode. Transient growth theory has been used with some success to describe the streak growth [16-19]. It shows that the growth of these streaks is proportional to the distance from the leading edge, or alternatively that the streamwise disturbance velocity increases as the square root of the distance from the leading edge. Note that the transient growth theory is linear, which can only describe the initial stage of transition. The latter stage must involve nonlinear effects [20].

As the streaks grow downstream, they become susceptive to the secondary instabilities developing on them. It is accepted that such instabilities are triggered by free-stream turbulence [21] or by streaks interactions [22]. Consequently, the streaks undergo wave motions and break down into turbulent spots. These spots appear at random location, grow in size and number and merge with each other until the flow is fully developed. In the literature, it is concluded that the streak breakdown is caused by one of two instability modes. The sinuous mode (Fig. 1.5), driven by streaks oscillations in the spanwise direction, is observed more frequently than the varicose mode (Fig. 1.6) which is caused by streaks oscillations in the wall-normal direction.
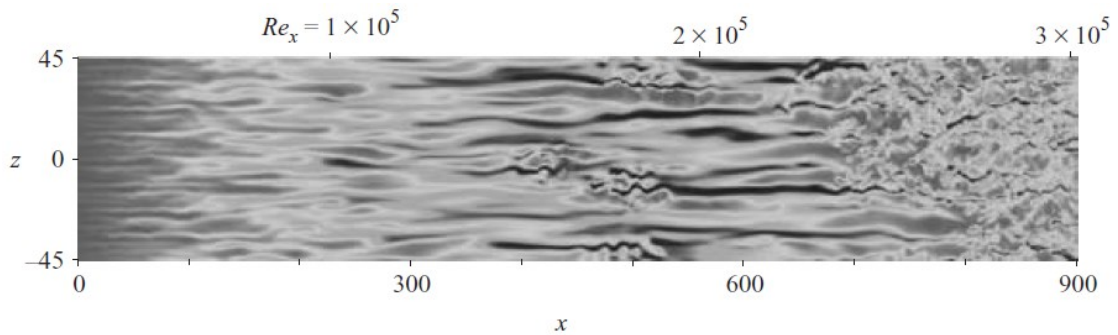
Fig. 1.4 Bypass transition [14]
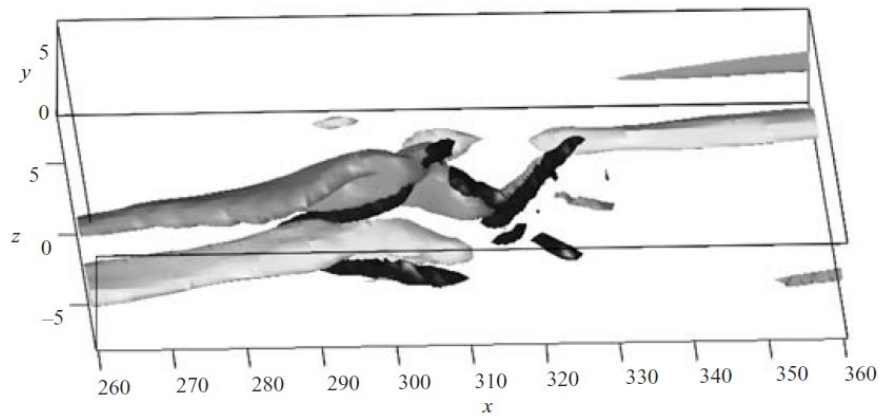
Fig. 1.5 Sinuous-like breakdown [14] (light grey: high-speed streaks;
dark grey: low-speed streaks; black: vortical structures)
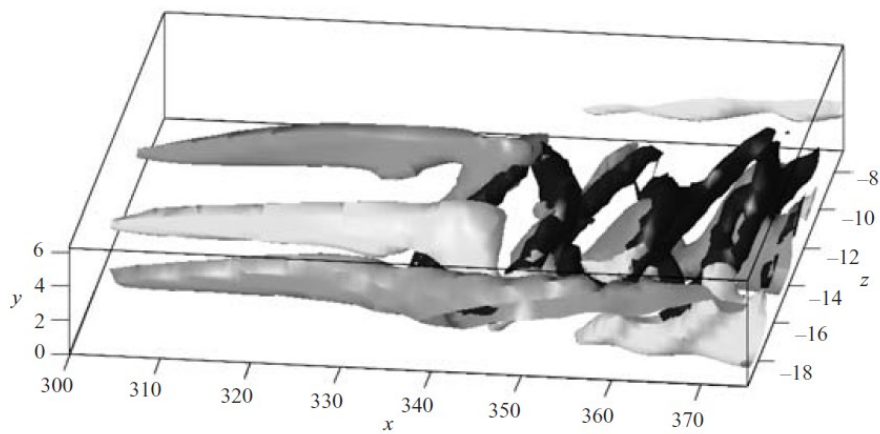
Fig. 1.6 Varicose-like breakdown [14] (light grey: high-speed streaks;
dark grey: low-speed streaks; black: vortical structures)

1.3 Turbulent Boundary Layer

Based on the distance away from the wall, a turbulent boundary layer (TBL) can be divided into several sublayers as shown in Table 1.1. Here, the wall-normal distance is normalized by either the wall units ($y^+ = yu_\tau/\nu$, where u_τ is the friction velocity) or the boundary layer thickness, δ. In the viscous sublayer, the flow is predominantly viscous and the effect of the Reynolds shear stress can be neglected. This leads to a linear distribution of the mean streamwise velocity along the wall-normal direction. The regions of low-speed streaks are observed in this sublayer. It is known that the mean spanwise spacing between these streaks is approximately 100 viscous lengths (ν/u_τ) up to Reynolds number of at least $Re_\theta \approx 6000$ [23-26]. In the log-law layer, however, the viscous effect is weak and the flow is dominated by Reynolds shear stress, leading to a log-law distribution of the mean streamwise velocity along the wall-normal direction. Between these two sublayers locates the buffer layer, where the viscous stress and Reynolds shear stress are of the same order of magnitude. Typically, the buffer layer is characterized by the intermittent bursting process, during which the low-speed fluid is ejected outward ($u < 0, v > 0$, where u and v are the streamwise and wall-normal velocity components) and the high-speed fluid is swept towards the wall ($u > 0, v < 0$), generating most of the turbulence production in the boundary layer [24][27-29]. On the other hand, in the outer region, the mean streamwise velocity distribution along the wall-normal direction obeys the defect law. A turbulent/nonturbulent interface is marked as the edge of the outer region from the free-stream.

Table 1.1 Different sublayers in a turbulent boundary layer

Sublayers		Range
Inner region	Viscous sublayer	$y^+ < 5$
	Buffer layer	$5 < y^+ < 30$
	Log-law layer	$30 < y^+ < 100$
Outer region		$y/\delta > 0.2$

In a turbulent boundary layer, the most striking structure is the coherent structures, describing the vortical structures which are robust in the sense that they retain their identity for many eddy-turn-over times and which appear again and again in more or less the same form [30]. The streamwise vortices, hairpin vortices, and packets of hairpins are the prevalent coherent structures in a turbulent boundary layer. They are relevant to the formation of the streaks and the bursting process mentioned above.

One of the first contributions to the issues of the existence of the coherent structures is due to Theodorsen [31] who introduce the hairpin vortex as shown in Fig. 1.7. In this model, vortical "tornadoes" form astride near-wall regions of low-speed fluid and grow outward with head inclined downstream 45°, and with spanwise dimensions proportional to the distance from the wall.
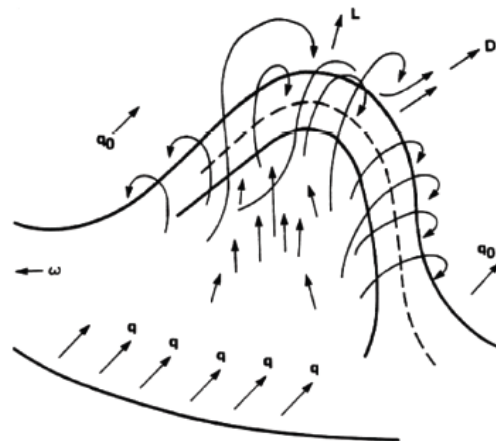
Fig. 1.7 Theodorson's description of a hairpin vortex [31]

It is concluded, by Kline at al. [24], that the formation of the streaks is the results of the streamwise vortices. As shown in Fig. 1.8, in the near-wall region, pairs of streamwise vortex rolls which are of opposite polarity are thought to be the dominate structure [30]. Accordingly, the fluid near the wall is swept horizontally towards the gap between the rolls and then pumped away from the wall. Owing to the effect of such flow motions, the spanwise vortices are compressed, indicating a reduction in streamwise velocity as shown in Fig. 1.9(a). Hence, the low-speed fluid near the wall is collected into a long streak, which is known as the low-speed streak. These streaks are eventually lifted up from the

wall once they get caught up in the updraft between the rolls, being followed by a sudden loss of stability and a breakup as shown in Fig. 1.9(b). The formation, oscillation and breakup of the low-speed streaks are identified as a bursting cycle.
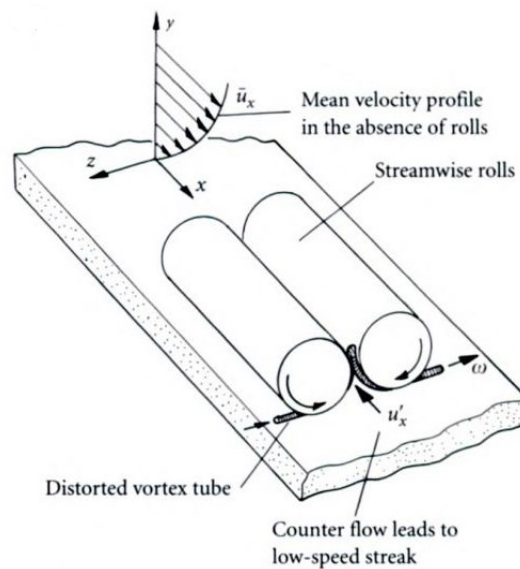
Fig. 1.8 A pair of streamwise vortex[30]
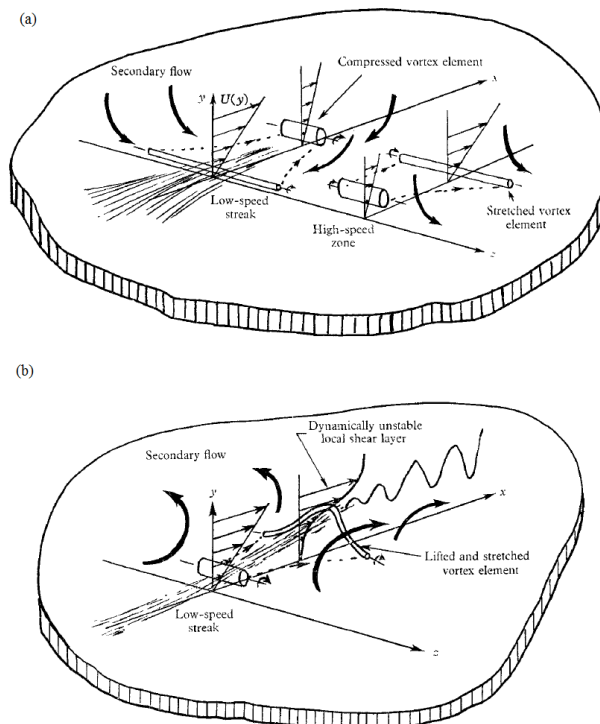
Fig. 1.9 (a) Formation of the streaks; (b) Breakup of the streaks [24]

A well-known description of hairpin vortex and its relation to the bursting cycle was proposed by Hinze [32] as shown in Fig. 1.10. A spanwise vortex is beginning to be formed locally at the wall. Then it is deformed by the flow into a more and more elongated hairpin vortex where the tip moves away from the wall. This gives rise to an outward flow between the legs of the hairpin vortex. At the same time, at distances $x_2^+ = x_2 u_\tau / v = 5 \sim 30$, an intense horizontal shear-layer is formed, showing up in the instantaneous streamwise velocity profile, i.e. U_1 profile, as a dent with inflection points. The resultant local instability and breakup of the flow surrounding the tip of the vortex produces a turbulent burst. Consequently, the blob of fluid of high turbulence intensity produced during the burst is convected in an accelerated way or swept in the downstream region.
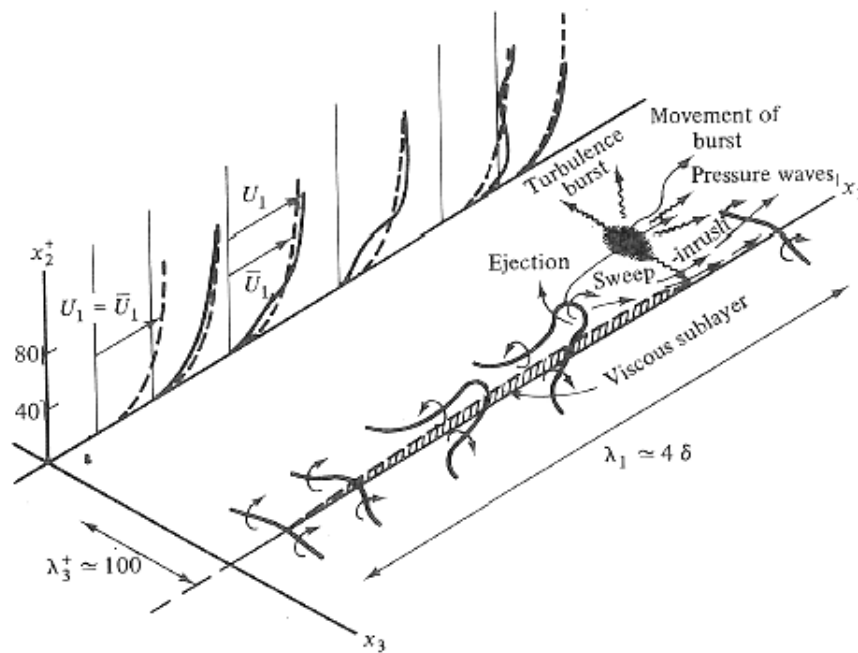
Fig. 1.10 The bursting cycle in a TBL with average spacing λ_1 and λ_3 [32]

A modernization of Theodorson's hairpin vortex was proposed by Adrian [5] as shown in Fig. 1.11. In this model, the hairpin vortex is attached to the wall, combining a horseshoe head with the legs of quasistreamwise vortices. Such vortex propagates in the direction of ejection ($u < 0, v > 0$), while the surrounding flow appears to be a sweep motion ($u > 0, v < 0$). The opposing ejection and sweep motions create the inclined shear layer.
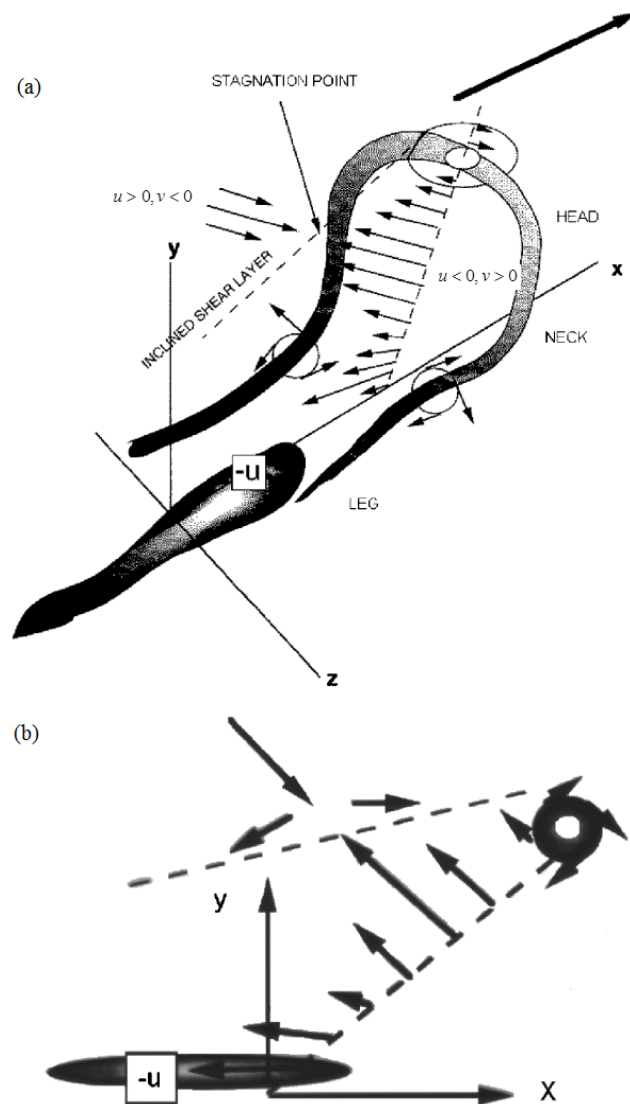
Fig. 1.11(a) Schematic of a hairpin vortex attached to the wall; (b) Hairpin vortex signature in the streamwise-wall-normal plane [5]

Sometimes the hairpin vortices appear in groups, which are called the hairpin vortex packets. An example of such packet was also proposed by Adrian [5] as shown in Fig. 1.12. The primary hairpin vortex (PHV) grows in all directions, and two new hairpin heads are formed: a downstream hairpin vortex (DHV) and a secondary hairpin vortex (SHV). The SHV generates another flow, leading to the formation of a tertiary hairpin vortex (THV). Note that the DHV appears to be detached from the wall.
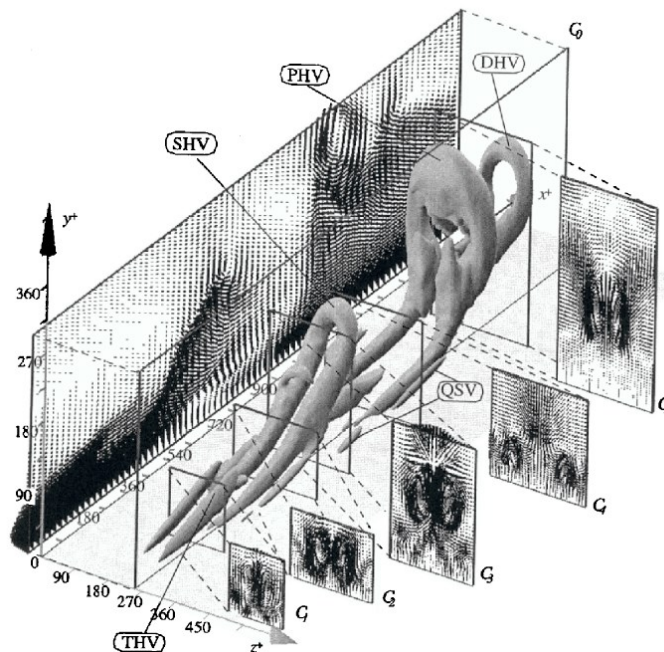
Fig. 1.12 Hairpin vortex packets [5]

1.4 Boundary Layer with Disturbances

1.4.1 Boundary layer under the effects of external disturbances

There are many studies on the effects of external disturbances on a boundary layer, including not only on a transitional boundary layer but also on a fully developed turbulent boundary layer (TBL). Among these studies, the external disturbance is mostly generated by a grid, i.e. grid-generated turbulence. It is nearly isotropic and homogeneous. Morkovin et al. [33] introduced a classical roadmap describing the transition scenarios of boundary layers subjected to the external disturbances. It is accepted that the transition process starts from the amplification of disturbances taken into a boundary layer through the receptivity

process. A detailed review on boundary layer receptivity to various external disturbances was summarized by Saric et al. [34]. Later, it was shown that the transition location in a boundary layer moves upstream with increasing the integral length scale [9][14] or the turbulence intensity of the grid turbulence [35]. Shahinfar and Fransson [36] found that the integral length scale has a relatively small influence on the transition location as compared to the turbulence intensity. Longer integral length scale advances the transition for low turbulence intensity cases, which is in agreement with previous studies [9][14], whereas it retards the transition for high turbulence intensity cases. On the other hand, the grid turbulence can also affect the structure of fully-developed boundary layers. It has been shown that the skin friction in a TBL is increased by the grid turbulence [37-38], but the effects on Reynolds shear stress are remained controversial. Charnay et al. [37] and Sharp et al. [39] found that the Reynolds shear stress in a fully developed TBL increases with the grid turbulence. However, studies by Hancock and Bradshaw [38] and Nagata et al. [40] showed that the Reynolds shear stress in a TBL is decreased by the grid turbulence.

Heat transfer in a boundary layer affected by the grid turbulence has also been investigated by several researchers. Most of the studies yielded consistent results in terms of observing an enhancement of heat transfer by the grid turbulence [40-45]. However, in some cases, the effects on mean temperature profile contradict. Péneau et al. [43] showed that the slope of the log-law region of mean temperature profile varies significantly with the turbulence intensity of the grid turbulence. However, in Li et al.'s study [45], such variation is not observed. Moreover, Maciejewski and Moffat [41-42] showed a unique behavior in mean temperature that not only the wake region but also the log-law region disappears under the effects of grid turbulence.

In addition to the grid turbulence, the effects of an external disturbance generated by a wake of an object placed in the free-stream on a boundary layer are also of interest over decades. Unlike the grid turbulence, such disturbances are anisotropic and often periodic in the near-wake region. Squire [46] summarized the studies on the wake-boundary layer interaction. He concluded that the upstream wake increase the overall turbulence level of the flow and thus advances the transition. As the object is placed closer to the surface, the interaction begins earlier. Later, Kyriakides et al. [47] performed experiments on boundary layer transition induced by a von Karman vortex street wake behind a cylinder. In their

study, two different transition mechanisms, known as strong-wake- and weak-wake-induced transitions, are found. It was established that the onset of the strong-wake-induced transition is a function of the free-stream velocity, the position of the cylinder with respect to the surface, the cylinder diameter, the drag coefficient and the minimum velocity in the developing wake at the onset location. Furthermore, the cylinder-wake-induced boundary layer transition at different cylinder Reynolds number was investigated by Ovchinnikov et al. [48] through numerical simulations. Rapid transition, which is somewhat similar to the bypass transition induced by the grid turbulence, is observed in higher Reynolds number cases. It is explained that the deformation of the formed spanwise rollers causes the injection of external wake momentum into the boundary layer. Such disturbances entering the boundary layer evolve into streaks of the streamwise velocity, which lead to transition to turbulence. On the other hand, Marumo et al. [49-50] carried out a set of experiments on a flat plate TBL disturbed by a cylinder wake and showed that the gap between the cylinder and the plate is a key parameter to describe the dependency of turbulence structure on the cylinder. Meanwhile, heat transfer is enhanced the most when the gap approaches the value of $0.5d$ (d is the cylinder diameter) and is less active when it exceeds the value of $0.75d$. Moreover, the cylinder wake reduces skin friction in the TBL with decreasing the gap. Further investigation by Suzuki et al. [51] has clarified that, when the gap is small, large dissimilarity between momentum and heat transfer in the TBL exists just behind the cylinder and it is caused by the intensification of the cold wall-wards and hot outwards interactions. Later, de Souza et al. [52] also experimentally investigated a TBL interacted with cylinder wakes. It is shown that the large coherent structures play a significant role in the variation of heat transfer and skin friction. In addition, Baskaran and Bradshaw [53] studied a TBL under the influence of wakes of circular and square bars with different sizes. Their results showed that there is no significant difference in skin friction under the influence of the circular bars with different sizes, but it is much smaller under the influence of the square bar. However, heat transfer is almost the same in all cases. Apart from bar wakes, the interaction between a wake of a thin flat plate and a TBL is also investigated by several researchers [54-56]. They generally show that skin friction and heat transfer in the TBL are sensitive to the setting of the plate, including not only the gap between the plate and the boundary layer but also the attack angle of the plate.

1.4.2 Boundary layer under the effects of internal disturbances

With respect to the effects of internal disturbances on a boundary layer, mounting tripping objects on the leading edge of a boundary layer is a conventional technique. Its main role is to create an initial disturbance which accelerates development to the TBL. Erm and Joubert [57] performed a set of experiments to investigate the effects of three types of tripping object (a wire, distributed grit, and cylinder pins) on a boundary layer. It is found that, in the early stage of the boundary layer development, the statistical quantities are different among the three tripping objects. However, their effects are quite small when the Reynolds number based on the momentum thickness approaches the value of $Re_\theta \approx 2175$ in the downstream region. Direct numerical simulations (DNSs) of the boundary layer were carried out by Rizzetta and Vibal [58] to investigate the effects of an array of cylindrical elements. They found that the boundary layer transitions from laminar to turbulence when the Reynolds number based on the size of the tripping elements exceeds a critical value. Later, Schlatter and Örlü [59] chose to model a real tripping object (roughness, vibrating ribbons, etc.) by using a trip forcing in their numerical simulations. In other words, the tripping is implemented as a weak random volume force acting in the wall-normal direction. The main inputs are the amplitude and the temporal frequency, which is associated with the height and the shedding characteristics of a real tripping object, respectively. Their results showed that the initiation of laminar-turbulent transition depends on the amplitude and the frequency of the tripping effects.

In addition, the effects of an internal disturbance generated by wall roughness on a TBL have been also investigated by several researchers. Previous studies were reviewed well by Raupach et al. [60]. This review supports the wall similarity hypothesis that turbulent motions outside the roughness sublayer of $y < 5H_r$ (H_r is the roughness height) are independent of the wall roughness and the interaction between the inner and outer layers is very weak at sufficiently large Reynolds number. However, some other experimental studies have shown disagreed results. Krogstad and Antonia [61] carried out experiments on a TBL over a wall roughened with periodically arranged rods in the streamwise direction. It showed that there is an increase in Reynolds stress profile in the outer layer. DNS of a TBL with the same roughness by Lee and Sung [62] also showed a lack of wall similarity.

1.5 Objective

From the former review on the research status of a boundary layer affected by various disturbances, it is known that detailed investigations have been focused on the flow fields in a boundary layer. The effects on the thermal field receive less scrutiny. Besides, the numerical studies on this subject are very limited. Compared with the experimental studies, numerical studies are quite useful since it can give more information of the boundary layer, especially in the near-wall region. Considering above, in the present study, a boundary layer with heat transfer under the effects of different disturbances is investigated by means of three-dimensional direct numerical simulation (DNS). Three types of disturbances which are common in both fundamental and applied applications are employed: a tripping object mounted on the wall, the grid turbulence, and a wake of a square bar. The aims of this research are as follows:

(1) To elucidate the effects of various disturbances on the development of a boundary layer.

(2) To elucidate the effects of various disturbances on the momentum and heat transfer in a boundary layer.

(3) To elucidate the contribution of vortical motions to heat transfer in a boundary layer.

(4) To provide a basis for flow control and heat transfer enhancement in a boundary layer by utilizing various disturbances.

1.6 Organization

This thesis is organized as follows. The background and objective of the study is introduced in the present chapter, Chapter 1. The details of numerical methods used in the present study are provided in Chapter 2. Chapters 3, 4, and 5 present the results and discussion on the three cases with various disturbances. Finally, the main conclusions are given in Chapter 6.

Chapter 2

Direct Numerical Simulation (DNS)

2.1 Introduction

With the development of the computer performances, numerical simulations play important roles in the study on a boundary layer. A numerical simulation allows us to investigate the whole flow field including the near-wall region that cannot be measured in the experiments. At present, three kinds of methods are mostly employed in numerical simulations. They are Reynolds-averaged Navier-Stokes equation simulation (RANS), large eddy simulation (LES) and direct numerical simulation (DNS). In RANS, the Reynolds-averaged Navier-Stokes equation is numerically solved. Owing to the closure problem caused by the term of Reynolds shear stress, turbulence models are needed. In LES, only the large energy-containing scales are solved, while modeling the influence of the small scales. DNS is considered to be the most accurate, where the Navier-Stokes (N-S) equations are numerically solved without any turbulence model. This requires, however, that the computational domain should be sufficiently large to contain the largest eddy and the computational mesh should be sufficiently fine to resolve the smallest eddy. The largest eddy is typically represented by the boundary layer thickness as for a boundary layer. On the other hand, the smallest eddy is usually the Kolmogorov length scale, $\eta = \left(v^3 / \varepsilon\right)^{1/4}$. Here, ε is the dissipation rate of turbulent kinetic energy. In the literature, ε peaks at the wall and reaches of the order of $0.2 u_\tau^4 / v$ [63]. It is, therefore, more convenient to use viscous length scale v / u_τ as the smallest scale. The basic calculation steps in DNS are shown in Fig. 2.1. The details of each calculation step will be discussed in the following sections.
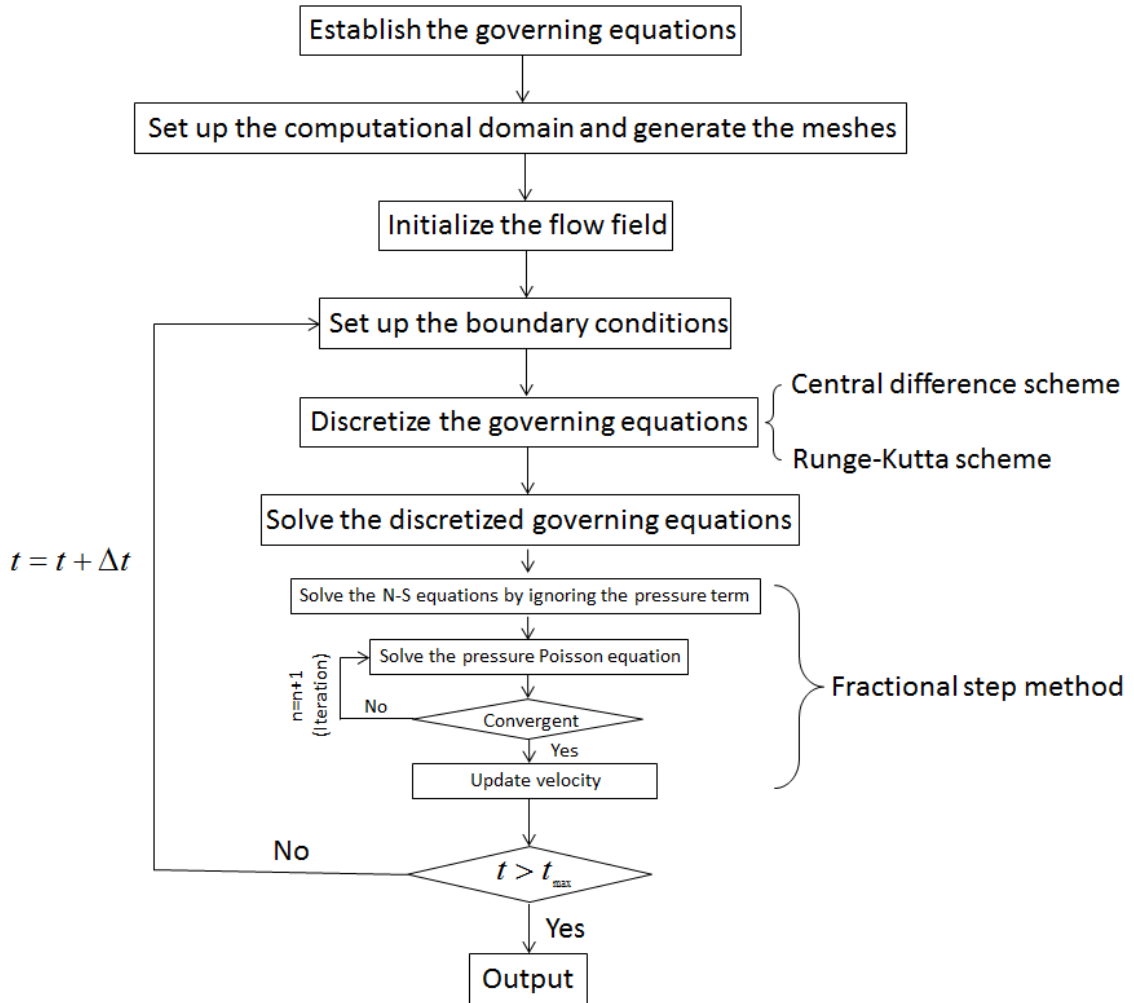
Fig. 2.1 A flow chart of calculation steps in DNS

2.2 Governing Equations and Numerical Algorithm

In current research, the governing equations are the continuity equation, Navier-Stokes equations for incompressible flows, and the scalar transfer equation:

$$\frac{\partial u_i}{\partial x_i} = 0 , \tag{2.1}$$

$$\frac{\partial u_i}{\partial t} + \frac{\partial}{\partial x_j}(u_i u_j) = -\frac{\partial p}{\partial x_i} + \frac{1}{Re}\frac{\partial^2 u_i}{\partial x_j \partial x_j} , \tag{2.2}$$

$$\frac{\partial T}{\partial t} + \frac{\partial}{\partial x_j}(T u_j) = \frac{1}{RePr}\frac{\partial^2 T}{\partial x_j \partial x_j} . \tag{2.3}$$

Here, all the variables are non-dimensionalized by a characteristic velocity, length scale and temperature. In this study, in the cases with a tripping object and the grid turbulence, the free-stream velocity, U_∞, the height of the computational domain, H, and the temperature difference between the free-stream and the wall, $T_\infty - T_w$ are used for the normalization, while the variables in the case with a wake of a square bar are normalized by the free-stream velocity, U_∞, the side length of the square bar, d, and the temperature difference between the free-stream and the wall, $T_\infty - T_w$.

A major difficulty in solving these governing equations is that the velocity and the pressure in Eq. (2.2) are coupled by the incompressibility constraint. To overcome this difficulty, the fractional step method in which the computations for velocity and pressure are decoupled is used in this study as well as many past studies. The details of the fractional step method are explained as follows:

Equation (2.2) can be rewritten as

$$\frac{u_i^{n+1} - u_i^n}{\Delta t} = -\frac{\partial}{\partial x_j}(u_i u_j)^n - \frac{\partial p^{n+1}}{\partial x_i} + \frac{1}{Re}\frac{\partial^2 u_i}{\partial x_j \partial x_j}^n . \tag{2.4}$$

By introducing an intermediate velocity, $\hat{u}_i^{n+1}$, Eq. (2.4) is divided into two parts:

$$\frac{\hat{u}_i^{n+1} - u_i^n}{\Delta t} = -\frac{\partial}{\partial x_j}(u_i u_j)^n + \frac{1}{Re}\frac{\partial^2 u_i}{\partial x_j \partial x_j}^n , \tag{2.5}$$

$$\frac{u_i^{n+1} - \hat{u}_i^{n+1}}{\Delta t} = -\frac{\partial p^{n+1}}{\partial x_i} . \tag{2.6}$$

Taking divergence of Eq. (2.6) and combining it with the continuity equation (Eq. (2.1)), we can obtain the following equation,

$$\frac{\partial^2 p^{n+1}}{\partial x_i \partial x_i} = \frac{1}{\Delta t} \frac{\partial \hat{u}_i^{n+1}}{\partial x_i} \quad , \tag{2.7}$$

which is called the pressure Poisson equation. At the first step of the fractional method, the intermediate velocity, $\hat{u}_i^{n+1}$, is solved through Eq. (2.5) by ignoring the pressure term and incompressibility. Then the pressure, p^{n+1}, is calculated by submitting $\hat{u}_i^{n+1}$ into Eq. (2.7). Finally, the velocity, u_i^{n+1}, is updated by submitting $\hat{u}_i^{n+1}$ and p^{n+1} into Eq. (2.6). Here, the pressure Poisson equation is acted as a projection operator, which projects the intermediate velocity into a divergence-free velocity field to get the next update of velocity and pressure.

2.3 Computational Mesh System

Convectional numerical algorithms based on a structure mesh mostly fall into two classes: regular and staggered mesh systems. In the regular mesh system, the velocity components and pressure are stored at the same point as shown in Fig. 2.2. The discretization of the continuity and momentum equation are centered at these points. In the staggered mesh system, on the other hand, pressure and scalars are stored at the center of the mesh while the velocity components are distributed around it as shown in Fig. 2.3. The continuity is centered at the pressure point and the momentum equation corresponding to velocity components is centered at the respective velocity points. Compared to the regular mesh system, the staggered mesh system has a great advantage of preventing spurious pressure oscillations. Hence, in my simulation, the staggered mesh system is adopted.
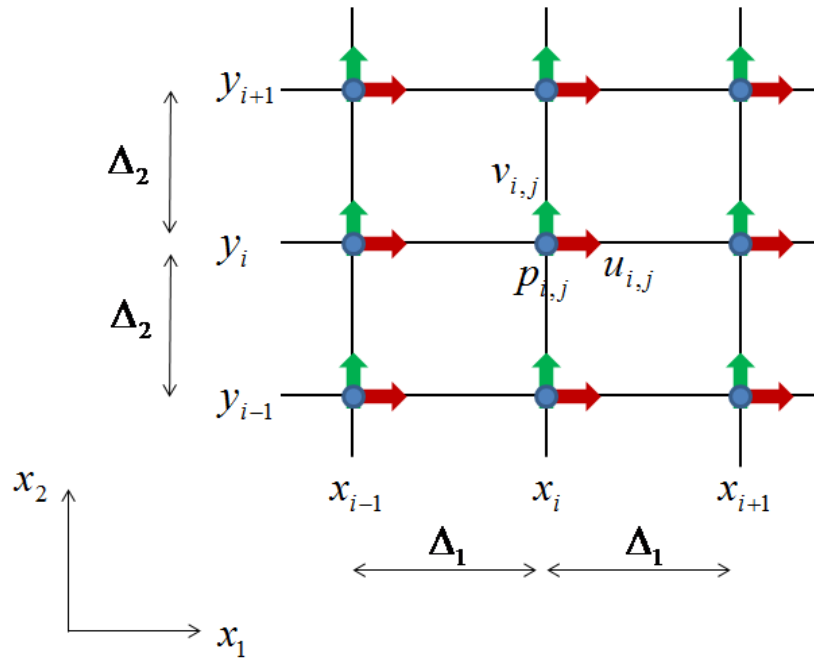
Fig. 2.2 Regular mesh system
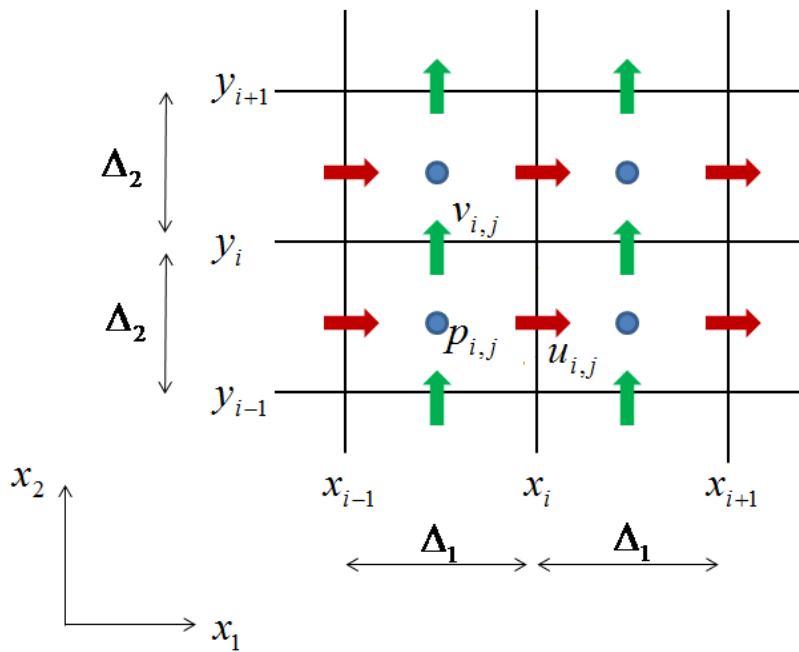
Fig. 2.3 Staggered mesh system

2.4 Spatial Discretization

In the early stage, spectral method is mostly used. Although it is of a high accuracy, the use of spectral method is limited to flows in a simple geometry and simple boundary conditions (e.g., periodic boundary conditions). As for a boundary layer, which is spatially developed in streamwise direction, the finite difference method is widely adopted. The main idea of the finite difference method is to approximate the derivative of the variable at one point as a linear combination of the variable value at different points, $f'_j = \sum_{i=1}^{n} a_i f_i$, or to approximate the linear combination of the derivative of the variable as a linear combination of the variable values at different points, $\sum_{j=1}^{n} b_j f'_j = \sum_{i=1}^{n} a_i f_i$. The former one includes the traditional forward, backward and central difference schemes (CDS), while the latter one is defined as the Padé scheme or compact scheme.

The fourth-order CDS using uniform mesh is expressed as [64]

$$f'_j = \frac{f_{j-2} - 8f_{j-1} + 8f_{j+1} - f_{j+2}}{12\Delta} , \tag{2.8}$$

where f is a variable, f' is the derivative of f , and Δ is the mesh spacing. In the present simulation, the viscous and diffusion terms (along the streamwise and wall-normal directions) in the governing equations are discretized by a second-order CDS as shown below:

$$f''_j = \frac{f_{j-1} - 2f_j + f_{j+1}}{\Delta^2} . \tag{2.9}$$

Here, f'' is the second derivative of f . With respect to the viscous and diffusion terms along the spanwise direction, a fourth-order CDS, as shown in Eq. (2.10), is adopted to increase the accuracy.

$$f''_j = \frac{f_{j-3} - 54f_{j-2} + 783f_{j-1} - 1460f_j + 783f_{j+1} - 54f_{j+2} + f_{j+3}}{(24\Delta)^2} . \tag{2.10}$$

The fourth-order Padé scheme using uniform mesh is expressed as [64]

$$f'_{j+1} + f'_{j-1} + 4f'_j = \frac{3}{\Delta}(f_{j+1} - f_{j-1}) . \tag{2.11}$$

Combining two additional equations at the boundary as shown in Eqs. (2.12) and (2.13),

Eq. (2.11) can be rewritten in term of a tridiagonal matrix which allows us to use a standard tridiagonal solver.

$$f_0' + 2f_1' = \frac{1}{\Delta}(-\frac{5}{2}f_0 + 2f_1 + \frac{1}{2}f_2) \tag{2.12}$$

$$f_n' + 2f_{n-1}' = \frac{1}{\Delta}(\frac{5}{2}f_n - 2f_{n-1} - \frac{1}{2}f_{n-2}) \tag{2.13}$$

In order to check the accuracy of Padé scheme, Eqs. (2.11), (2.12) and (2.13) are used to differentiate

$$f(x) = \sin 5x, \quad 0 \le x \le 3. \tag{2.14}$$

The result is plotted in Fig. 2.4. It is confirmed that, although relatively few mesh points are used, the Padé scheme is remarkably accurate.
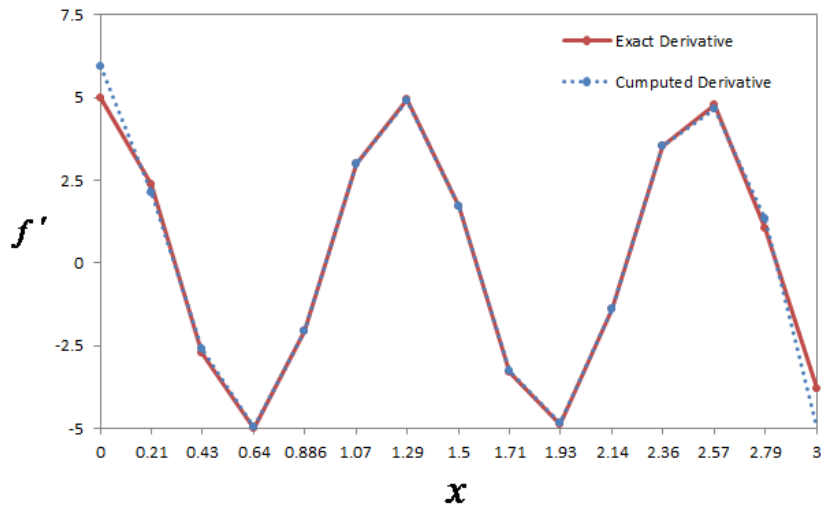
Fig. 2.4 Computed derivative by using a fourth-order Padé scheme

2.4.1 Central compact finite difference scheme

Based on the Padé scheme, Lele [65] proposed a central compact finite difference scheme (CCS) on a cell-centered mesh. Compared to the traditional finite schemes, it stays close to the exact value over a wider range of wavenumbers (spectral-like resolution). A fourth-order and eighth-order CCS on a cell-centered mesh is generally expressed as

$$\alpha f_{j+1}' + f_j' + \alpha f_{j-1}' = a \frac{f_{j+1/2} - f_{j-1/2}}{\Delta} + b \frac{f_{j+3/2} - f_{j-3/2}}{3\Delta} + c \frac{f_{j+5/2} - f_{j-5/2}}{5\Delta}. \tag{2.15}$$

Here, the coefficients are listed in Table 2.1. At the boundary, the following discretization is used:

$$\alpha f'_{j+1} + f'_j = a_0 \frac{f_{j+1/2} - f_{j-1/2}}{\Delta} \, .$$
(2.16)

Compared to the traditional compact schemes on a mesh node (e.g., Eq. (2.11)), the schemes on the cell-centered mesh have considerably lower differencing errors. Note that the second derivative of f can be calculated by using Eq. (2.15).

Table 2.1 Coefficients in CCS [65]

	CCS4	CCS8
α	$1/22$	$75/354$
a	$12/11$	$(37950 - 39275\alpha)/31368$
b	0	$(65115\alpha - 3550)/20912$
c	0	$(25699\alpha - 6114)/62736$
α_0	$23/22$	$-$

2.4.2 Fully conservative finite difference scheme

In numerical simulations, care must be taken on the discretization of the convective term (non-linear term) in Navier-Stokes equations, since it is the major source causing the numerical instability and is related to the conservation of kinetic energy. There are three forms for the convective term [66-67],

Divergence form: $\quad \dfrac{\partial}{\partial x_j}(u_i u_j)$,
(2.17)

Advective form/Gradient form: $\quad u_j \dfrac{\partial u_i}{\partial x_j}$,
(2.18)

Skew-symmetric form: $\quad \dfrac{1}{2}\dfrac{\partial}{\partial x_j}(u_i u_j) + \dfrac{1}{2}u_j\dfrac{\partial u_i}{\partial x_j}$.
(2.19)

It is known, from the study by Morinishi et al. [66], that the aliasing error that causes the numerical instability can be suppressed and the kinetic energy is conserved by using the

skew-symmetric form (Eq. (2.19)). Based on this, a fully conservative second-order finite difference scheme in a staggered mesh system was proposed [66],

$$\frac{1}{2}\frac{\delta \overline{u}_j^{x_i}\overline{u}_j^{x_j}}{\delta x_j} + \frac{1}{2}\overline{\overline{u}_j^{x_i}\frac{\delta u_i}{\delta x_j}}^{x_j} \; ,$$

(2.20)

where the finite difference operator is defined as

$$\left.\frac{\delta \phi}{\delta x_1}\right|_{x_1,x_2,x_3} = \frac{\phi(x_1 + \Delta_1/2, x_2, x_3) - \phi(x_1 - \Delta_1/2, x_2, x_3)}{\Delta_1} \; ,$$

(2.21)

and the interpolation operator is defined as

$$\left.\overline{\phi}^{x_1}\right|_{x_1,x_2,x_3} = \frac{\phi(x_1 + \Delta_1/2, x_2, x_3) + \phi(x_1 - \Delta_1/2, x_2, x_3)}{2} \; .$$

(2.22)

Here, Δ_1 is the mesh spacing in the x_1 direction as shown in Fig. 2.3. As mentioned above, the continuity equation is centered at the pressure point while the momentum equation is centered at the respective velocity points by using the staggered mesh system. Thus, the interpolation operation is acted to centralize them at the same point, i.e. at the pressure point. The present simulation was carried out based on this fully conservative finite difference scheme for the convective term.

2.5 Time Advancement

Basically, the schemes in time advancement can be classified as the explicit scheme and implicit scheme. Consider a first-order ordinary differential equation

$$y' = \frac{dy}{dt} = f(y,t), \quad y(t_0) = y_0 \; .$$

(2.23)

Two simplest forms of the explicit and implicit schemes for solving Eq. (2.23) are expressed as

$$y_{n+1} = y_n + \Delta t f(y_n, t_n) \; ,$$

(2.24)

$$y_{n+1} = y_n + \Delta t f(y_{n+1}, t_{n+1}) \; ,$$

(2.25)

where Δt is the time step. In using the explicit scheme (Eq. (2.24)), one simply starts from the initial condition and marches forward to obtain the final value. Contrary to the explicit scheme, the implicit scheme (Eq. (2.25)) does not allow us to easily obtain the solution at the next step. Figure 2.5 shows a comparison of solving the following ordinary

differential equation by using the explicit and implicit schemes with different time steps.

$$y' + 0.5y = 0, \quad y(0) = 1, \quad 0 \le t \le 20. \tag{2.26}$$

It is seen that the results become unstable by using the explicit scheme when the time step is large. On the other hand, the results are both stable and it gets closer to the exact value as decreasing the time step by using the implicit scheme, indicating that the implicit scheme has a better stability. By using the explicit scheme, one can solve the equation easily but much attention should be paid to the numerical stability. In the stability analysis, it is required that the Courant-Friedrichs-Lewy number, $CFL = u\Delta t/\Delta$, should be less than 1 to ensure the numerical stability for an explicit scheme. Here, Δ is the mesh spacing.
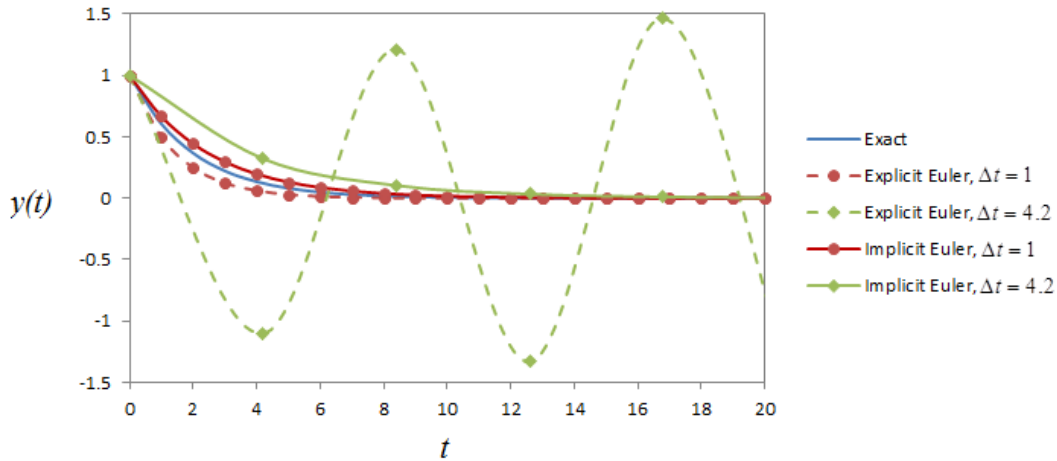
Fig. 2.5 The comparison of the explicit and implicit schemes

2.5.1 Crank-Nicolson scheme

It has been known that for a diffusion equation, the stability limits for explicit schemes are too stringent [64]. The implicit schemes are preferred. A popular implicit scheme is the Crank-Nicolson scheme, which is often called the trapezoidal scheme. A second-order Crank-Nicolson scheme is expressed as

$$y_{n+1} = y_n + \frac{\Delta t}{2}\left[f(y_{n+1}, t_{n+1}) + f(y_n, t_n)\right]. \tag{2.27}$$

This scheme is unconditionally stable. In the present simulation, the viscous and diffusion terms (along the wall-normal direction) are advanced by using the second-order Crank-Nicolson scheme.

2.5.2 Adams-Bashforth scheme

As one of the explicit schemes, Adams-Bashforth scheme is used in time advancement. It is also referred to as the multi-step scheme where the information from prior to step n is used. A second-order Adams-Bashforth scheme is expressed as

$$y_{n+1} = y_n + \Delta t \left[\frac{3}{2} f(y_n, t_n) - \frac{1}{2} f(y_{n-1}, t_{n-1}) \right]. \tag{2.28}$$

Although high accuracy is achieved because more information about f is provided, Adams-Bashforth scheme is not self-starting. Usually, another scheme such as the one shown in Eq. (2.24) is adopted to start the calculation for the first or first few time steps.

2.5.3 Runge-Kutta scheme

Runge-kutta scheme is widely used in numerical simulations since it has a higher accuracy and a better stability. By using this scheme, more points are introduced between t_n and t_{n+1}. A classical fourth-order Runge-Kutta scheme is expressed as

$$\left.\begin{aligned}
k_1 &= \Delta t f(y_n, t_n), \\
k_2 &= \Delta t f(y_n + \frac{k_1}{2}, t_n + \frac{\Delta t}{2}), \\
k_3 &= \Delta t f(y_n + \frac{k_2}{2}, t_n + \frac{\Delta t}{2}), \\
k_4 &= \Delta t f(y_n + k_3, t_n + \Delta t), \\
y_{n+1} &= y_n + \frac{k_1}{6} + \frac{k_2}{3} + \frac{k_3}{3} + \frac{k_4}{6}.
\end{aligned}\right\} \tag{2.29}$$

It is known that the apparent price for the higher accuracy is the use of additional computer memory for k_2, k_3 and k_4.

In order to allow a larger stability limit and reduce the computational storage without loss of accuracy, a third-step semi-implicit Runge-Kutta scheme is proposed by Le and Moin [68]. With respect to the continuity equation (Eq. (2.1)) and the incompressible Navier-Stokes equation (Eq. (2.2)), it can be written as

Step 1: $\dfrac{u_i' - u_i^n}{\Delta t} = \alpha_1 L(u_i^n) + \beta_1 L(u_i') - \gamma_1 N(u_i^n) - \zeta_1 N(u_i^{n-1}) - (\alpha_1 + \beta_1)\dfrac{\delta p'}{\delta x_i}$,   (2.30a)

$\dfrac{\delta u_i'}{\delta x_i} = 0$,   (2.30b)

Step 2: $\dfrac{u_i'' - u_i'}{\Delta t} = \alpha_2 L(u_i') + \beta_2 L(u_i'') - \gamma_2 N(u_i') - \zeta_2 N(u_i^n) - (\alpha_2 + \beta_2)\dfrac{\delta p''}{\delta x_i}$,   (2.31a)

$\dfrac{\delta u_i''}{\delta x_i} = 0$,   (2.31b)

Step 3: $\dfrac{u_i^{n+1} - u_i''}{\Delta t} = \alpha_3 L(u_i'') + \beta_3 L(u_i^{n+1}) - \gamma_3 N(u_i'') - \zeta_3 N(u_i') - (\alpha_3 + \beta_3)\dfrac{\delta p^{n+1}}{\delta x_i}$,   (2.32a)

$\dfrac{\delta u_i^{n+1}}{\delta x_i} = 0$.   (2.32b)

Here, $\delta / \delta x_i$ is the finite difference operator. $L(u_i)$ and $N(u_i)$ represent the finite difference approximations to the viscous and convective terms in the Navier-Stokes equation, respectively:

$$L(u_i) = \frac{1}{Re}\frac{\delta^2 u_i}{\delta x_j \delta x_j},$$ (2.33)

$$N(u_i) = \frac{\delta}{\delta x_j}(u_i u_j).$$ (2.34)

As shown in Table 2.2, the coefficients α, β, γ and ζ are selected so that the total time advancement between t_n and t_{n+1} has a third-order accuracy for the convective term and second-order accuracy for the viscous term.

Table 2.2 Coefficients in Runge-Kutta scheme [68]

	1	2	3
α	4/15	1/15	1/6
β	4/15	1/15	1/6
γ	8/15	5/12	3/4
ζ	0	−17/60	−5/12

In this scheme, the convective term is advanced explicitly and the viscous term is advanced implicitly. Strictly, the overall accuracy is third-order on the convective term and second-order on the viscous term. The stability limit, $CFL = u\Delta t/\Delta$, is $\sqrt{3}$ based on the total time step, which allows a larger time step. At each sub-step, the fractional step method mentioned in section 2.2 is applied. In the present simulation, the time advancement is based on this semi-implicit Runge-Kutta scheme. In order to increase the computational efficiency, only the viscous term along the wall-normal direction is advanced implicitly in the simulation.

2.6 Pressure Poisson Equation

Based on the fractional step method, the discrete pressure Poisson equation is expressed as

$$\frac{\delta^2 p^n}{\delta x_i \delta x_i} = \frac{1}{\Delta t}\frac{\delta \hat{u}_i^n}{\delta x_i}.$$

(2.35)

Here, $\delta / \delta x_i$ is the finite difference operator. Typically, direct method and iterative method are used to solve the pressure Poisson equation. The former one includes the well-known fast Fourier transform (FFT) which is prevalent in the models with periodic boundary conditions. As for a boundary layer which spatially develops in the streamwise direction, iterative methods, including the Conjugate Gradient method (CG), Bi-Conjugate Gradient method (Bi-CG) and Stable Bi-Conjugate Gradient method (Bi-CGStab), are more efficient. Here, the Bi-CGStab method is proposed by Van der Vorst [69] for solving the nonsymmetric linear systems. It is concluded that the Bi-CGStab method has a fast and smooth convergence behavior and is attractive for incompressible flows. Thus, in the present simulation, Bi-CGStab method is adopted for solving the pressure Poisson equation.

In term of linear system, pressure Poisson equation (Eq. (2.35)) can be rewritten as

$$Ax = b,$$

(2.36)

where $A = \delta^2 / \delta x_i \delta x_i$ (a large sparse matrix), $x = p^n$, and $b = \frac{1}{\Delta t}\frac{\delta \hat{u}_i^n}{\delta x_i}$. By using the Bi-CGStab method [69], Eq. (2.36) can be solved according to the following steps.

1. Set an initial value of x_0, e.g., $x_0 = 0$;

2. Compute the initial residual $r_0 = b - Ax_0$;

3. Set an arbitrary vector $\hat{r}_0$ which satisfies $(\hat{r}_0, r_0) \neq 0$, e.g., $\hat{r}_0 = r_0$;

4. Set $\rho_0 = \alpha = \omega_0 = 1$; $\upsilon_0 = p_0 = 0$;

5. Do $i = 1, 2, 3, ...$,

$\rho_i = (\hat{r}_0, r_{i-1})$;

$\beta = (\rho_i / \rho_{i-1})(\alpha / \omega_{i-1})$;

$p_i = r_{i-1} + \beta(p_{i-1} - \omega_{i-1}\upsilon_{i-1})$;

$\upsilon_i = Ap_i$;

$\alpha = \rho_i / (\hat{r}_0, \upsilon_i)$;

$s = r_{i-1} - \alpha\upsilon_i$;

$t = As$;

$\omega_i = (t,s)/(t,t)$;

$x_i = x_{i-1} + \alpha p_i + \omega_i s$;

If x_i is accurate enough then quit;

$r_i = s - \omega_i t$;

End.

2.7 Boundary and Initial Conditions

2.7.1 Boundary conditions

It is well recognized that besides the numerical algorithm, properly chosen boundary conditions are of great importance in view of a good representation of a physical system. In this thesis, a spatially developed boundary layer is investigated. For illustrating the boundary conditions in this case, a two-dimensional computational domain is shown in Fig. 2.6. The fluid flows from the left side to the right side and the boundary layer is developed on the bottom wall.
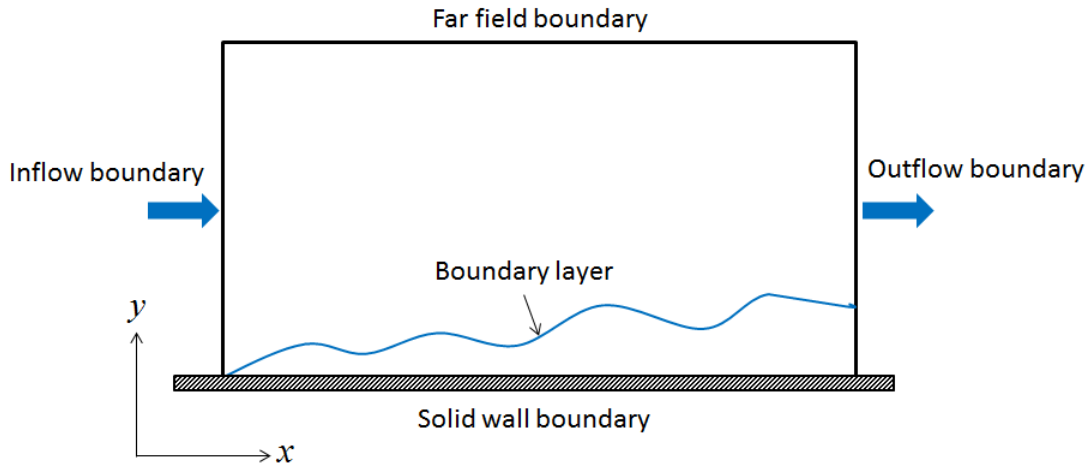
Fig. 2.6 Computational domain

(1) Solid wall boundary

With respect to a solid wall without permeability, the fluid sticks to the surface due to the viscous effects, and there is no slip. If the solid wall is stationary, the non-slip boundary condition, $u_i = 0$, can be applied. Note that the normal velocity component could be set to zero straightaway while the tangential component is set to the velocity of the wall when the solid wall is motional.

(2) Far field boundary

At a far field boundary where there is no friction between the fluid and the boundary, the slip boundary condition can be applied. For providing such boundary condition, the velocity component normal to slip boundary should be zero and the gradient of velocity parallel to slip boundary should be zero.

(3) Inflow boundary

As for a spatially developed boundary layer where the flow is inhomogeneous in the streamwise direction, an inflow boundary condition as well as the outflow boundary condition should be designated, respectively. Owing to the chaotic character of the Navier-Stokes equations, any uncertainty in the inflow boundary condition can remain as a source of error during the simulation and strongly affect the afterward flow field development [70]. Basically, the existing inflow generation techniques for a turbulent boundary layer can be classified as the random fluctuations method [71-73] and the auxiliary

simulation method [74]. The main idea of random fluctuations method is to superimpose some fluctuations to the typical mean profiles, while the main idea of auxiliary simulation method is to rescale the velocity fields extracted from an auxiliary simulation and re-introduce them at the inlet. In the present study, the developing region of a boundary layer affected by various disturbances is of major interest. Therefore, the additional disturbance is inappropriate and the inflow boundary condition can be simplified by using the uniform flow with a 1/7 power law near the bottom wall.

(4) Outflow boundary

Conjuncting to the inflow boundary condition, appropriate outflow boundary condition has to be designated in this study to ensure that the flow can approach and pass the outlet without significant disturbance on reflection back into the computational domain. This leads to the so-called nonreflecting boundary conditions, among which convective outflow boundary condition, expressed as follows, is prevalent.

$$\frac{\partial u_i}{\partial t} + U_c \frac{\partial u_i}{\partial x} = 0 .$$
(2.37)

Here, U_c is the convective velocity which is taken as the mean streamwise velocity averaged at the outlet. This outflow boundary condition works well in convecting large disturbances out of the computational domain with minimum reflections and has been used successfully in internal as well as external flows.

Note that if the flow is statistically homogeneous in one or more directions, the inflow and outflow boundary conditions mentioned above can be simplified by using a periodic boundary condition in these directions. Given an arbitrary variable, ϕ, the periodic boundary condition is expressed as

$$\phi_0 = \phi_N , \quad \phi_1 = \phi_{N+1} , \; \dots \; .$$
(2.38)

However, care must be taken to ensure that the computational domain is sufficiently large to contain a representative number of large-scale structures or more specifically, at least twice as large as the separation at which two-point correlations vanish [63].

2.7.2 Initial condition

Apart from the boundary condition, initial condition is also needed to be designated in

numerically solving the time-evolving flows. Considering the computational efficiency, an ideal situation is that the simulation is started with the initial condition which is close to the realistic final state. In most cases, such initial condition is not known. It has to be generated in some way. The methods of generating inflow boundary condition can also be applied in generating the initial condition. As for the turbulent flow, it gets independent of the initial condition if sufficient time has elapsed [63]. Thus, the simplest way to superimpose the fluctuations generated by random noise to the typical mean profiles is sufficient. However, it may happen that the fluctuations decay since there is a lack of energy in the low wave number, causing unphysically high viscous dissipation. This can be overcome by artificially increasing the Reynolds number and then gradually decreasing it to the desired value [63]. There is then sufficient transient time in which fluctuating energy can be distributed among all the wave numbers.

Table 2.3 Numerical schemes used in current research

Governing equations	Continuity equation Incompressible Navier-Stokes equations Scalar transfer equation	
Numerical algorithm	Fractional step method	
Time advancement	3rd-order Runge-Kutta [68]	Convective term
		Viscous and Diffusion terms (x, z directions)
	2nd-order Crank-Nicolson	Viscous and Diffusion terms (y direction)
Spatial discretization	Fully conservative 2nd-order CDS [66]	Convective term
	2nd-order CDS	Viscous and Diffusion terms (x, y directions)
	4th-order CDS	Viscous and Diffusion terms (z direction)
Poisson equation	Bi-CGstab [69]	
Mesh arrangement	Staggered mesh	

2.8 Summary

In this chapter, the details of direct numerical simulation (DNS) are presented. A summary of the numerical schemes used in current research are shown in Table 2.3. Note that CDS stands for central difference scheme.

Chapter 3

Boundary Layer with Heat Transfer under the Effects of a Tripping Object Mounted on the Wall (75)

3.1 Introduction

The role of the tripping object in boundary layers is one of the significant topics, especially with regard to the flow control in the engineering applications. In this chapter, the effects of a tripping object on the development of a boundary layer with heat transfer are investigated by a three-dimensional direct numerical simulation (DNS).

3.2 Numerical Details

Figure 3.1 shows the schematic of the computational domain. It is a rectangular parallelepiped box with a size of $L_x \times L_y \times L_z = 6H \times H \times H$. Here, H is the height of the computational domain, and x, y, and z denote the streamwise, wall-normal, and spanwise coordinate axes, respectively. The origin of the coordinate is at the center and bottom end of the tripping object. As a tripping object, nine small cubes with a side length of $0.02H$ are placed on the bottom wall alternatively in the spanwise direction. More specifically, as shown in Fig. 3.1, four of them are placed at $x = 0.36H$ while the other five are placed at $x = 0.44H$. The spanwise spacing between the cubes is set to $k = 0.1H$.

The Cartesian mesh system with mesh numbers of $624 \times 200 \times 160$ in the streamwise, wall-normal, and spanwise directions is used. Non-uniform meshes are employed in the streamwise and wall-normal directions, while the uniform mesh is employed in the spanwise direction. Figures 3.2(a) and (b) show the streamwise and wall-normal spatial resolutions, respectively. The value of Δx at $x = 0$ is about $1/8$ of that in the far

downstream, which enables an accurate calculation near the tripping object with high efficiency. In addition, due to the steep gradient of the velocity and temperature near in the boundary layer, the mesh points are clustered near the wall ($y \leq 0.25H$) by using a hyperbolic tangent function as shown below:

$$y_j = \frac{H}{4}\left\{1 - \frac{\tanh[\alpha(1 - j/N_{yw})]}{\tanh\alpha}\right\},$$
(3.1)

where N_{yw} is the mesh numbers in the near-wall region of $y \leq 0.25H$, $\alpha = 1.914$, and $j = 1,2,3,...$. Note that it is required to place at least three mesh points within the viscous sublayer to catch the smallest structure in a boundary layer [76]. In this simulation, thirteen mesh points are set within the viscous sublayer to meet such requirement. Moreover, the spatial resolutions normalized by the wall units are $\Delta x^+ = 0.76 \sim 6.67$, $\Delta y^+ = 0.28 \sim 3.33$, and $\Delta z^+ = 3.33$. This is in agreement with pervious simulations [77-78], ensuring the accuracy of the spatial resolutions.
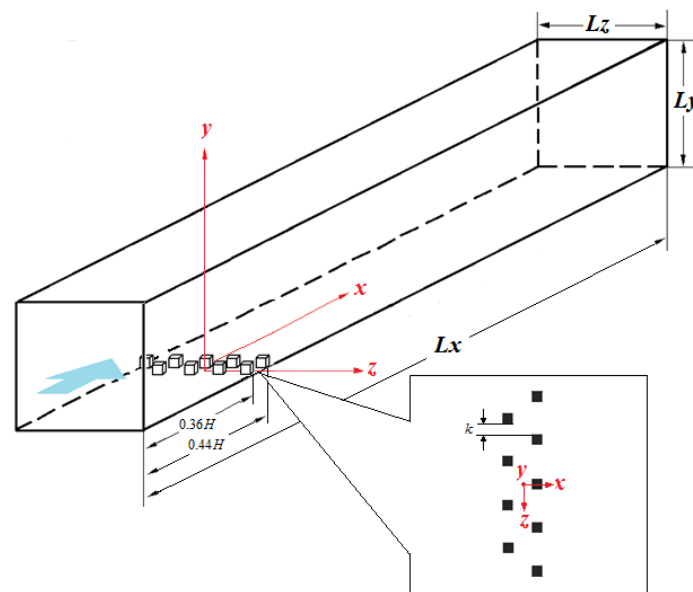
Fig. 3.1 Schematic of the computational domain
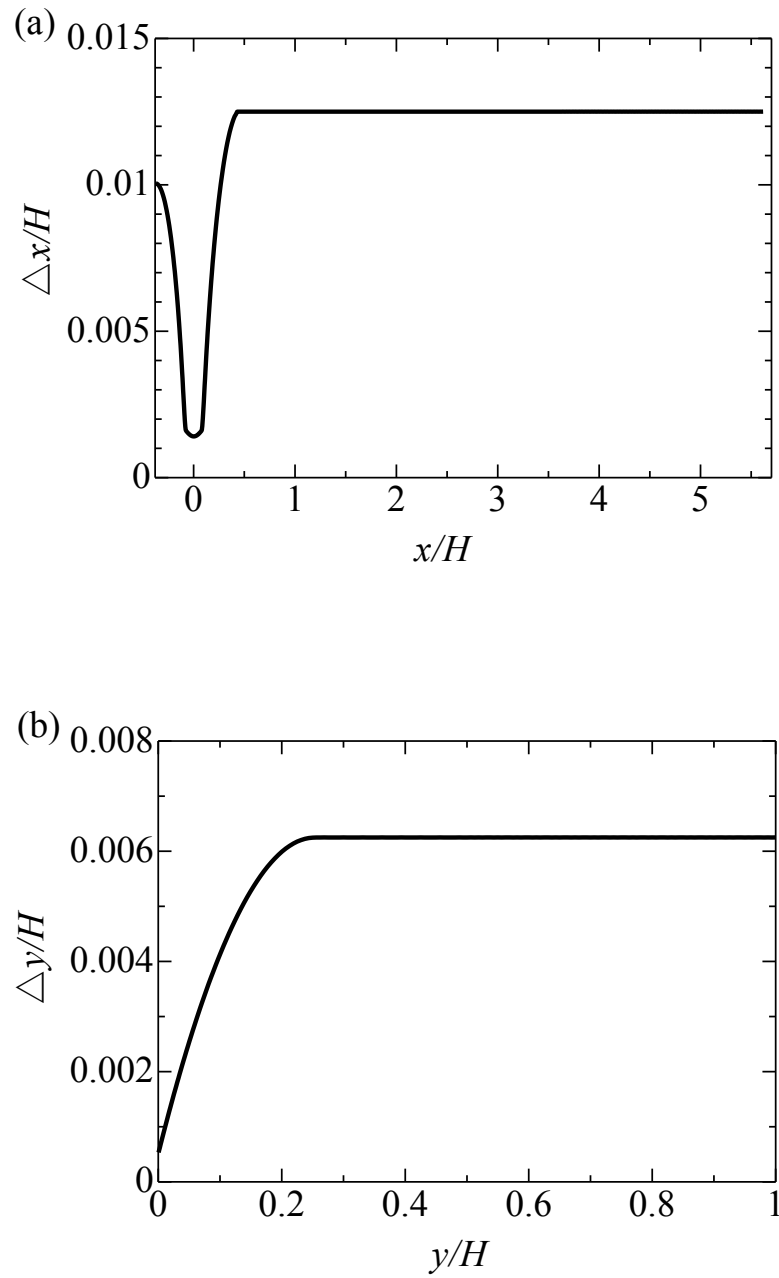
Fig. 3.2 Spatial resolutions

In this simulation, the governing equations are the normalized continuity equation (Eq. (2.1)), incompressible Navier-Stokes equations (Eq. (2.2)), and the scalar transfer equation (Eq. (2.3)). Here, Reynolds number, $Re = U_\infty H / \nu$, is set to 13333 and Prandtl number, Pr, is set to 0.71. The normalized computational time step is set to $\Delta t U_\infty / H = 0.0005$, which corresponds to a maximum Courant-Friedrichs-Lewy (CFL) condition of $CFL_{max} = 0.94$. The numerical schemes summarized in the former chapter (Table 2.3) are adopted for solving these governing equations.

A uniform flow without any disturbance is given as the inflow boundary condition but a $1/7$ power law is employed near the bottom wall ($y \le 0.125H$). The temperature inflow boundary condition is similar to the flow field at the inlet. The convective outflow boundary conditions (Eq. (2.37)) for velocity and temperature are applied at the exit. Here, the convective velocity is obtained by averaging the streamwise velocity over the spanwise direction at the exit. The non-slip ($u = v = w = 0$) and constant temperature ($T = 0$) boundary conditions are imposed on the wall, while the slip ($\partial u / \partial y = \partial w / \partial y = 0$, $v = 0$) and constant temperature ($T = 1$) boundary conditions are applied to the upper boundary. The periodic boundary condition is applied in the spanwise direction. On the surface of the tripping object, the interpolation method is applied to make the velocity zero. For the pressure, the Neumann boundary condition ($\partial p / \partial x_i = 0$) is employed.

3.3 Results and Discussion

3.3.1 Instantaneous flow and thermal fields

Figures 3.3 and 3.4 show the instantaneous velocity and temperature fields on the $x - y$ plane at $z = 0$, respectively. It is confirmed that the velocity and thermal boundary layers are developed spatially. The uneven boundary layers in the flow and thermal fields are mostly visible in the vicinity of the tripping object and such characteristic becomes less discernible in the downstream region. It is also seen that the amplitudes of the wall-normal and spanwise velocities are smaller, especially in the downstream region.
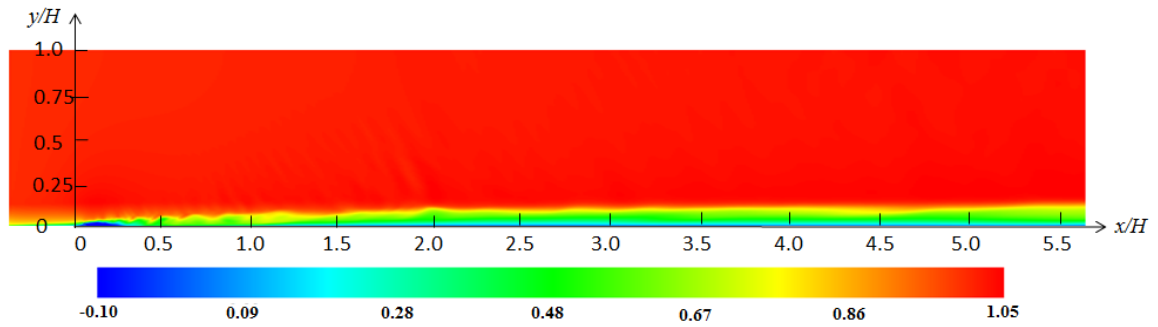
(a) Streamwise velocity
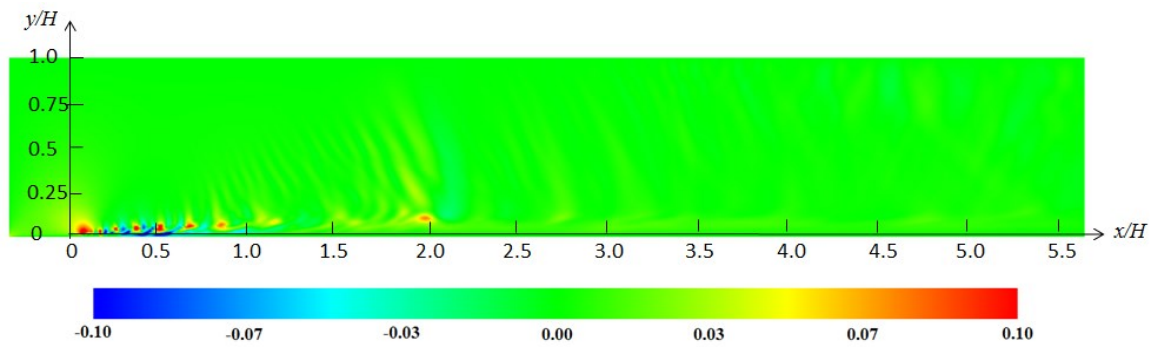
(b) Wall-normal velocity
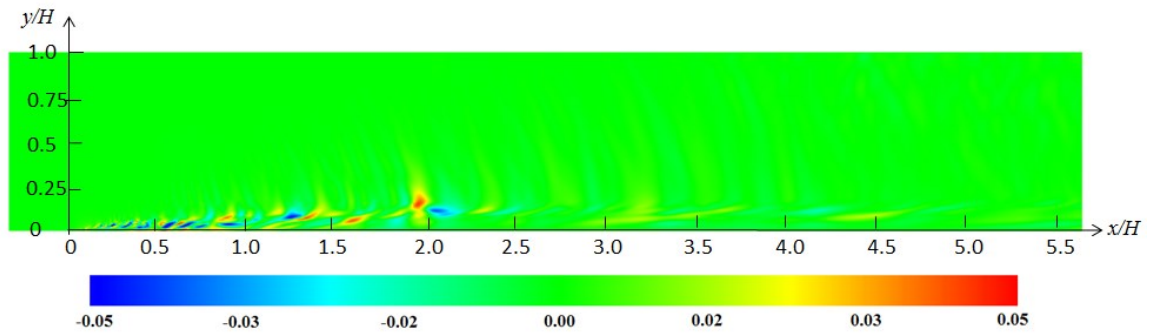
(c) Spanwise velocity

Fig. 3.3 Instantaneous velocity fields
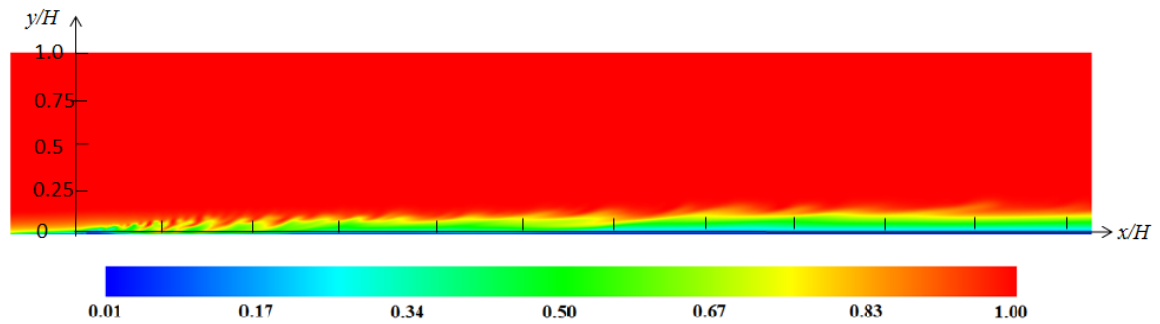
Fig. 3.4 Instantaneous temperature field

Instantaneous streamline in the vicinity of the tripping object and in the downstream region is shown in Figs. 3.5(a) and (b), respectively. It is observed from Fig. 3.5(a) that recirculation region exists behind the tripping object and the streamlines exhibit wavy motions. On the other hand, as shown in Fig. 3.5(b), the streamline in the downstream region appears to remain smooth since the disturbances generated by the tripping object become small in the downstream region as shown in Fig. 3.3.
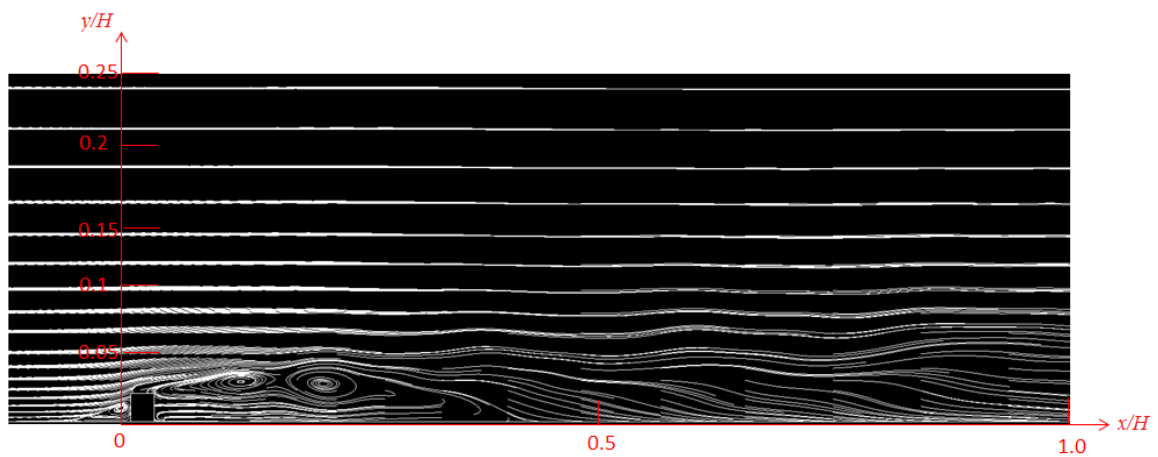
(a) In the vicinity of the tripping object
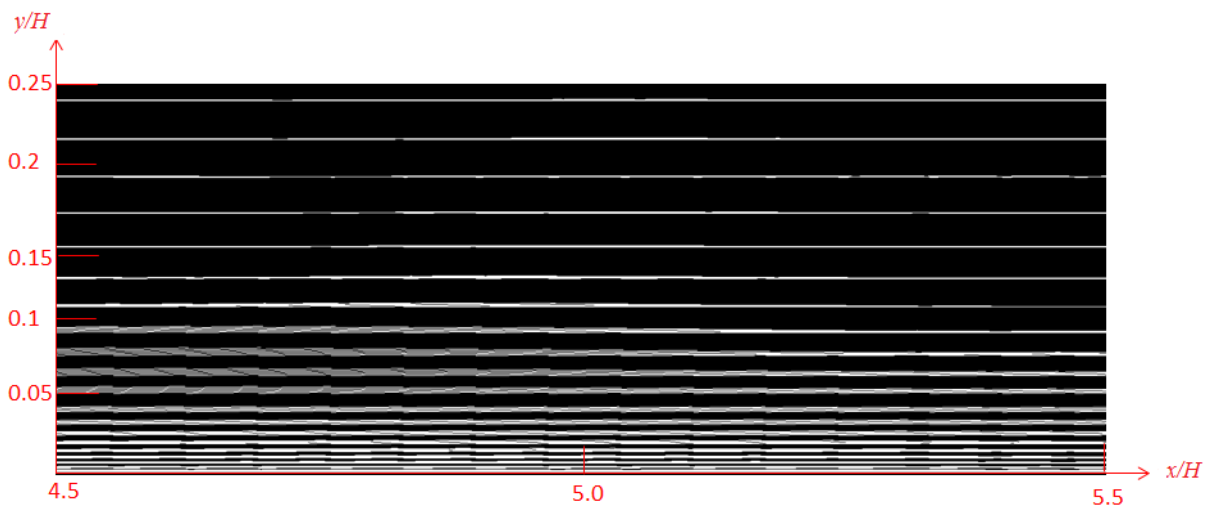
(b) In the downstream region

Fig. 3.5 Instantaneous streamline fields

The evolution of the boundary layer in this case is also examined by visualizing the normalized instantaneous spanwise vorticity, $\omega_z H / U_\infty$, on the $x - y$ plane at $z = 0$ as shown in Fig. 3.6. The negative vortices, which are similar to the Karman vortices shed from the upper side of the tripping object (small cubes), are developed in the vicinity of the tripping object. In the downstream region, however, such characteristic can hardly be seen.
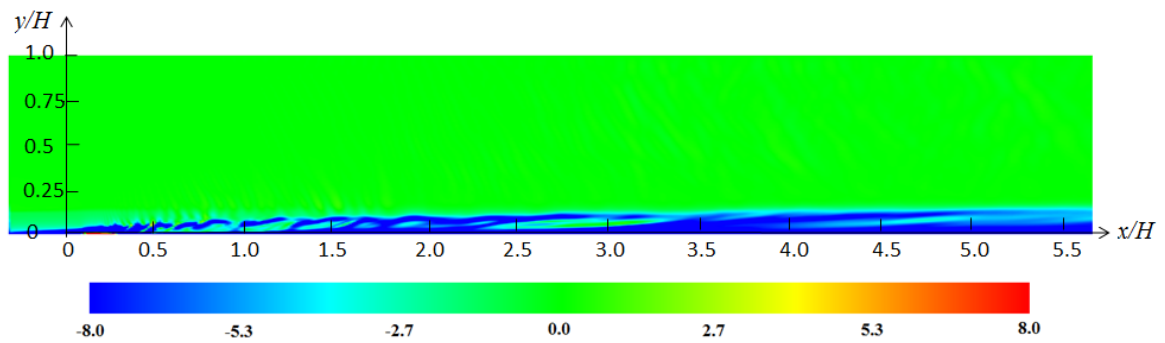
Fig. 3.6 Instantaneous spanwise vorticity field
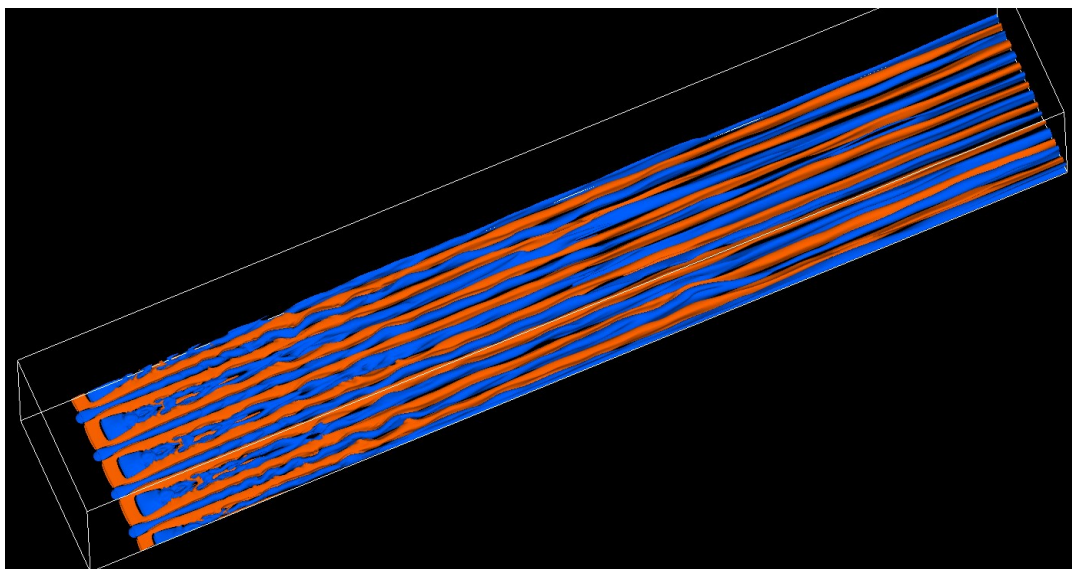
Fig. 3.7 Iso-surfaces of streamwise velocity fluctuations
(blue: $u'/U_\infty = -0.1$; orange: $u'/U_\infty = 0.1$)

Figure 3.7 shows the visualized iso-surfaces of streamwise velocity fluctuations at the same time step as before. The streamwise elongated streaky structures with high and low streamwise velocity fluctuations alternating in spanwise direction are clearly observed in the whole region. Note that such low- and high-speed streaks undergo wave motions with tips tilted towards the downstream direction in the upstream region, while they appear to be stable in the downstream region. This is attributed to the different vortical structures in these two regions which will be discussed later in section 3.3.6.

Above all, it has shown that the tripping object used in this case mainly affects the upstream region in the flow and thermal fields. In the downstream region, such tripping effect becomes weak.

3.3.2 Integral quantities

In the following, we define the time-averaging quantities as

$$F = \bar{f} = \frac{1}{L_z}\frac{1}{t_a}\int_0^{L_z}\int_{t-t_a}^{t} f(x,y,z,t)dtdz \ . \tag{3.2}$$

Here, the time-averaging period, t_a, is set to the time length that the flow goes through the entire computational domain twice. In other words, all the statistical values in this simulation are taken after the flow goes through the computational domain for two cycles and then averaged over the following two flow-through cycles.

It is known that a direct and overall assessment of the boundary layer development can be obtained by the boundary layer thickness, δ, as well as the displacement thickness, δ^*, and the momentum thickness, θ. Here, δ is defined as the distance across a boundary layer from the wall to a point where the flow velocity has essentially reached 99% of the free-stream velocity, and δ^* and θ are defined as

$$\delta^* = \int_0^{\delta}\left(1 - \frac{U}{U_\infty}\right)dy \ , \tag{3.3}$$

$$\theta = \int_0^{\delta}\frac{U}{U_\infty}\left(1 - \frac{U}{U_\infty}\right)dy \ . \tag{3.4}$$

Figure 3.8 shows the streamwise evolution of boundary layer thickness. The increase of boundary layer thickness along the streamwise direction is clearly observed.
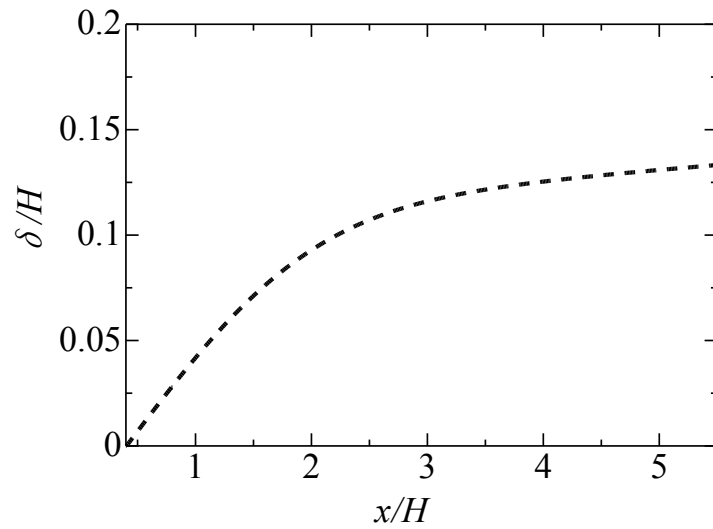
Fig. 3.8 Streamwise evolution of boundary layer thickness
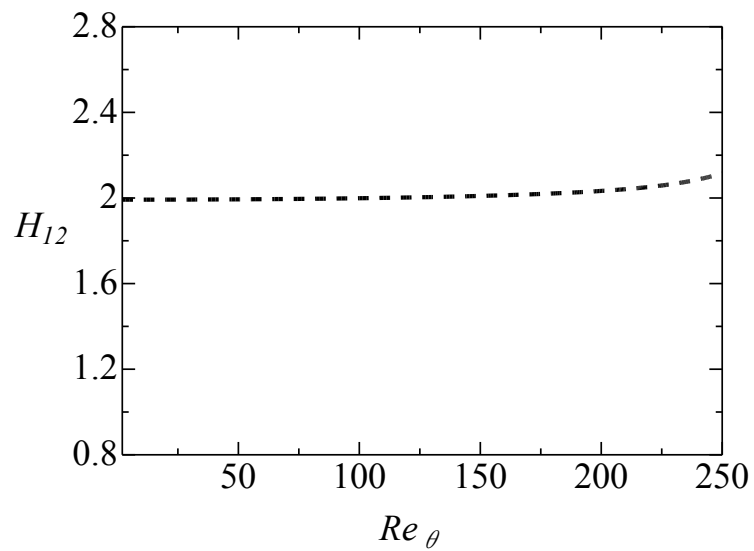
Fig. 3.9 Distribution of shape factor

In particular, the ratio of the two integral quantities, the shape factor, $H_{12} = \delta^{*}/\theta$, is considered to be a good indicator of the boundary layer state. Based on the Blasius solution, the value of H_{12} is about 2.6 in a laminar boundary layer. In a turbulent boundary layer, on the other hand, it is around 1.5 obtained by previous studies [79-81]. The distribution of H_{12} against Re_{θ} is plotted in Fig. 3.9. H_{12} is smaller than the typical value in a laminar boundary layer and does not approach the typical value in a turbulent boundary layer. This evidences the fact that the boundary layer flow is to some extent transitional.

3.3.3 Mean profiles

The wall-normal distributions of mean streamwise velocity and mean temperature at different streamwise locations are shown in Figs. 3.10 and 3.11, respectively. The arrow points in the downstream direction. The results of a transitional boundary layer at $Re_{\theta} = 250$ obtained by Nolan et al. [82] and Wu and Durbin [83] are also included to validate the present DNS. It is observed, in the viscous sublayer ($y^{+} < 5$), that the mean streamwise velocity and temperature profiles both follow the linear distributions as seen in a typical turbulent boundary layer:

$$U^{+} = y^{+}, \tag{3.5}$$

$$\bar{T}^{+} = \Pr y^{+}. \tag{3.6}$$

Here, $U^{+} = U/u_{\tau}$, $\bar{T}^{+} = \bar{T}/T_{\tau}$ (T_{τ} is the friction temperature), $y^{+} = yu_{\tau}/v$. In the log-law layer ($30 < y^{+} < 100$), however, they deviate from the typical log-law distribution in a turbulent boundary layer expressed by the following equations:

$$U^{+} = \frac{1}{0.41}\ln(y^{+}) + 5.0, \tag{3.7}$$

$$\bar{T}^{+} = 2.075\ln(y^{+}) + 4.03. \tag{3.8}$$

Again, this indicates that the boundary layer flow is still in transition. Moreover, as moving to the downstream region, the deviation from the log-law distribution becomes larger. This phenomenon confirms the former observation in the instantaneous fields that the uneven boundary layers become less discernible in the downstream region. It is suggested that the effect of the tripping object becomes weak in the downstream region.
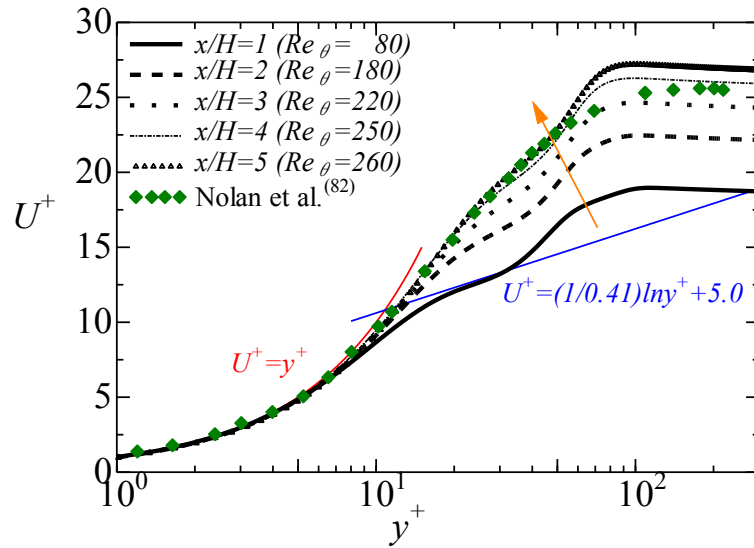
Fig. 3.10 Mean streamwise velocity profile
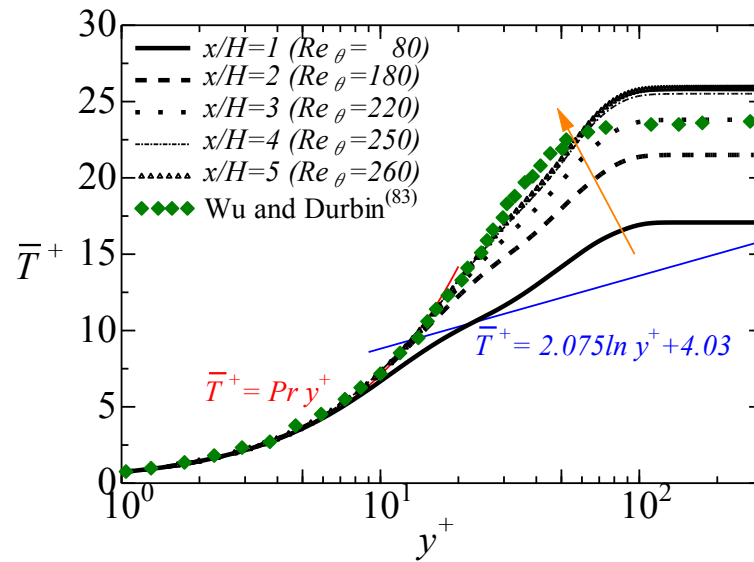
Fig. 3.11 Mean temperature profile

(a)

(b)

(c)
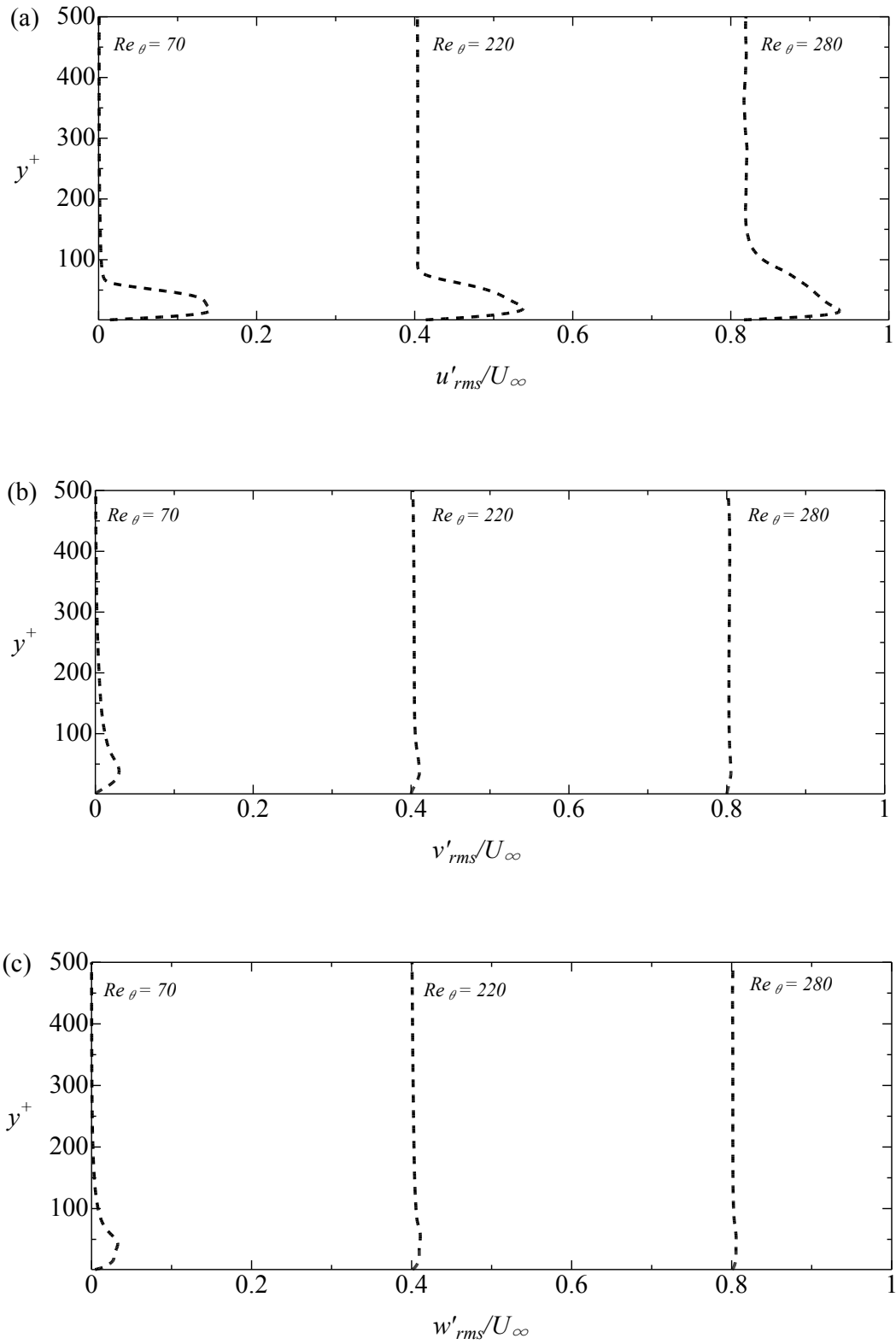
Fig. 3.12 Streamwise evolution of rms velocity fluctuations

3.3.4 Fluctuation profiles

Figure 3.12 shows the evolution of the root-mean-square (rms) values of the velocity fluctuations in the streamwise direction which corresponds to the direction of the increase of Re_θ. It is observed that the values of v'_{rms} and w'_{rms} are much smaller than that of u'_{rms} at each streamwise location. Besides, they become smaller in the downstream region. Again, it suggests that the effect of the tripping object becomes weak in the downstream region and the boundary layer has a laminar-like structure.

The correlation coefficients for u' and v', and v' and T',

$$R_{uv} = \frac{-\langle u'v' \rangle}{u'_{rms}\, v'_{rms}}, \tag{3.9}$$

$$R_{vT} = \frac{-\langle v'T' \rangle}{v'_{rms}\, T'_{rms}}, \tag{3.10}$$

at the streamwise location of $x/H = 4$ ($Re_\theta = 250$) are plotted in Fig. 3.13. The results of a pure turbulent boundary layer (TBL) in the experiments by Chen and Blackwelder [84] are also included for comparison. As for a pure TBL, R_{uv} and R_{vT} increase near the wall and then level off at 0.5 within the range of $0.2 < y/\delta < 0.7$. In the case with the tripping object, R_{uv} and R_{vT} follow the same trend as seen in the experiments by Chen and Blackwelder [84] but the constant values are larger since the flow is still in transition.
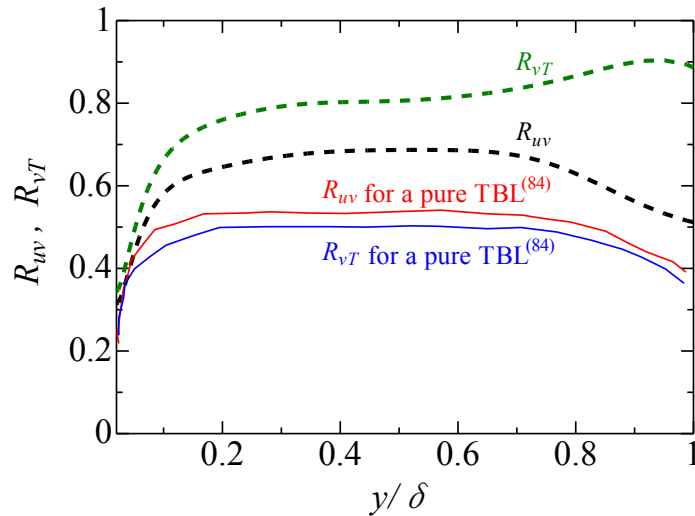
Fig. 3.13 Distribution of the correlation coefficients at $x/H = 4$ ($Re_\theta = 250$)

3.3.5 Wall quantities

The skin friction coefficient, C_f, and the Stanton number, St, are two important wall quantities in a boundary layer. They are defined as

$$C_f = \frac{\tau_w}{\frac{\rho U_\infty^2}{2}},$$

(3.11)

$$St = \frac{h}{\rho C_p U_\infty},$$

(3.12)

where τ_w is the wall shear stress defined by

$$\tau_w = \mu \left. \frac{\partial U}{\partial y} \right|_{y=0},$$

(3.13)

C_p is the specific heat at a constant pressure, and h is the heat transfer coefficient defined by

$$h = \frac{-\kappa (\partial T / \partial y)|_{y=0}}{T_w - T_\infty}.$$

(3.14)

Here, μ is the dynamic viscosity of the fluid and κ is the thermal conductivity of the fluid. Figures 3.14 and 3.15 show the streamwise development of C_f and St, respectively. In the case with the tripping object, C_f is almost the same as that for a laminar boundary layer (LBL). It indicates that the effect of the tripping object on the skin friction in a boundary layer is very small. A similar profile is seen in St (Fig. 3.15) which is the counterpart of C_f and provides a measurement of heat transfer on the wall. Note that the typical value of St for a laminar boundary layer (LBL) is derived from the Reynolds-Colburn analogy expressed as follows [85]:

$$St = \frac{C_f}{2} Pr^{-2/3}.$$

(3.15)

In the case with the tripping object, St is larger than the typical value for a LBL in the upstream region, but it approaches the same value in the downstream region since the effect of the tripping object disappears. It means that heat transfer is slightly enhanced by the tripping object.
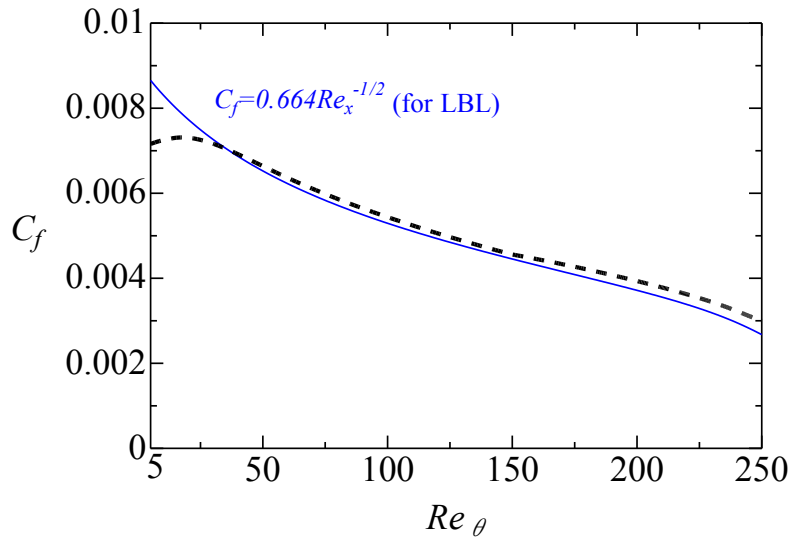
Fig. 3.14 Streamwise distribution of skin friction coefficient
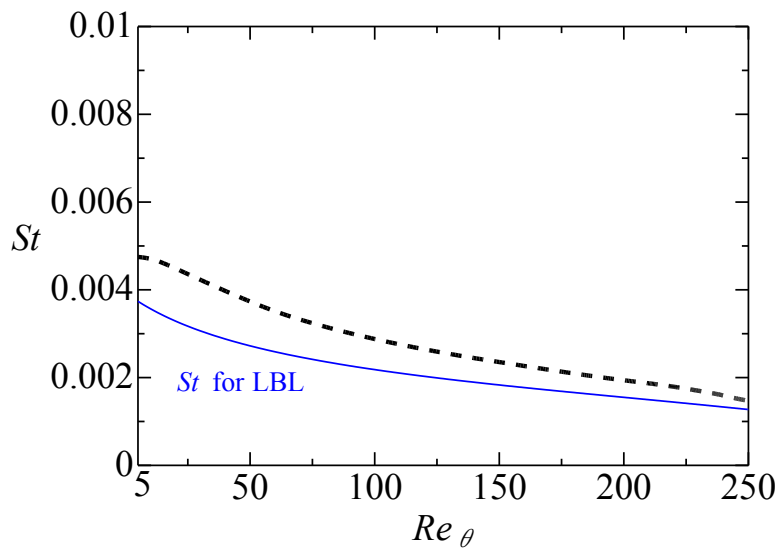
Fig. 3.15 Streamwise distribution of Stanton number

The relationship between the momentum and heat transfer can be expressed by the analogy factor, $St/(C_f/2)$. It is known that, when the analogy factor is constant, momentum transfer is analogous to heat transfer, i.e. the Reynolds analogy holds. Figure 3.16 shows the streamwise distribution of the analogy factor in this case. It lies around 1 in the downstream region, indicating that the Reynolds analogy holds. However, in the vicinity of the origin where the tripping object is placed, the analogy factor increases, implying that the Reynolds analogy does not hold in this region. This is mainly due to the fluctuations generated by the tripping object near the origin.
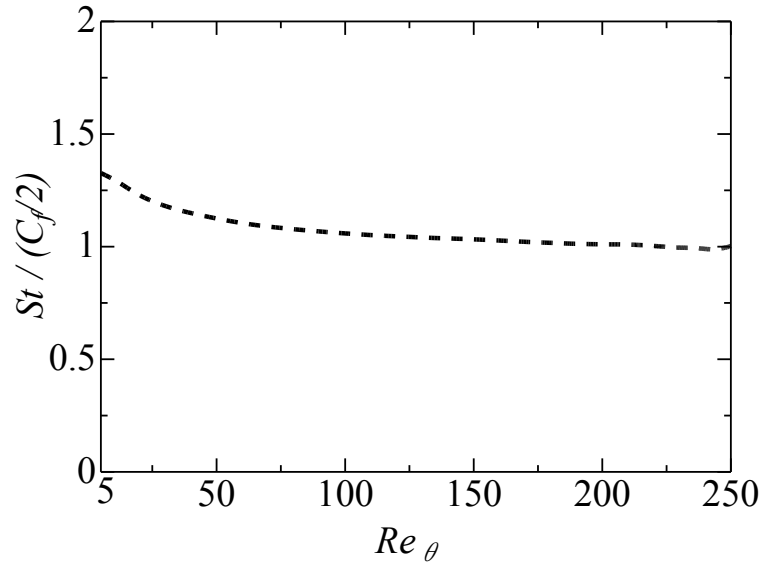
Fig. 3.16 The analogy factor

3.3.6 Vortical structures

The vortical structures play a major role in the dynamics of transition from laminar to turbulent boundary layer. It has been known that the second invariant of velocity gradient tensor, Q, is mostly used to visualize such voritical structures. Here, Q is defined by

$$Q = \frac{1}{2}\left(W_{ij}W_{ij} - S_{ij}S_{ij} \right), \tag{3.16}$$

where W_{ij} is the skew-symmetric rate of rotation tensor, and S_{ij} is the symmetric rate of strain tensor, which are expressed as:

$$W_{ij} = \frac{1}{2}\left(\frac{\partial u_j}{\partial x_i} - \frac{\partial u_i}{\partial x_j} \right), \quad S_{ij} = \frac{1}{2}\left(\frac{\partial u_j}{\partial x_i} + \frac{\partial u_i}{\partial x_j} \right), \tag{3.17}$$

where u_i is the instantaneous velocity. Figure 3.17 shows the visualized iso-surface of $QH/U_\infty = 0.3$ (white) along with the iso-surfaces of $u'/U_\infty = -0.1$ (blue) and $u'/U_\infty = 0.1$ (orange). It has seen that the vortical structures in the upstream region are more concentrated than those in the downstream region. In the downstream region, the longitudinal structures, located between the high- and low-speed streaks, are prevalent. A close-up of the vortical structures in the upstream region is displayed in Fig. 3.18, showing the presence of the hairpin-like structure in the upstream region. Such vortical structure is in a form where tips are lifted up and tilted towards the downstream direction. Typically, they are the product of the tripping object (small cubes) mounted at the leading edge of the boundary layer. It is also observed that such hairpin-like structure straddles the low-speed streaks (blue) and the high-speed streaks (orange) are located aside, causing the wave motions in the high- and low-speed streaks observed in Fig. 3.7 previously.

3.4 Summary

A DNS of the boundary layer with heat transfer subjected to the internal disturbance generated by a tripping object mounted on the wall has been performed to investigate the effects of such disturbances on the flow field and heat transfer in the boundary layer. The results are summarized as follows:

(1) The boundary layer has been triggered by the tripping object and the flow in this boundary layer is to some extent transitional.

(2) The effect of the tripping object on the development of the boundary layer is weak, especially in the downstream region. Only small-amplitude fluctuations are generated in the vicinity of the tripping object and the flow in the downstream region has a laminar-like structure.

(3) Heat transfer is slightly enhanced by the tripping object, and there is almost no effect on the skin friction.

(4) In the upstream region, the hairpin-like structure, induced by the tripping object (small cubes), is visible. In the downstream region, the longitudinal structures are prevalent.
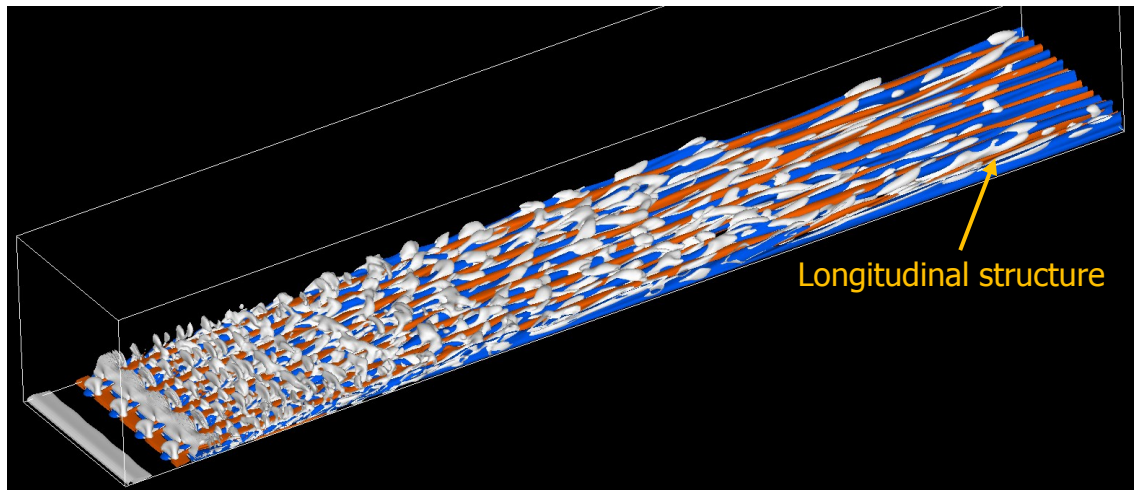
Fig. 3.17 Iso-surface of $QH/U_\infty = 0.3$ (white) along with the iso-surfaces of streamwise velocity fluctuations (blue: $u'/U_\infty = -0.1$; orange: $u'/U_\infty = 0.1$)
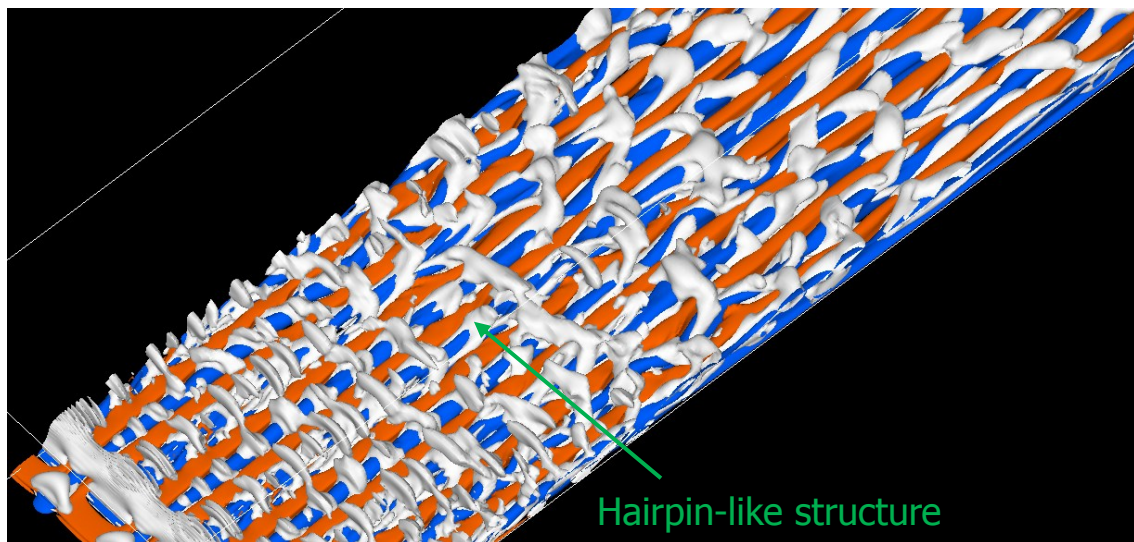
Fig. 3.18 A close-up of iso-surface of $QH/U_\infty = 0.3$ (white) in the upstream region (blue: iso-surface of $u'/U_\infty = -0.1$; orange: iso-surface of $u'/U_\infty = 0.1$)

Chapter 4

Boundary Layer with Heat Transfer under the Effects of Grid Turbulence [75][86-87]

4.1 Introduction

In addition to using the internal disturbance discussed in Chapter 3, people have been trying to control the boundary layer by using the external disturbance. In this chapter, the effects of an external disturbance generated by a regular grid on the development of a boundary layer with heat transfer are investigated by a three-dimensional direct numerical simulation (DNS).

4.2 Numerical Details

Figure 4.1 shows the schematic of the computational domain. A biplane regular grid, which is installed at a location of $0.4H$ downstream from the inlet, is chosen to generate the external grid turbulence. The mesh size and thickness of the grid are $M = 0.25H$ and $D = 0.05H$, respectively, corresponding blockage ratio being 0.36. Note that the influence of the grid bars mounted on the bottom wall on the transition of the boundary layer is assumed to be negligible [40] in this case. The origin of the coordinate is set at the center and bottom end of the grid. Table 4.1 shows the size of the computational domain and mesh numbers. The non-uniform mesh spacing, which is similar to that shown in Fig. 3.2, is employed in the streamwise and wall-normal directions, respectively. Accordingly, the spatial resolutions normalized by the wall units are $\Delta x^+ = 1.05 \sim 9.33$, $\Delta y^+ = 0.39 \sim 4.67$, and $\Delta z^+ = 4.67$, which are in agreement with pervious simulations [77-78], ensuring the accuracy of the spatial resolutions. Moreover, in order to meet the requirement for catching the smallest structure in a boundary layer [76], ten mesh points in the wall-normal direction are set within the viscous sublayer in this case.

With respect to the numerical schemes and boundary conditions, they are the same as those in the former case, i.e. the case with the tripping object. Note that DNS is carried out at $Re = U_\infty H/\nu = 13333$ (corresponding to $Re_M = U_\infty M/\nu = 3333$) and $Pr = 0.71$ in the case with the grid turbulence.
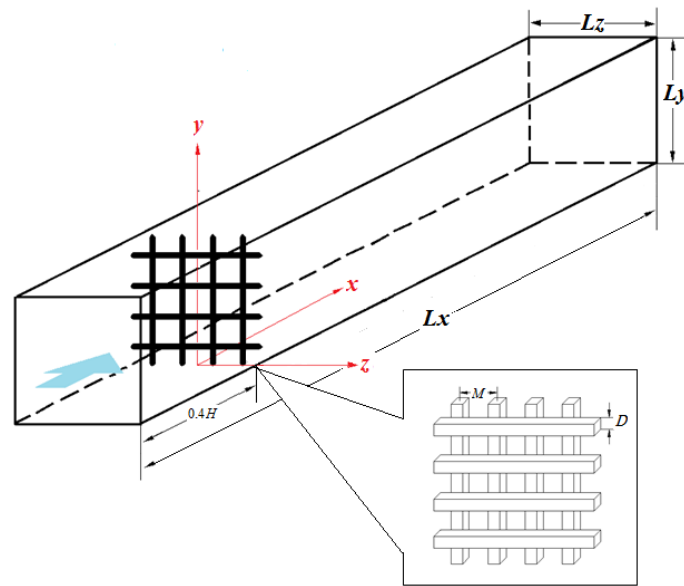
Fig. 4.1 Schematic of the computational domain

Table 4.1 Computational domain size and mesh numbers

Domain size $L_x \times L_y \times L_z$	$6H \times H \times H$
Mesh number $N_x \times N_y \times N_z$	$624 \times 200 \times 160$

4.3 Results and Discussion

4.3.1 Characteristics of the grid turbulence

The turbulence intensity of the grid turbulence is defined as

$$Tu = \frac{\sqrt{\left(u'^{2}_{rms} + v'^{2}_{rms} + w'^{2}_{rms}\right)/3}}{U_{\infty}} ,$$

(4.1)

where u'_{rms}, v'_{rms}, and w'_{rms} are the root-mean-square (rms) values of the velocity fluctuations. Figure 4.2(a) shows the streamwise evolution of the turbulence intensity at different wall-normal locations above the boundary layer. It is confirmed that the grid turbulence is homogeneous in the region of $x/H > 1$. Besides, Tu at the beginning is nearly 50% of the free-stream velocity and then decays to 7% at around $x/H = 4$ in the downstream region. Note that the turbulence intensity decays with a power law, $Tu = Cx^{-0.7}$, where C is determined by the grid configuration and the mesh Reynolds number, $Re_{M} = U_{\infty}M/\nu$. In this case, $C = 0.2$. In addition, the exponent, -0.7, gives the decay rate, which is a little bit smaller than that in the previous studies (-0.5 given by Tennekes and Lumley [88] and -0.6 obtained by Oberlack [89]). On the other hand, the rms values of the velocity fluctuations are displayed in Fig. 4.2(b). It is confirmed that the grid turbulence is nearly isotropic.

The integral length scale is defined as

$$L_{\infty} = \int_{0}^{\infty} \frac{\overline{u'(x,t)u'(x+r,t)}}{(u')^{2}} dr ,$$

(4.2)

where the overbar denotes the time average as defined in Eq. (3.2). Figure 4.3 shows the streamwise evolution of the integral length scale at the wall-normal location of $y/H = 0.7$. It is clear that the integral length scale increases with the streamwise distance. In the downstream region of $x/H = 4$, the integral length scale of the grid turbulence is around $L_{\infty}/\delta \approx 0.7$.

The streamwise profiles of the normalized mean pressure drop, P, caused by this turbulence-generating grid is plotted in Fig. 4.4. Here, P is averaged in the $y-z$ plane. As expected, P peaks immediately downstream of the grid, generating a large pressure drop.

(a)
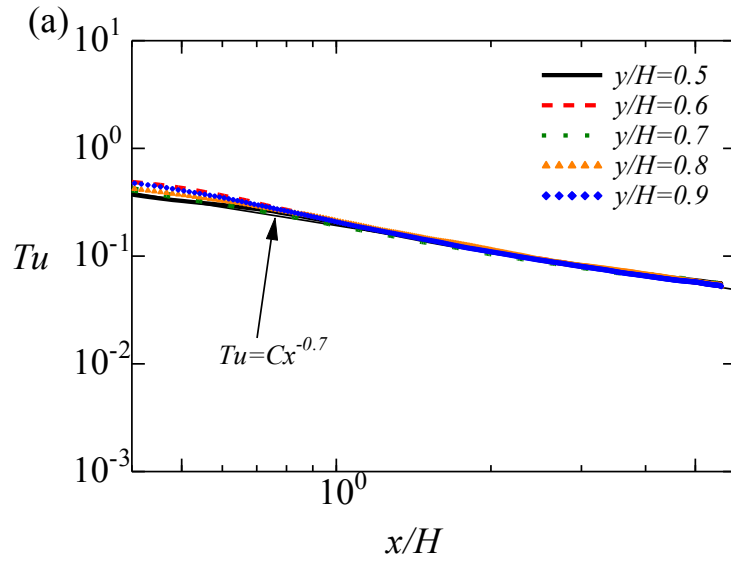
Fig. 4.2 (a) Turbulence intensity of the grid turbulence

(b)
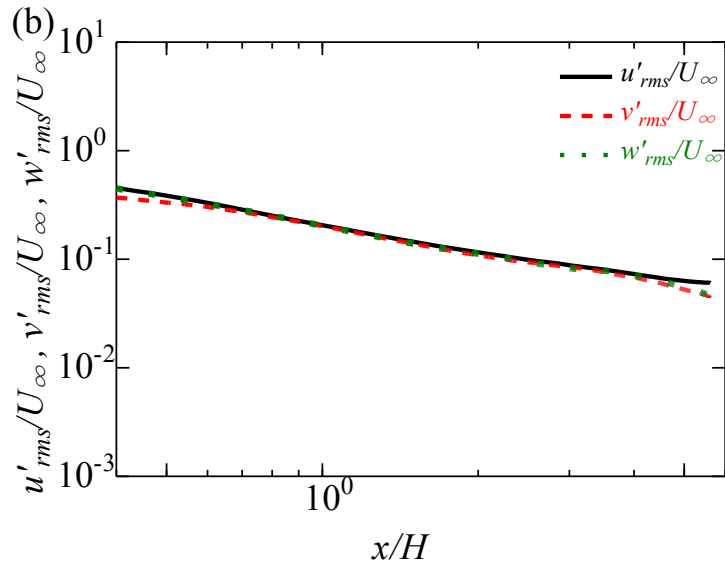
Fig. 4.2 (b) Rms velocity fluctuations of the grid turbulence
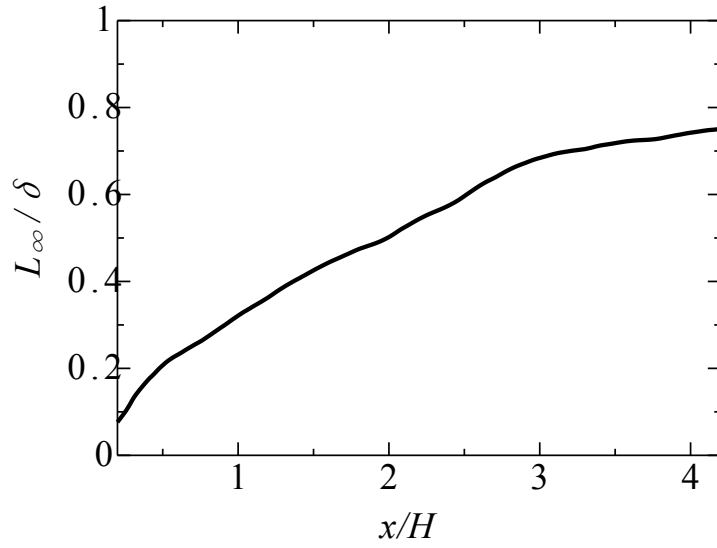
Fig. 4.3 Streamwise evolution of the integral length scale at $y/H = 0.7$
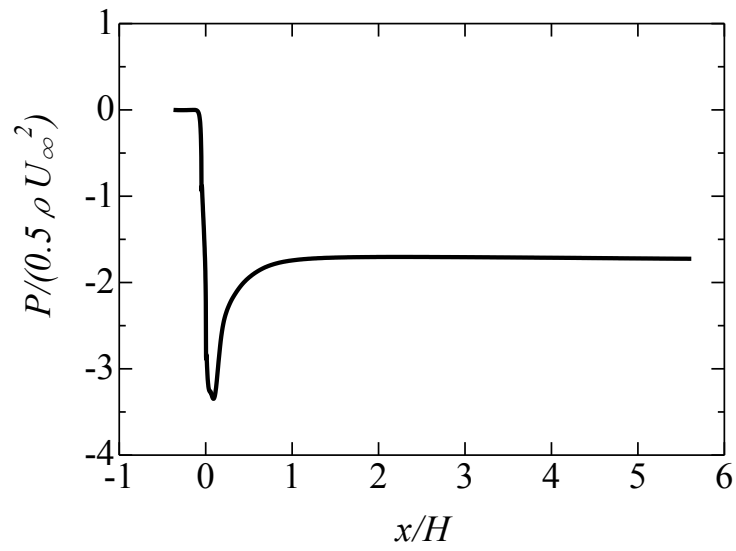
Fig. 4.4 Pressure drop

4.3.2 Instantaneous flow and thermal fields

Figures 4.5 and 4.6 show the instantaneous velocity and temperature fields on the $x-y$ plane at $z=0$, respectively. It is confirmed from Fig. 4.5 that the velocity boundary layer is developed spatially. The grid generates velocity fluctuations in the entire region and it interacts with the boundary layer. Similarly, the growth of the thermal boundary layer is also observed in Fig. 4.6. The thermal boundary layer is intensively deformed by the grid turbulence. Compared to the case with the tripping object (Fig. 3.4), heat transfer in the boundary layer under the effects of grid turbulence seems to be more significant, especially in the downstream region.

Figure 4.7 shows the instantaneous streamwise velocity fluctuations on the $x-z$ plane at different wall-normal locations. In the viscous sublayer ($y^+ = 3$), the streamwise velocity fluctuation field is organized into alternating streaks of high- and low-speed fluids. As moving away from the wall, these streaks undergo wavy motions in the buffer layer ($y^+ = 10$) and become less discernible as seen in the log-law layer ($y^+ = 70$). This confirms the typical structure in a turbulent boundary layer. As mentioned before, the streaks are the regions of high- and low-speed fluids formed by the longitudinal vortices. They are eventually lifted up from the wall and followed by a sudden loss of stability and a breakup, generating the bursting phenomenon which mostly occurs in the buffer layer. Thus, above the buffer layer, such streaks become less discernible.

4.3.3 Integral quantities

As shown in section 3.3.2, the development of boundary layer can be evaluated by the boundary layer thickness, δ, and the shape factor, $H_{12} = \delta^* / \theta$. Figure 4.8 shows the streamwise evolution of boundary layer thickness. The increase of boundary layer thickness along the streamwise direction is clearly observed. Compared to the case with the tripping object (Fig. 3.8), the boundary layer is thicker in the case with the grid turbulence.

The distribution of H_{12} against Re_θ is plotted in Fig. 4.9. The shape factor lies around 1.5 in the whole region. This coincides with the typical value in a turbulent boundary layer [79-81], suggesting that the boundary layer flow is in turbulent state under the effect of grid turbulence.
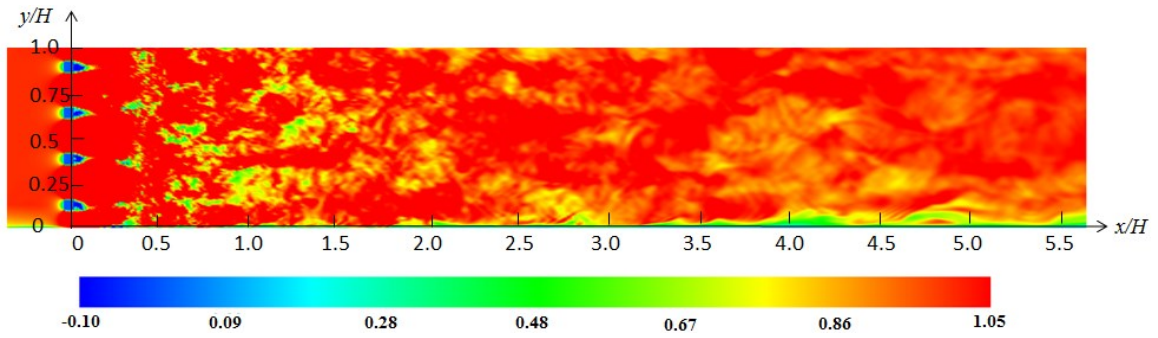
(a) Streamwise velocity
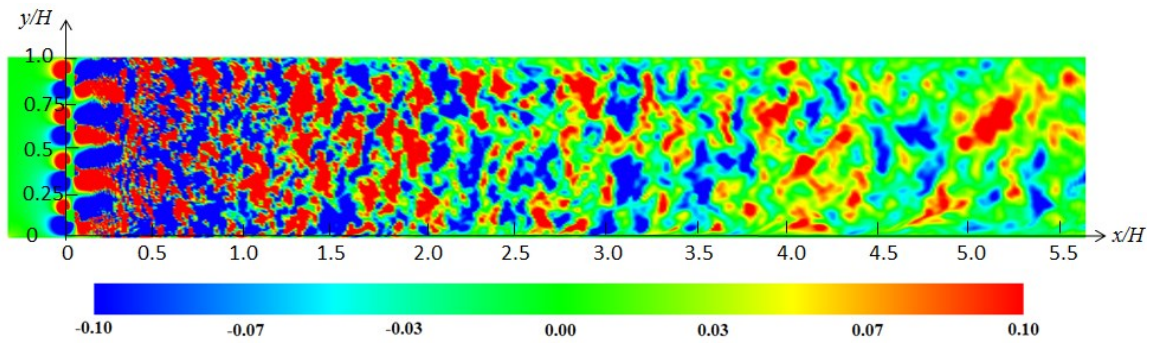
(b) Wall-normal velocity
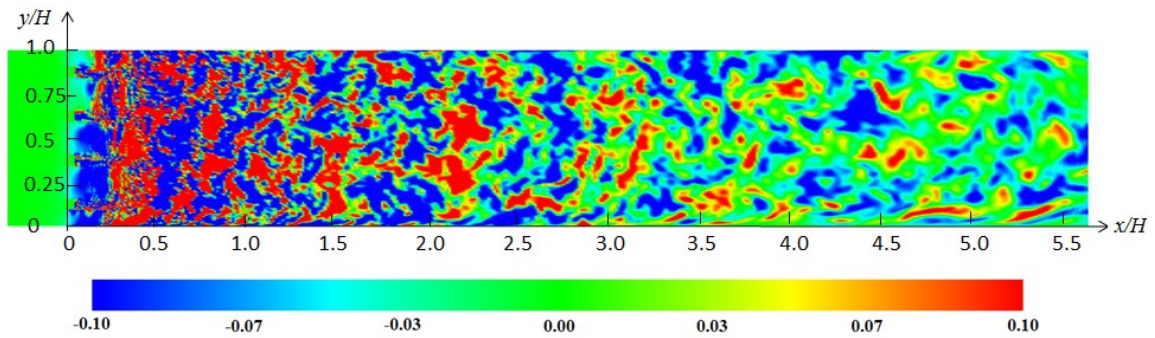
(c) Spanwise velocity

Fig. 4.5 Instantaneous velocity fields
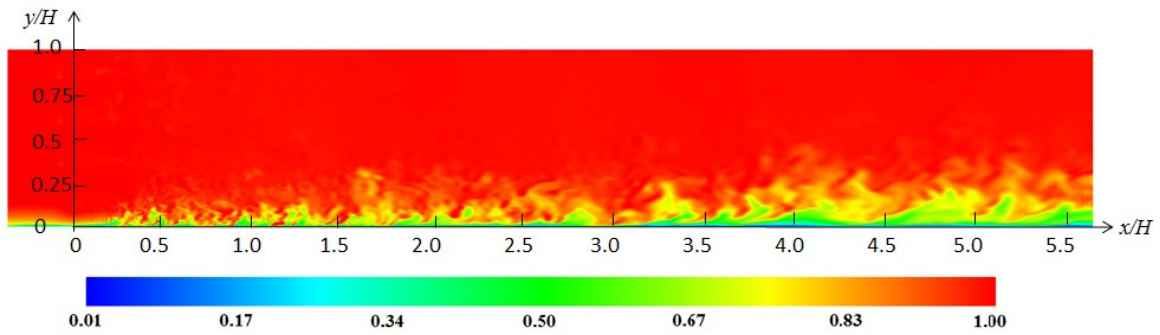
Fig. 4.6 Instantaneous temperature field
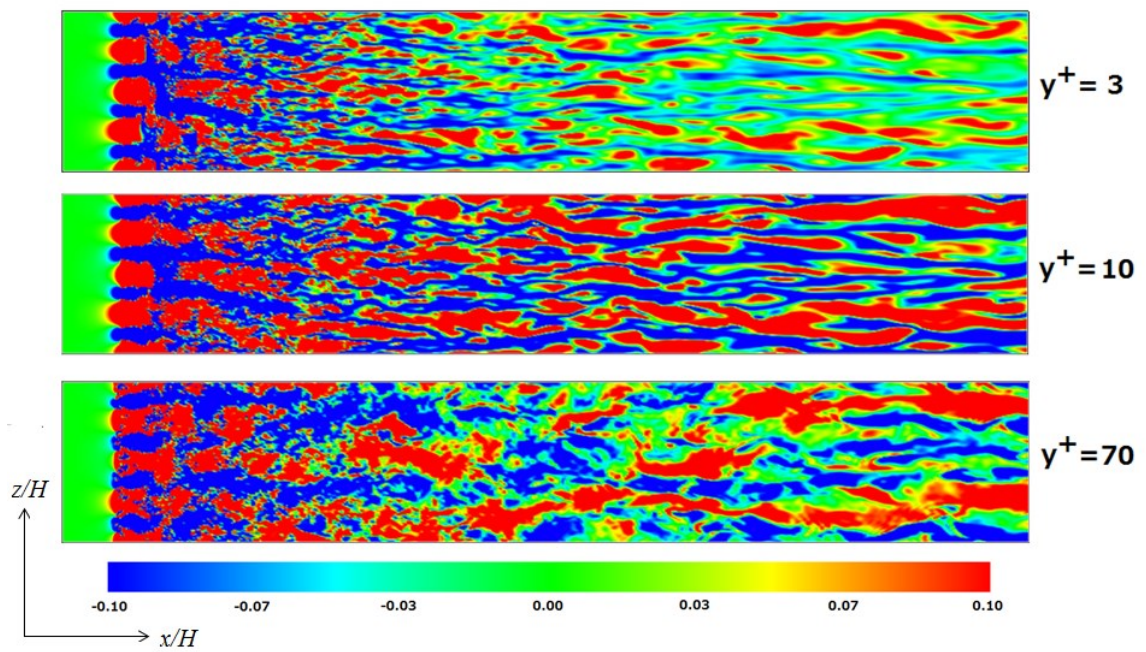
Fig. 4.7 Instantaneous streamwise velocity fluctuations
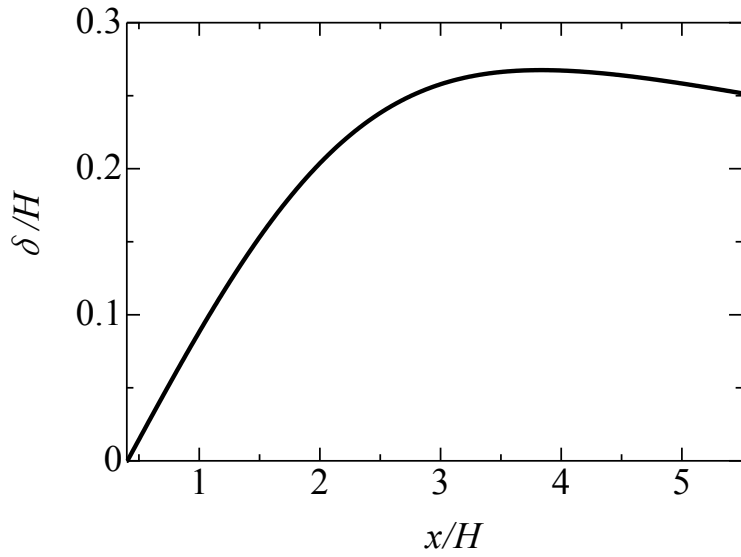
Fig. 4.8 Streamwise evolution of boundary layer thickness
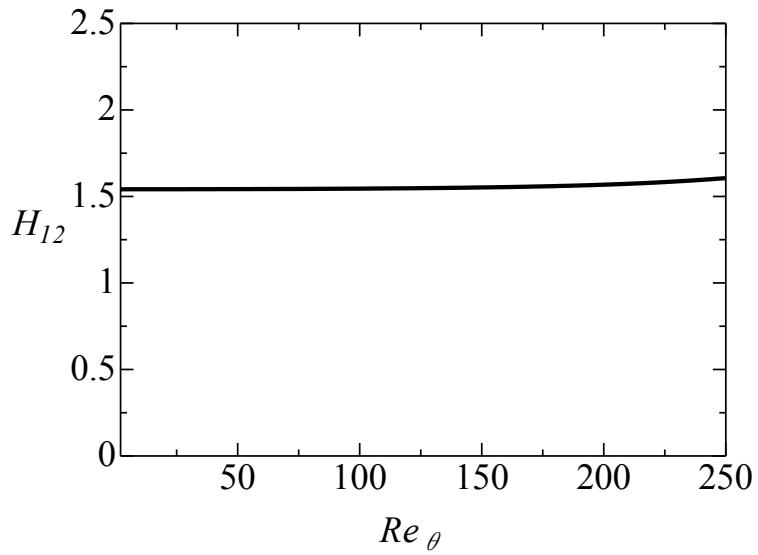
Fig. 4.9 Distribution of shape factor

4.3.4 Mean profiles

The wall-normal distribution of mean streamwise velocity and mean temperature at $x/H = 4$ ($Re_\theta = 250$) are shown in Figs. 4.10 and 4.11, respectively. Here, all the variables are normalized by the wall units. In this case, the results agree with those in the study by Li et al. [45], indicating the validation of present DNS. The results in the case with the tripping object at the same location are also included for comparison. Unlike the case with the tripping object, the profiles of U^+ and $\bar{T}^+$ in the case with the grid turbulence follow not only the linear distribution ($y^+ < 5$) but also the log-law distribution ($30 < y^+ < 100$) as seen in a typical turbulent boundary layer, meaning the boundary layer is in turbulent state under the effect of grid turbulence.

4.3.5 Fluctuation profiles

Figure 4.12 shows the streamwise evolutions of root-mean-square (rms) values of the velocity fluctuations. Comparing to the case with the tripping object, it is clearly seen that the velocity fluctuations generated by the grid are much larger. The non-zero values due to the grid turbulence are noticeable in the outer region of the boundary layer.

The wall-normal distributions of the Reynolds shear stress and the wall-normal heat flux at $x/H = 4$ ($Re_\theta = 250$) are plotted in Figs. 4.13 and 4.14, respectively. It is clearly observed, in the case with the grid turbulence, that both the Reynolds shear stress and the wall-normal heat flux are larger than those in the case with the tripping object.

The wall-normal distribution of the correlation coefficients, R_{uv} and R_{vT}, defined by Eqs. (3.9) and (3.10), at $x/H = 4$ ($Re_\theta = 250$) are plotted in Fig. 4.15. The results of a pure turbulent boundary layer (TBL) in the experiments by Chen and Blackwelder [84] are also included for comparison. In the case with the grid turbulence, R_{uv} increases near the wall and then decreases as y/δ increases. This trend differs from that in a pure TBL, implying the penetration of the uncorrelated u and v of the grid turbulence into the boundary layer, thereby reducing R_{uv}. On the other hand, R_{vT} increases near the wall and then level off at 0.5 within the range of $0.2 < y/\delta < 0.7$, which is in agreement with that in the experiments by Chen and Blackwelder [84] for a pure TBL.
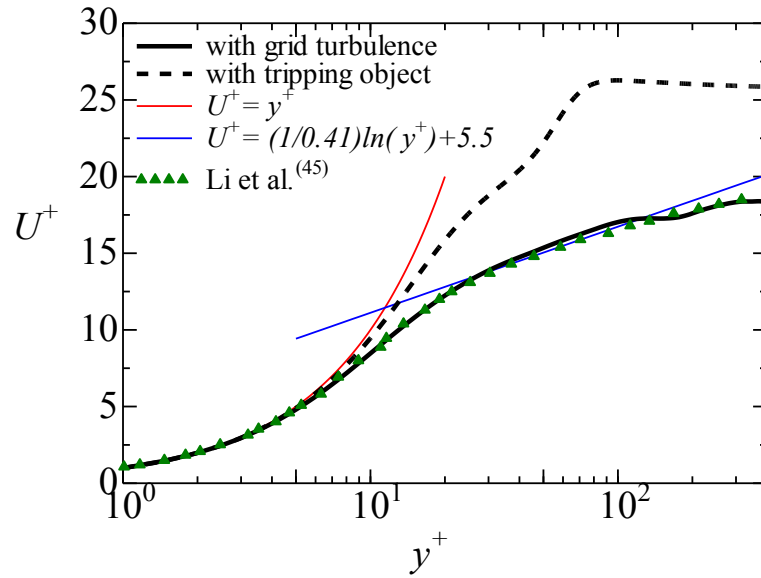
Fig. 4.10 Mean streamwise velocity profile
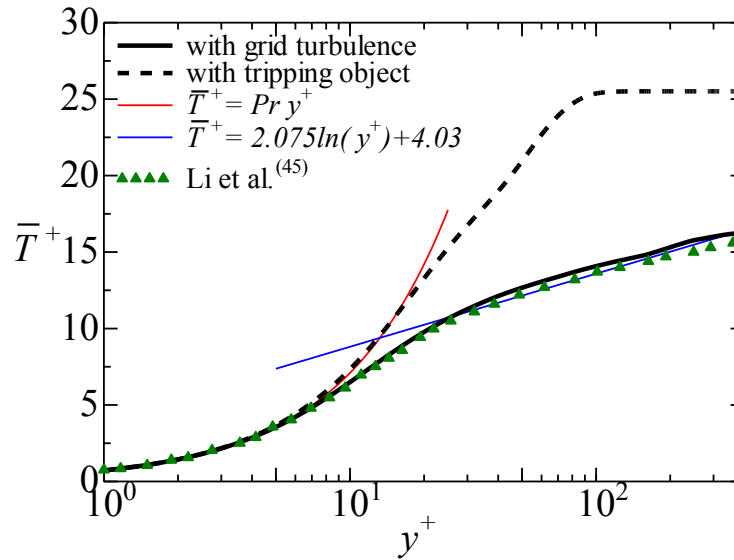
Fig. 4.11 Mean temperature profile
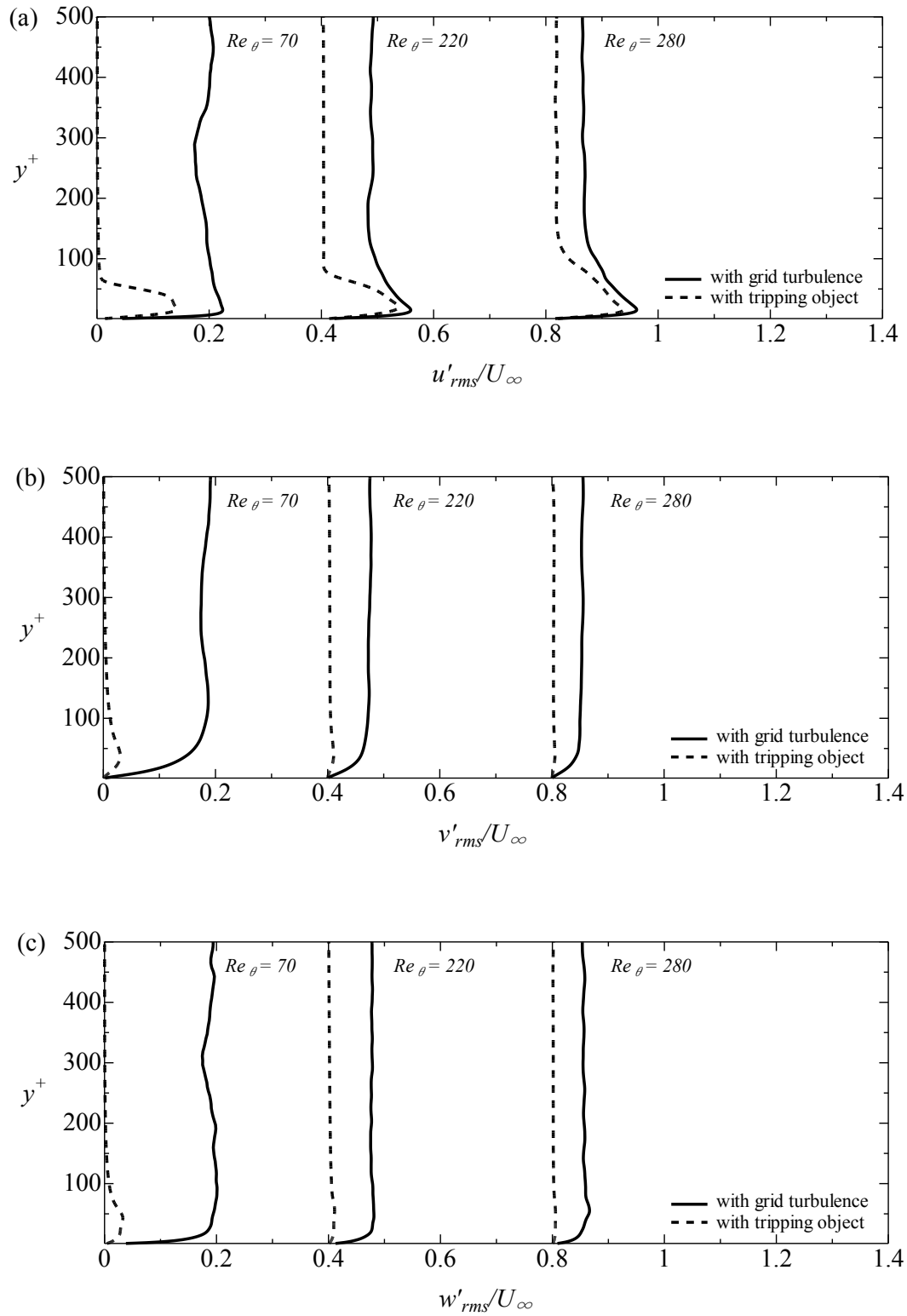
Fig. 4.12 Streamwise evolution of rms velocity fluctuations
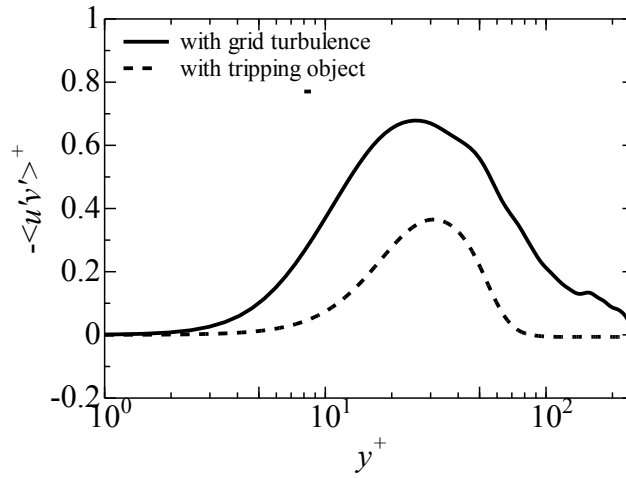
Fig. 4.13 Distribution of Reynolds shear stress at $x/H = 4$ ($Re_\theta = 250$)
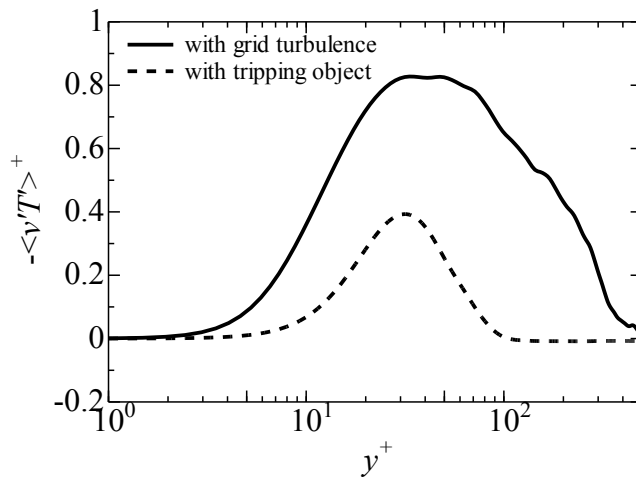
Fig. 4.14 Distribution of wall-normal heat flux at $x/H = 4$ ($Re_\theta = 250$)
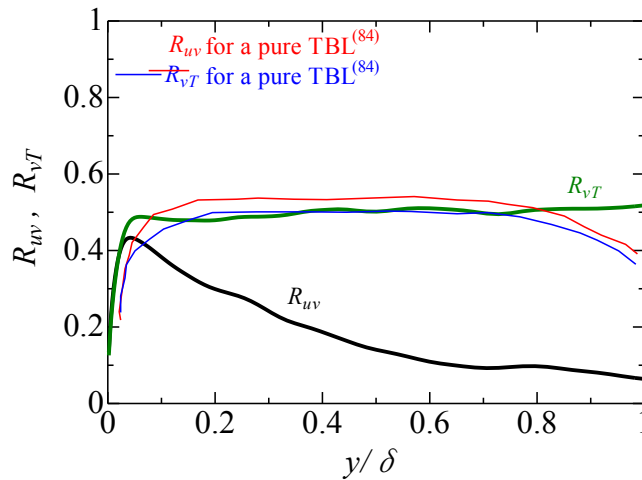
Fig. 4.15 Distribution of the correlation coefficients at $x/H = 4$ ($Re_\theta = 250$)

4.3.6 Wall quantities

Figures 4.16 and 4.17 shows the streamwise development of C_f and St, respectively. It is observed that C_f is larger than the typical value in a turbulent boundary layer (TBL) obtained by Karman and Schoenherr [90] in the region of $Re_\theta > 25$. A similar profiles of St is seen in Fig. 4.17. Here, the typical value of St for a TBL is derived from the Reynolds-Colburn analogy expressed in Eq. (3.15). In the case with the grid turbulence, St is larger than the typical value for a TBL in the region of $Re_\theta < 230$. This implies that both the skin friction and heat transfer are more enhanced by the grid turbulence.
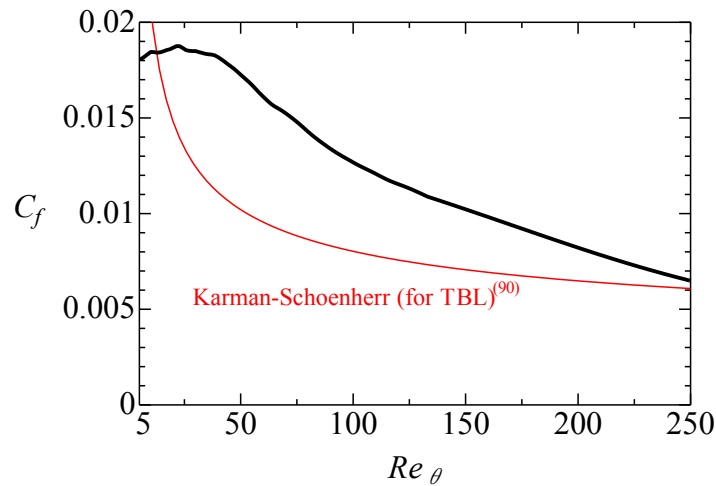
Fig. 4.16 Streamwise development of skin friction coefficient
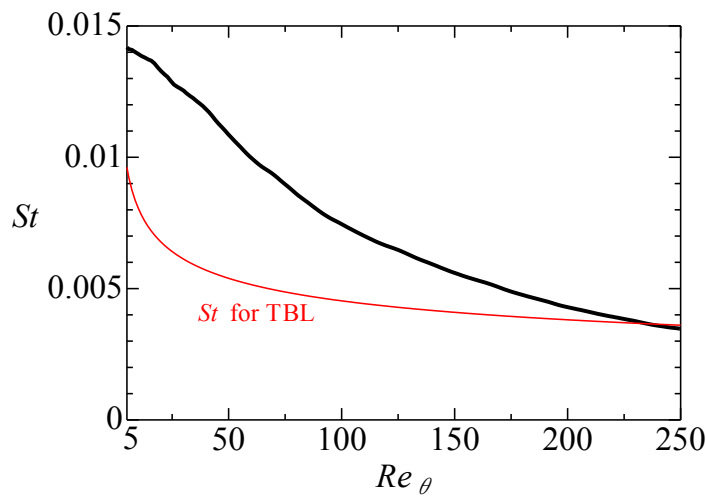
Fig. 4.17 Streamwise development of Stanton number

Figure 4.18 shows the streamwise distribution of $St/(C_f/2)$ in the case with the grid turbulence. It lies around 1.1 in the downstream region, indicating that the Reynolds analogy holds, i.e. momentum transfer is analogous to heat transfer. However, in the vicinity of the origin where the grid is placed, the analogy factor increases, implying that the Reynolds analogy does not hold in this region. This is mainly due to the high turbulence intensity generated by the grid turbulence.
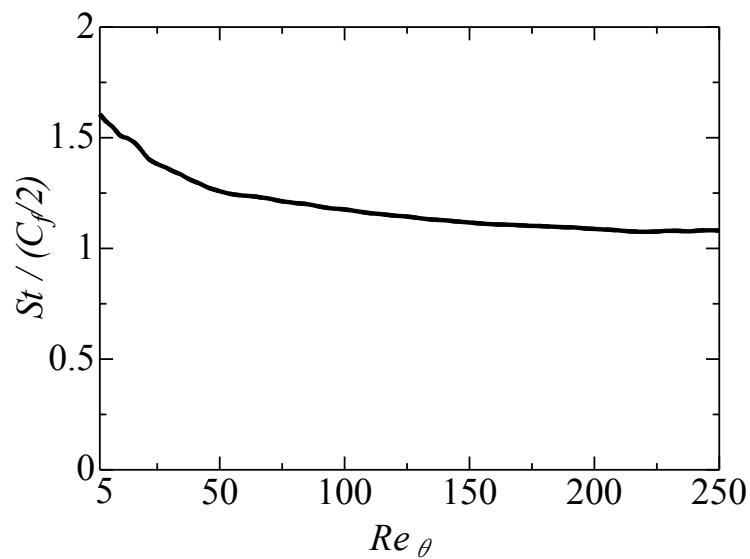
Fig. 4.18 The analogy factor
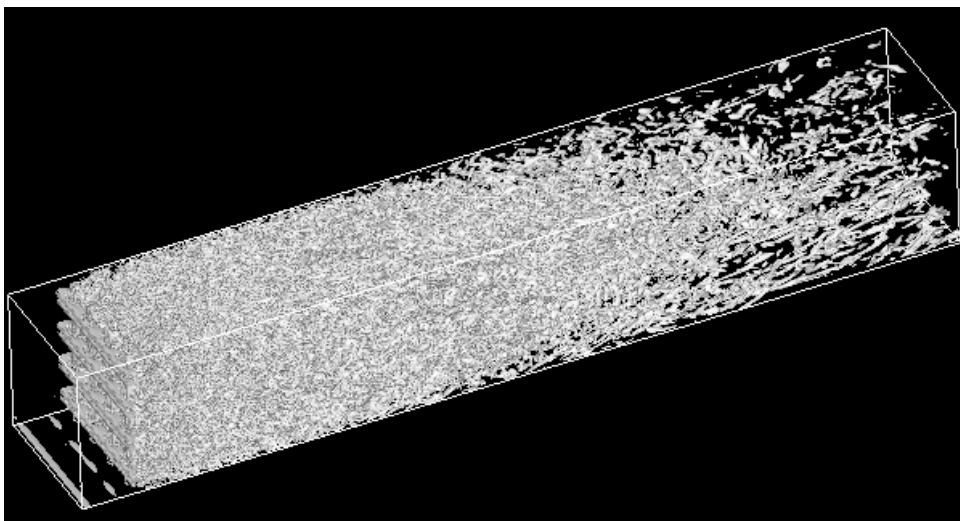
Fig. 4.19 Iso-surface of $Q=10$

4.3.7 Vortical motion and heat transfer

Vortical structure is visualized by the second invariant of velocity gradient tensor, Q, which is defined by Eq. (3.16). Figure 4.19 shows the iso-surface of $Q=10$ in space in the case with the grid turbulence. The vortical structures of the grid turbulence are clearly observed. As moving to the downstream region, these structures become less clear because of the energy decay of the grid turbulence.

On the other hand, the vortical motions in the near-wall region are of special interest and their contribution to the enhancement of heat transfer is investigated. Figure 4.20 shows the visualized instantaneous heat transfer coefficient, h, on the $x-z$ plane close to the wall. Figures 4.21 and 4.22 show the visualized second invariant of velocity gradient tensor, Q, on the $x-z$ plane at $y^+ = 5$ (in the viscous sublayer) and at $y^+ = 10$ (in the buffer layer), respectively. Here, h and Q are defined by Eqs. (3.14) and (3.16), respectively. It is known that Q gives a measure of the relative intensity of strain and rotation. $Q < 0$ means that the strain ($Q_s = -\frac{1}{2} S_{ij} S_{ij}$) dominates over the rotation ($Q_w = \frac{1}{2} W_{ij} W_{ij}$), i.e. the flow has a sheet-like structure. On the other hand, $Q > 0$ means that the rotation dominates over the strain, i.e. the flow is more close to a tube-like structure. Comparison between Figs. 4.20 and 4.21 tells us that large h appears where Q is mostly negative at $y^+ = 5$, as marked by dashed circles. This indicates that strong strain in the viscous sublayer contributes to the enhancement of heat transfer. From Fig. 4.22, it is found that the rotation motion ($Q > 0$) is active above the region where the strong strain is dominated. It implies that the strong-strain regions in the viscous sublayer are induced by the rotation motions in the buffer layer. According to the streamwise vortex model proposed by Kim et al., [1] as shown in Fig. 4.23, such rotation motion is induced by the streamwise vortex in the buffer layer. These analyses lead to a conclusion that strong strain in the viscous sublayer, which is induced by the vortical motion in the buffer layer, contributes to the enhancement of heat transfer in the case with the grid turbulence.
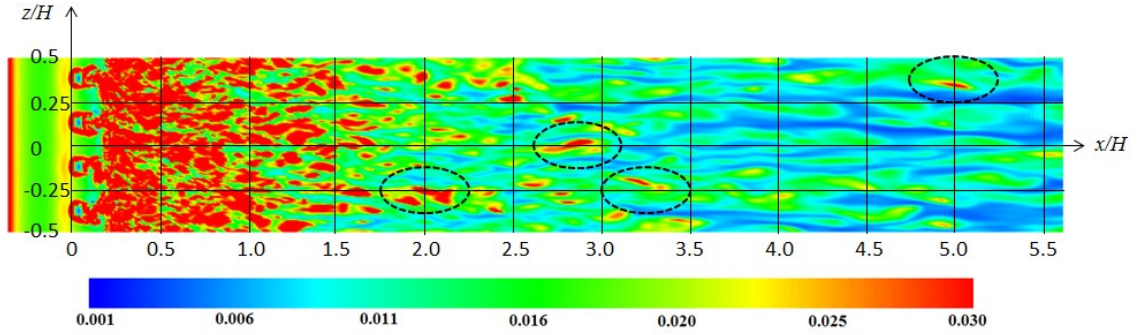
Fig. 4.20 h on $x - z$ plane close to the wall (red: high; blue: low)
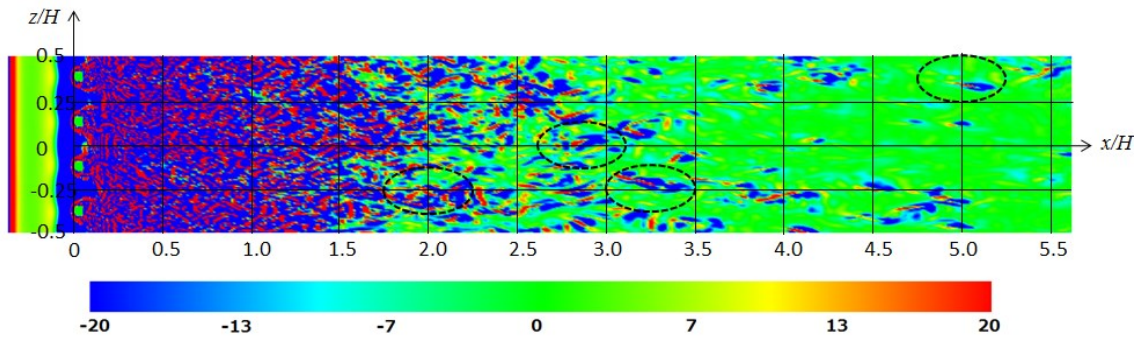
Fig. 4.21 Q on $x - z$ plane at $y^+ = 5$ (red: positive; blue: negative)
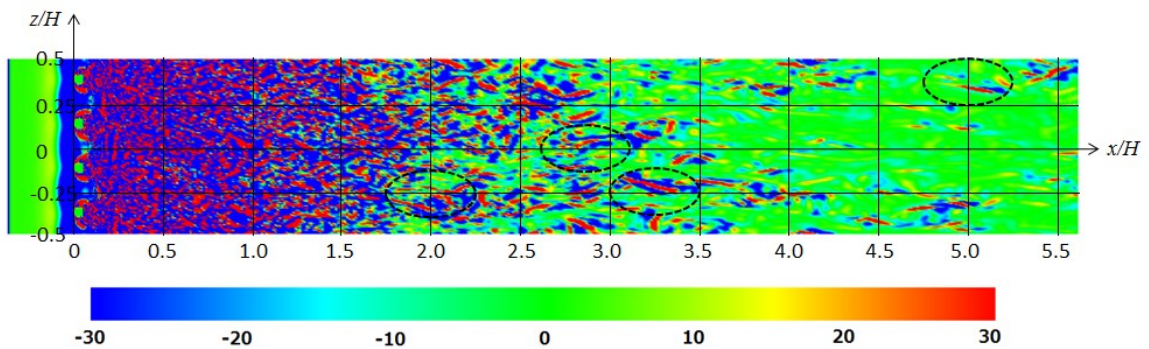
Fig. 4.22 Q on $x - z$ plane at $y^+ = 10$ (red: positive; blue: negative)
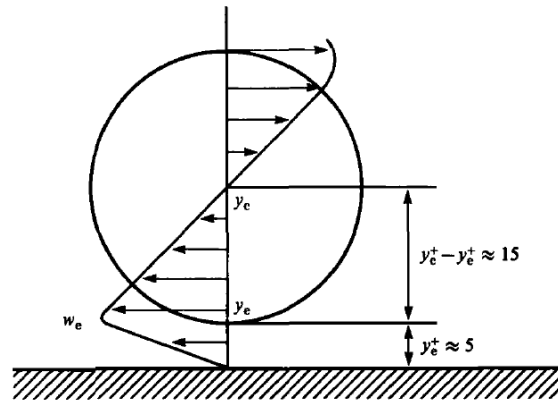
Fig. 4.23 A streamwise vortex model proposed by Kim et al. [1]

4.4 Summary

In this chapter, DNS of a boundary layer with heat transfer subjected to the external disturbance generated by a regular grid has been performed to investigate the effects of such disturbance on the flow field and heat transfer in the boundary layer. The results are summarized as follows:

(1) The boundary layer is triggered by the regular grid and the boundary layer flow becomes the turbulent state even though Re_θ is low.

(2) Skin friction and heat transfer in the boundary layer are more enhanced by the grid turbulence.

(3) Strong strain in the viscous sublayer, which is induced by the vortical motion in the buffer layer, contributes to the enhancement of heat transfer.

Chapter 5

Boundary Layer with Heat Transfer under the Effects of a Wake of a Square Bar [91]

5.1 Introduction

Many flows of industrial importance can be idealized as the interaction of the wake with a boundary layer. The large scale motions of the wake strongly affect the boundary layer. In this chapter, the development of a boundary layer with heat transfer under the effects of a wake of a square bar is investigated by a three-dimensional direct numerical simulation (DNS).

5.2 Numerical Details

Figure 5.1 shows the schematic of the computational domain. A square bar with its axis parallel to the bottom wall and normal to the flow direction is placed at a location of $3d$ downstream from the inlet. The gap between the square bar and the bottom wall, C, is set to $0.25d$ (hereafter referred to as the small-gap case) and $3d$ (hereafter referred to as the large-gap case). Table 5.1 shows the size of the computational domain and the mesh numbers. Similar to that shown in Fig. 3.2, the mesh spacing is uniform in the spanwise direction but non-uniform in the streamwise and wall-normal directions with refined mesh in the vicinity of the square bar and near the wall. Note that fifteen mesh points in the wall-normal direction are set within the viscous sublayer to meet the requirement for catching the smallest structure in the boundary layer [76]. In addition, the spatial resolutions normalized by the wall units are $\Delta x^+ = 0.67 \sim 6$, $\Delta y^+ = 0.26 \sim 3$, and $\Delta z^+ = 3$, which are in agreement with pervious simulations [77-78], ensuring the accuracy of the spatial resolutions.

In this case, the numerical schemes and boundary conditions are the same as those in the cases with the tripping object and with the grid turbulence. Here, the Reynolds number,

$Re_d = U_\infty d/\nu$, is set to 1667 and Prandtl number, Pr, is set to 0.71. The computational time step normalized by the free-stream velocity, U_∞, and the side length of the square bar, d, is set to 0.0016, which corresponds to a maximum Courant-Friedrichs-Lewy condition of $CFL_{max} = 0.37$.
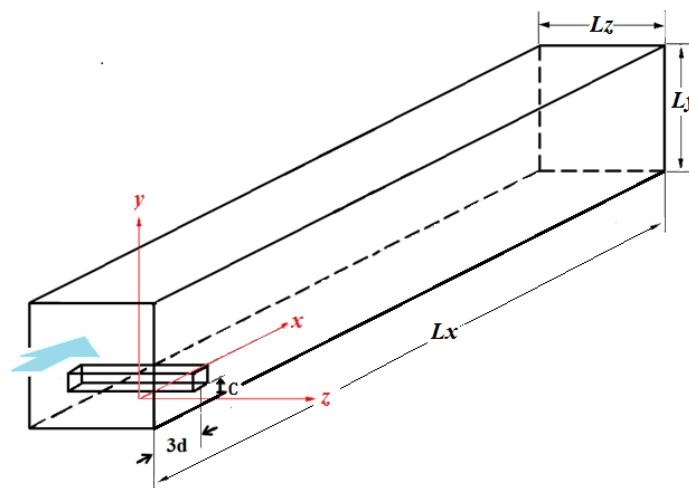
Fig. 5.1 Schematic of the computational domain

Table 5.1 Computational domain size and mesh numbers

Domain size $L_x \times L_y \times L_z$	$30d \times 8d \times 8d$
Mesh number $N_x \times N_y \times N_z$	$444 \times 200 \times 160$

5.3 Results and Discussion

5.3.1 Instantaneous flow and thermal fields

Figure 5.2 shows the instantaneous streamwise velocity (background color) along with the velocity vector on the $x-y$ plane at $z=0$. It is confirmed that the boundary layer is triggered by and interacts with the wake. In the small-gap case ($C/d=0.25$), the wake merges with the boundary layer immediately after shedding from the square bar. On the other hand, in the large-gap case ($C/d=3.0$), the wake starts to merge with the boundary layer some distance downstream ($x/d>10$). It is known that the merging distance depends on the propagation speed of the vortices, the boundary layer growth rate, and the gap between the square bar and the bottom wall. Comparing to the large-gap case, large recirculating regions are observed in the small-gap case particularly in the upstream region. This results in the thicker boundary layer in the small-gap case.
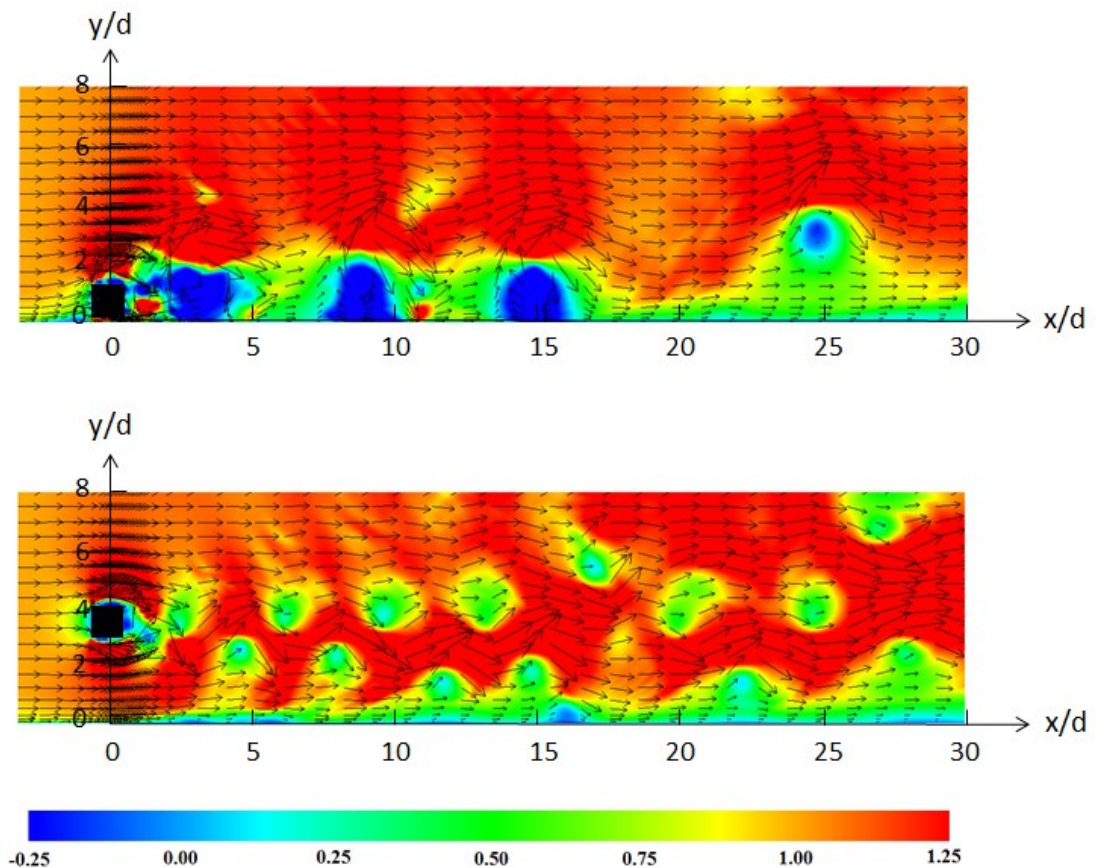
Fig. 5.2 Instantaneous streamwise velocity fields (background color) and velocity vector. Upper image: $C/d=0.25$; lower image: $C/d=3.0$.
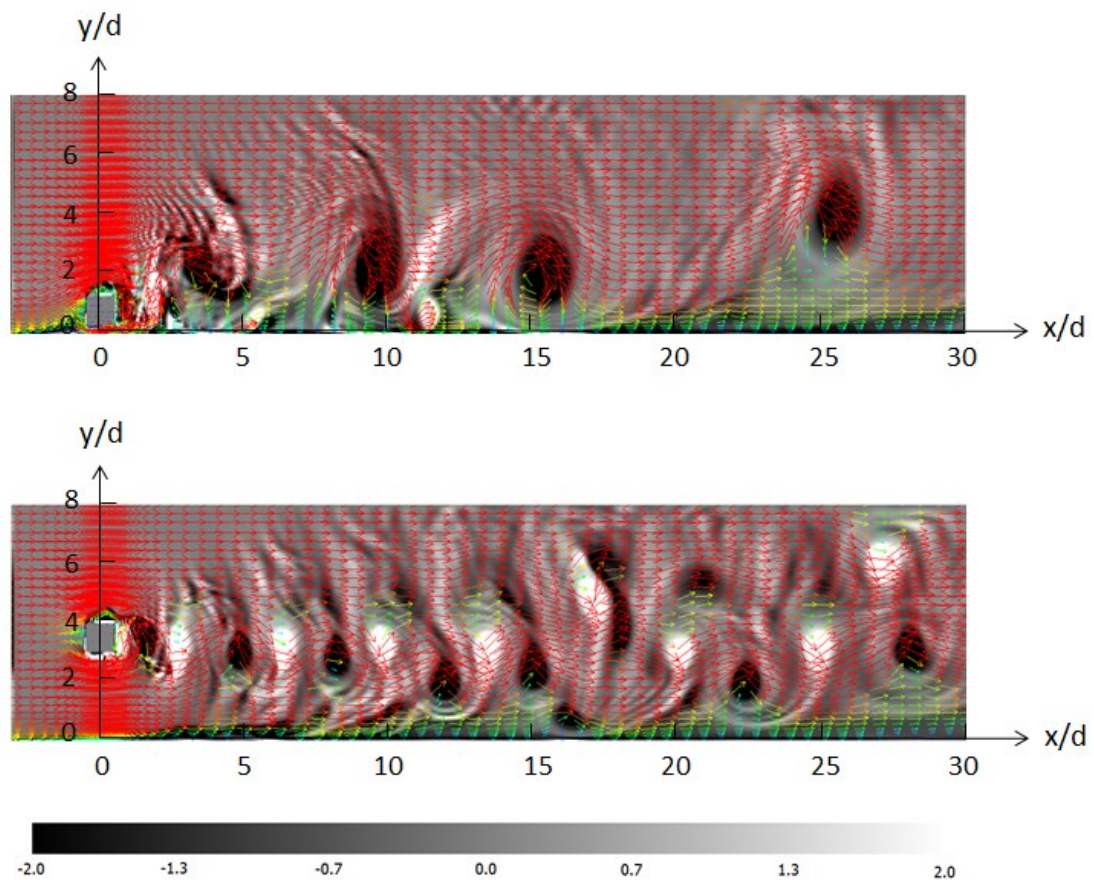
Fig. 5.3 Normalized instantaneous spanwise vorticity fields (black and dark gray: negative/clockwise; white and light gray: positive/counter-clockwise) and velocity vector (red: high-speed; blue: low-speed). Upper image: $C/d = 0.25$; lower image: $C/d = 3.0$.

Figure 5.3 shows the normalized instantaneous spanwise vorticity, $\omega_z d / U_\infty$, in a form of color contour (black: negative; white: positive) and the velocity vector (red: high-speed; blue: low-speed) on the $x-y$ plane at $z = 0$. In the small-gap case, the negative (clockwise) vortices shed from the upper side of the square bar are large and occupy almost the entire region near the bottom wall, while the positive (counter-clockwise) vortices shed from the lower side of the square bar are small. It is also observed that strong backward sweep motions of fluid, induced by the large negative vortices, exist near the bottom wall. This leads to the large reversed flow regions observed in Fig. 5.2. On the other hand, in the large-gap case, the negative and positive vortices of the same size, are shed from the square bar alternatively and perturb the flow by advecting the fluid wallward and outward in turn.

Furthermore, it is found that, as the vortices move downstream, they do not remain on the same side where they originally shed: the negative vortices shed from the upper side get close to the wall boundary layer and occupy the lower position in the downstream region, while the positive vortices shed from the lower side goes up and occupy the upper position. This behavior confirms the "crisscross motion" found by Suzuki et al. [92-93]. As a result, the negative vortices mostly interact with the boundary layer.
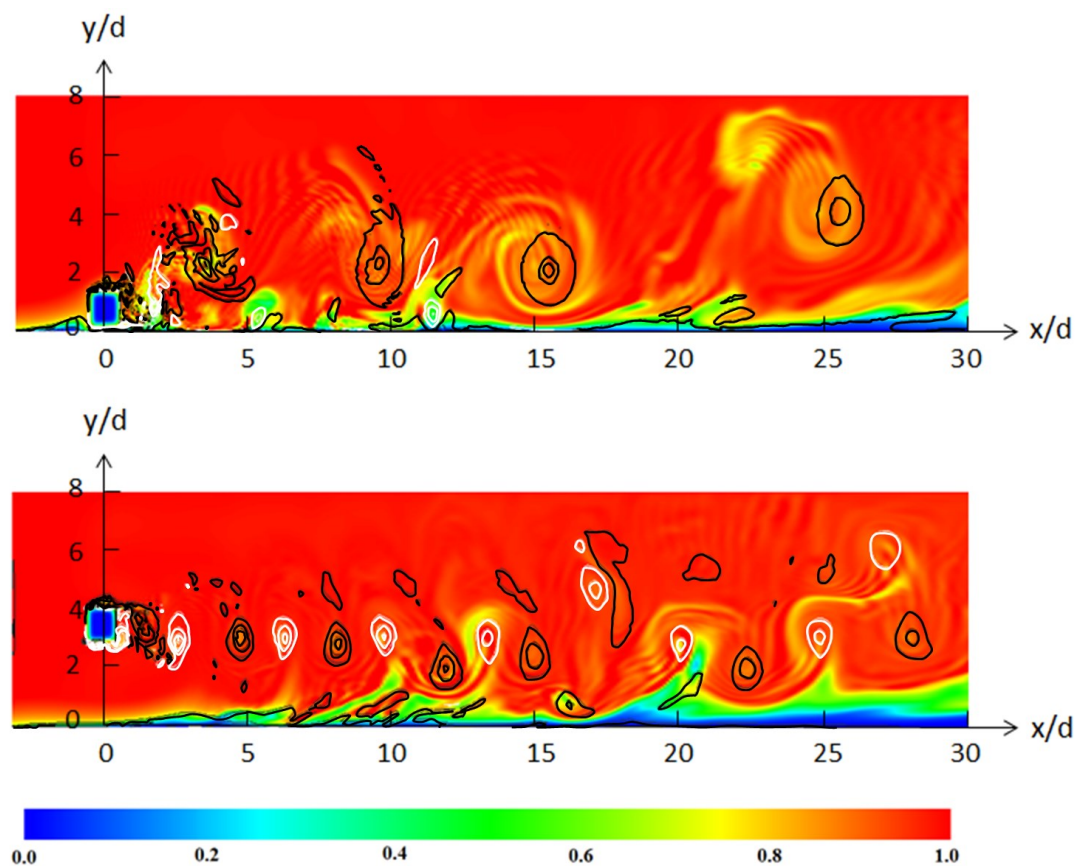
Fig. 5.4 Instantaneous temperature fields with the iso-vorticity line (black: negative/clockwise; white: positive/counter-clockwise). Upper image: $C/d = 0.25$; lower image: $C/d = 3.0$.

Figure 5.4 shows the instantaneous temperature fields in a form of color contour along with the iso-vorticity line (black: negative; white: positive). It is observed that the thermal boundary layers are developed spatially and disturbed by the wakes in both cases. The negative (clockwise) vortices generally suppress the thermal boundary layer by engulfing the hot fluid from the outer region into the near-wall region, which makes the temperature

gradient large. On the other hand, the positive (counter-clockwise) vortices seem to stretch the thermal boundary layer by ejecting the cold fluid from the near-wall region into the outer region and it makes the temperature gradient small. In the small-gap case, the effect of the positive vortices is small due to its smallness in size and less in number and the main effect comes from the large negative vortices that strongly suppress the thermal boundary layer. In the large-gap case, however, not only the negative vortices but also the positive vortices affect the thermal boundary layer. Furthermore, the negative vortices are smaller and exist far away from the plate ($y/d > 2$) in comparison with the small-gap case. Therefore, the suppression effect by the negative vortices in this case is relatively weak. As a result, the thermal boundary layer in the small-gap case is strongly suppressed by the large negative vortices in comparison with the large-gap case. This leads to the thinner thermal boundary layer, hence the larger temperature gradient.
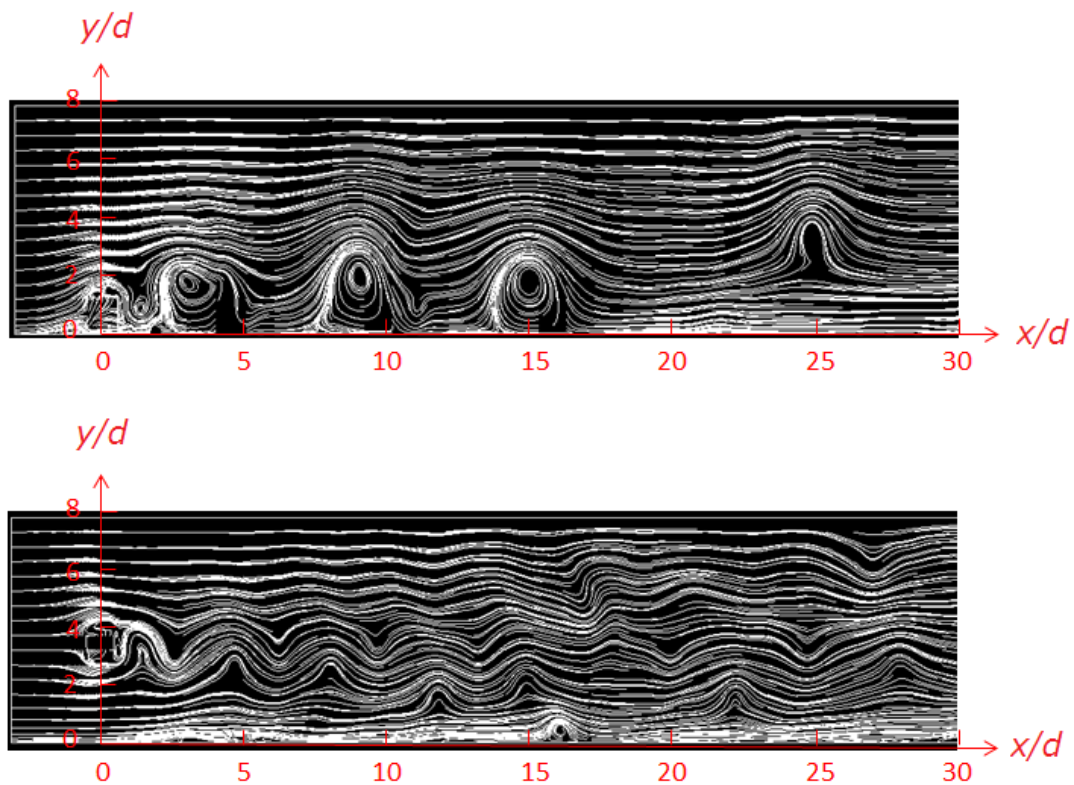
Fig. 5.5 Instantaneous streamline fields. Upper image: $C/d = 0.25$; lower image: $C/d = 3.0$.

The instantaneous streamline in the two cases is shown in Fig. 5.5. It is clear that the vortex shedding in the Von Karman vortex street interferes with the wall boundary layer. In the small-gap case, the large recirculation regions are observed in the upstream region. This is attributed to the strong backward sweep motions of fluid induced by the large negative vortices as seen in Fig. 5.3. On the other hand, in the large-gap case, a small recirculation region in the boundary layer is created while the shed vortices approach the boundary layer, and it rolls over the bottom wall.

5.3.2 Integral quantities

Comparing the flow fields in Figs. 3.3(a), 4.5(a) and 5.2, it is indicated that the boundary layer development is affected by the way that it is triggered. A direct and overall assessment of the boundary layer development can be obtained by the boundary layer thickness, δ, as well as the displacement thickness, δ^*, and the momentum thickness, θ. Figure 5.6 shows the streamwise evolution of the boundary layer thickness in the case with the square bar. In the small-gap case ($C/d = 0.25$), δ is larger than that in the large-gap case ($C/d = 3.0$). This confirms the former observation in the instantaneous velocity fields that the boundary layer is thicker in the small-gap case.

In addition, the shape factor, $H_{12} = \delta^*/\theta$, is considered to be a good indicator of the boundary layer state. Based on the Blasius solution, the value of H_{12} is about 2.6 in a laminar boundary layer. In a turbulent boundary layer, on the other hand, it is around 1.5 obtained by previous studies [79-81]. The distribution of H_{12} along the streamwise direction is plotted in Fig. 5.7. It is observed that H_{12} in the small-gap case is smaller than that in the large-gap case, especially in the downstream region, but both of them are smaller than the laminar value ($H_{12} \approx 2.6$) and does not approach the turbulent value ($H_{12} \approx 1.5$). It implies that the boundary layer flows in the two cases are still in transition.
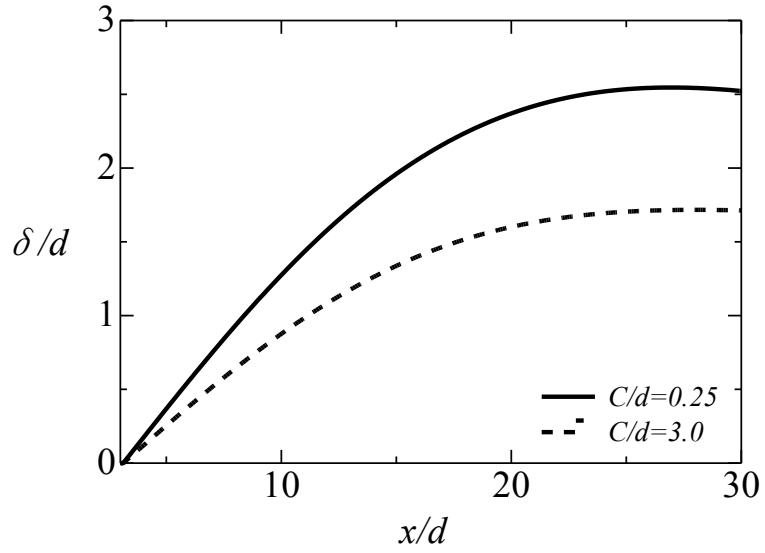
Fig. 5.6 Streamwise evolution of boundary layer thickness
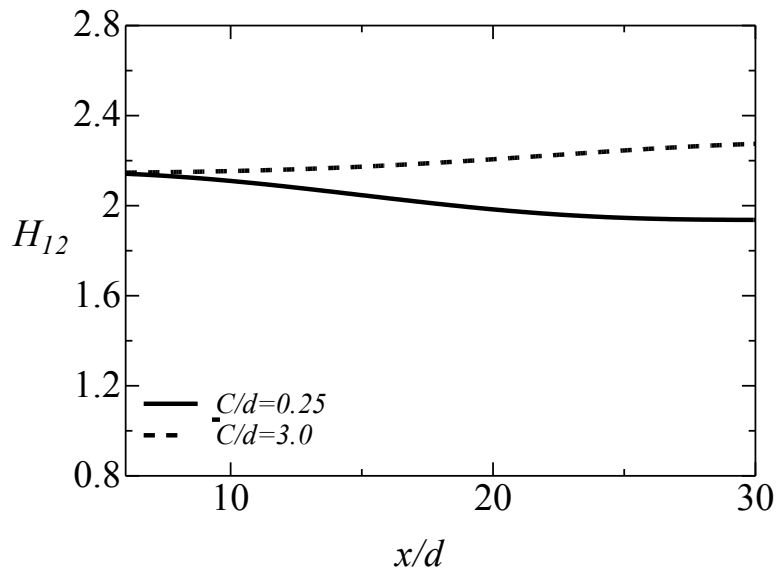
Fig. 5.7 Streamwise distribution of shape factor

5.3.3 Mean profiles

In this part, the mean profiles of streamwise velocity and temperature are presented to discuss the influence of the wake on the flow and thermal fields. Figure 5.8 shows the mean streamwise velocity profiles at different streamwise locations. In the large-gap case ($C/d = 3.0$), velocity defect due to the presence of the square bar appears behind the bar. It gradually disappears with increasing the streamwise distance and the profile becomes smooth at $x/d = 5$. However, in the region of $x/d > 5$, the mean streawise velocity distribution fluctuates again. This phenomenon can be explained by the migration of vortices. Figure 5.9 shows the time sequence of the normalized spanwise vorticity, $\omega_z d/U_\infty$, in the large-gap case. The negative vortex A (Fig. 5.9a) moves downstream as shown in Figs. 5.9b and 5.9c. At the same time, the tip of vortex B in the boundary layer (Fig. 5.9b) is lifted up gradually and detaches from the bottom wall as an isolated vortex (Fig. 5.9d). Meanwhile, the elongated vortex A breaks up into two vortices (A1 and A2): the main vortex A1 interacts with the isolated vortex B (Fig. 5.9e) and moves into the lower position with respect to the positive vortex C (Fig. 5.9f), while the other vortex A2 stays in the upper position with respect to positive vortex C (Fig. 5.9e) and disappears gradually (Fig. 5.9f). Such migration of the negative and positive vortices along the wall-normal direction leads to the fluctuation in the mean streamwise velocity profile. Note that the negative vortices tend to align at $y/d = 2 \sim 3$ and as a result, the flow at $y/d = 3 \sim 4$ is accelerated in the region of $x/d > 10$. On the other hand, in the small-gap case ($C/d = 0.25$), the reversed flow in the region of $x/d < 5$ is observed, indicating the influence from the large negative vortices as shown in Fig. 5.3. In addition, as moving to the downstream, the mean streamwise velocity profile near the bottom wall becomes almost the same as that in the large-gap case.
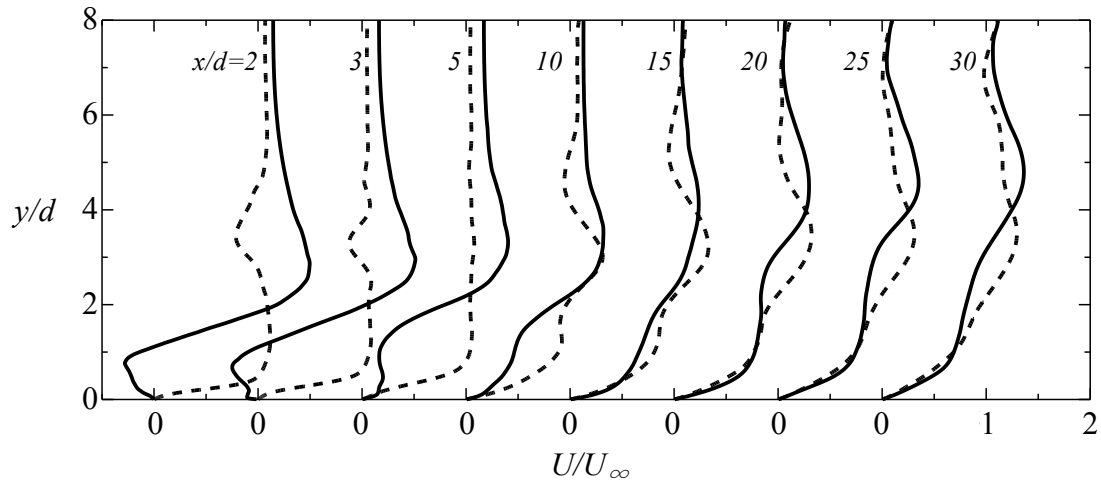
Fig. 5.8 Mean streamwise velocity profile. Solid line: $C/d = 0.25$; dash line: $C/d = 3.0$.
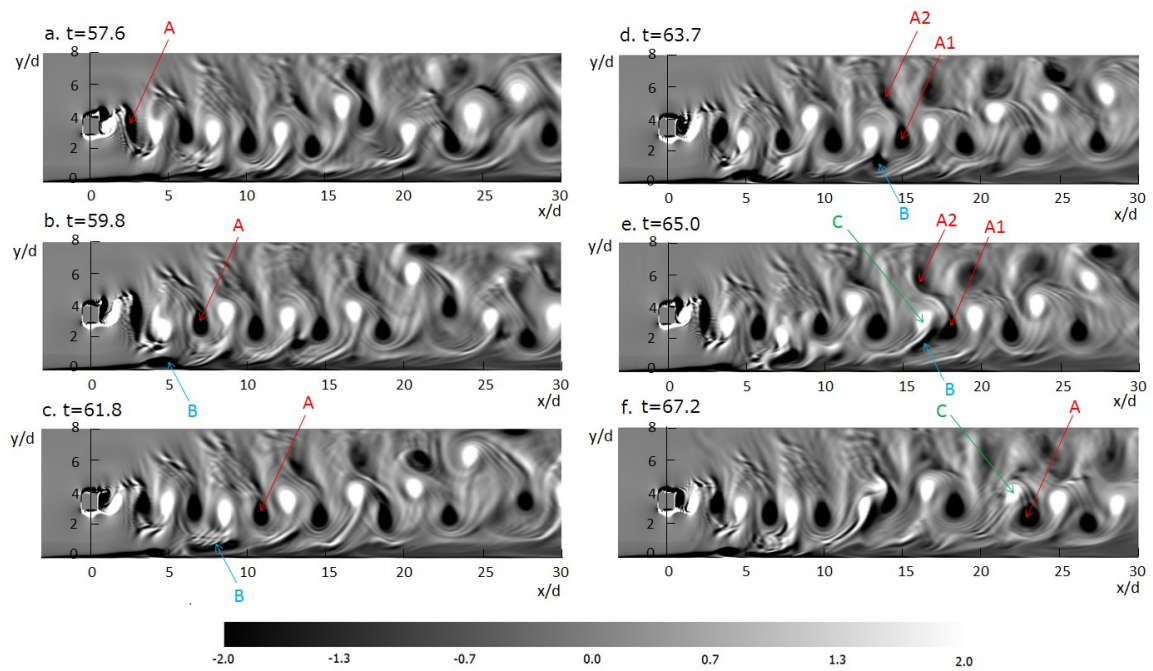
Fig. 5.9 Time sequence of the normalized spanwise vorticity field in the case of $C/d = 3.0$ (black and dark gray: negative; white and light gray: positive)
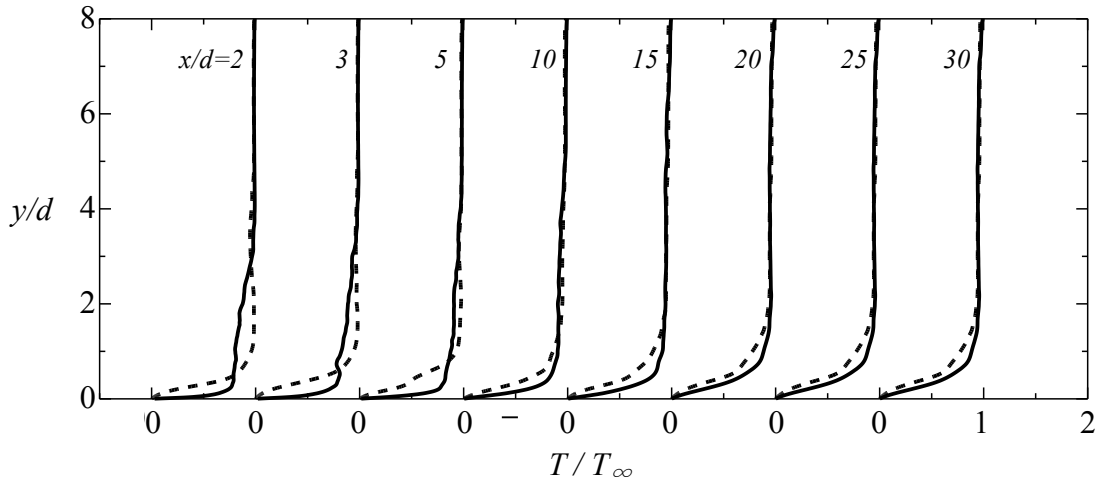
Fig. 5.10 Mean temperature profile. Solid line: $C/d = 0.25$; dash line: $C/d = 3.0$.

The mean temperature profiles of the two cases at different streamwise locations are plotted in Fig. 5.10. It shows that the temperature gradient in the small-gap case ($C/d = 0.25$) is larger than that in the large-gap case ($C/d = 3.0$), especially in the upstream region. As shown in the instantaneous temperature fields (Fig. 5.4), it has been known that the thermal boundary layer in the small-gap case is strongly suppressed by the large negative vortices in comparison with the large-gap case. Consequently, more hot fluid is engulfed from the outer region into the near-wall region, which results in the larger temperature gradient in the small-gap case.

5.3.4 Wall quantities

Figures 5.11 and 5.12 show the streamwsie development of two important wall quantities, the skin friction coefficient, $C_f = \tau_w / (\rho U_\infty^2 / 2)$, and Stanton number, $St = h/(\rho C_p U_\infty)$, respectively. It is found that C_f in the small-gap case is smaller than that in the large-gap case in the region of $x/d < 20$. As shown in Fig. 5.3, the strong backward sweep motions of fluid induced by the negative vortices exist near the bottom wall in the small-gap case. Hence, the velocity is reduced, resulting in the reduction in skin friction. In the downstream region, the values of C_f in the two cases are almost the same.

On the other hand, St in the small-gap case is larger than that in the large-gap case, especially in the upstream region. In other words, heat transfer is more active in the small-gap case. This is due to the existence of the large negative vortices, by which the thermal boundary layer is strongly suppressed (Fig. 5.4) and the temperature gradient is made larger (Fig.5.10).
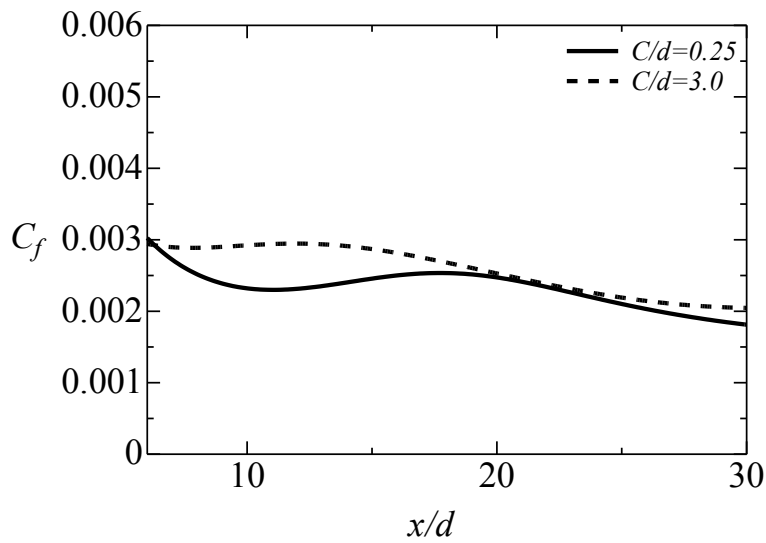
Fig. 5.11 Streamwise development of skin friction coefficient
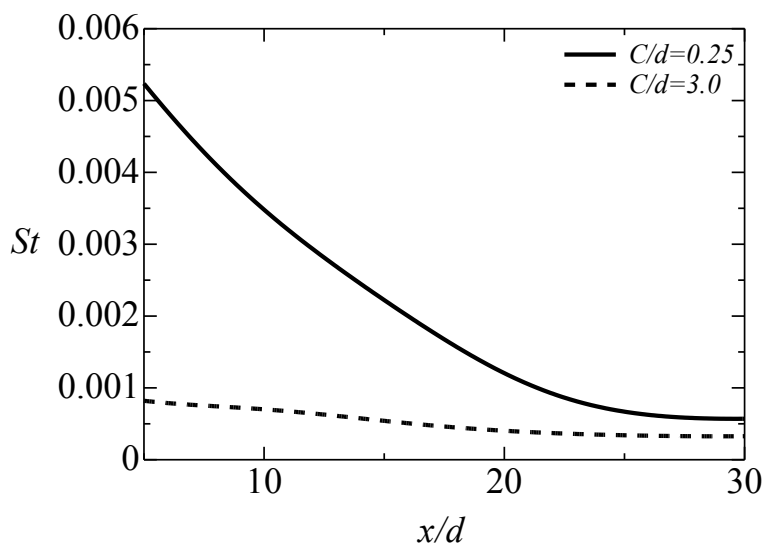
Fig. 5.12 Streamwise development Stanton number

5.4 Summary

In this chapter, the development of a boundary layer with heat transfer under the effects of a wake of a square bar with different gaps has been investigated by means of direct numerical simulation (DNS). The results are summarized as follows:

(1) The boundary layers have been triggered by the wakes of the square bar and the flows in these boundary layers are to some extent transitional.

(2) In the large-gap case ($C/d = 3.0$), the alternating negative and positive vortices, shed from the bar, perturb the boundary layer by advecting the fluid wallward and outward in turn. On the other hand, in the small-gap case ($C/d = 0.25$), the negative vortices are large and occupy almost the entire region, which lead to the strong backward sweep motions of fluid near the bottom wall.

(3) In the large-gap case, the mean streamwise velocity profile fluctuates again after being smoothed. This is attributed to the migration of the negative and positive vortices along the wall-normal direction. In the small-gap case, the backward sweep motions of fluid induced by the large negative vortices reduce the velocity near the bottom wall hence the skin friction in comparison with the large-gap case.

(4) The thermal boundary layer in the small-gap case is strongly suppressed by the large negative vortices. This results in the larger temperature gradient and more active heat transfer in comparison with the large-gap case. These indicate that careful design is required to enhance heat transfer in a boundary layer by utilizing a wake of a square bar.

Chapter 6

Conclusions

6.1 Summary

In this research, the effects of three types of disturbances on the development of a boundary layer with heat transfer are investigated by means of three-dimensional direct numerical simulation (DNS). The major findings are summarized below.

The effects of internal disturbance generated by a tripping object mounted on the wall are discussed in Chapter 3. The tripping object in this case contains nine small cubes which are placed on the wall alternatively in the spanwise direction. It is found that:

- The boundary layer has been triggered by the tripping object and the flow in this boundary layer is to some extent transitional;

- The effect of the tripping object on the development of the boundary layer is weak, especially in the downstream region. Only small-amplitude fluctuations are generated in the vicinity of the tripping object and the flow in the downstream region has a laminar-like structure;

- Heat transfer is slightly enhanced by the tripping object, and there is almost no effect on the skin friction;

- In the upstream region, the hairpin-like structure induced by the tripping object is visible. In the downstream region, on the other hand, the longitudinal structures are prevalent.

The effects of external disturbance generated by a regular grid are discussed in Chapter 4. Such grid turbulence has a turbulence intensity of 50% at the beginning, and is nearly homogeneous and isotropic. It is shown that:

- The boundary layer is triggered by the regular grid and the boundary layer flow becomes the turbulent state even though Re_θ is low;

● Skin friction and heat transfer in the boundary layer are more enhanced by the grid turbulence;

● Strong strain in the viscous sublayer, which is induced by the vortical motion in the buffer layer, contributes to the enhancement of heat transfer.

The effects of external disturbance generated by a wake of a square bar with different gaps are discussed in Chapter 5. The axis of the square bar is parallel to the bottom wall and normal to the flow direction. It is known that:

● The boundary layers have been triggered by the wakes of the square bar and the flows in these boundary layers are to some extent transitional;

● In the large-gap case, the alternating negative and positive vortices, shed from the bar, perturb the boundary layer by advecting the fluid wallward and outward in turn. On the other hand, in the small-gap case, the negative vortices are large and occupy almost the entire region, which lead to the strong backward sweep motions of fluid near the bottom wall;

● In the large-gap case, the mean streamwise velocity profile fluctuates again after being smoothed. This is attributed to the migration of the negative and positive vortices along the wall-normal direction. In the small-gap case, the backward sweep motions of fluid induced by the large negative vortices reduce the velocity near the bottom wall hence the skin friction in comparison with the large-gap case;

● The thermal boundary layer in the small-gap case is strongly suppressed by the large negative vortices. This results in the larger temperature gradient and more active heat transfer in comparison with the large-gap case.

A comparison of the main effects of these three types of disturbances mentioned above is summarized in Table 6.1. On the basis of these major findings, the following conclusions can be made.

(1) The boundary layer affected by the grid turbulence has been developed into turbulent state even though Re_θ is low, while the boundary layer flows are still in transition under the effects of the tripping object and the wake of a square bar.

(2) The effect of the tripping object on skin friction and heat transfer in a boundary layer is relative small. They are most enhanced by the grid turbulence. On the other hand, the effect of the wake of a square bar varies with the gap between the square

bar and the bottom wall. Skin friction is reduced but heat transfer is more active in the small-gap case, while they are both reduced in the large-gap case.

(3) In the case with the grid turbulence, strong strain in the viscous sublayer, which is induced by the vortical motion in the buffer layer, contributes to the enhancement of heat transfer. On the other hand, in the case with a wake of a square bar (small-gap case), the active heat transfer is attributed to the large negative vortices shed from upper side of the square bar.

(4) From the viewpoints of heat transfer enhancement and skin friction reduction in a boundary layer, it is preferred to utilize a wake of a square bar with small gap between it and the bottom wall.

Table 6.1 A comparison of the main effects of three types of disturbances
$\uparrow$: increase; $\downarrow$; decrease; $\rightarrow$: no significant effect (compared to a pure laminar boundary layer).

	Tripping object	Grid turbulence	Wake of a square bar	
			Small gap	Large gap
Boundary layer state	Transitional	Turbulent	Transitional	
Skin friction	$\rightarrow$	$\uparrow\uparrow$	$\downarrow$	$\downarrow$
Heat transfer	$\rightarrow$	$\uparrow\uparrow$	$\uparrow$	$\downarrow$

6.2 Further Work

The main aims of this research have been achieved. The boundary layer development as well as heat transfer strongly depends on the way that it is triggered. Particularly for engineering applications, careful design is required to control the boundary layer and enhance heat transfer by utilizing various disturbances. In the future, the following efforts can be made to develop this research further.

(1) To study the boundary layer flow with higher Reynolds number under the effects of various disturbances and combine numerical simulations with experimental studies.

(2) To study the effects of disturbances generated by different objects from the current research, i.e. the internal disturbance generated by several arrays of rod mounted on the wall, and the external disturbances generated by a fractal grid and a wake of a square bar with its axis normal to the bottom wall.

(3) To study the effects of the tripping object, the regular grid and the square bar, which are used in current research, by varying the size of them to obtain an optimal size for design.

Acknowledgements

My deepest gratitude goes first and foremost to Professor Yasuhiko Sakai and Associate Professor Kouji Nagata, my supervisors, for their guidance on this thesis. Their instructive advice and useful suggestions are very helpful for improving this thesis.

My grateful thanks also go to Associate Professor Yasumasa Ito, who has walked with me through the research and provided me with patient instruction and valuable comments.

I also express my heartfelt thanks to Professor Hiroshi Yamashita and Professor Norihiko Yoshikawa for their careful review and valuable comments with regard to this thesis. Those comments are very helpful for revising and improving this thesis, as well as the important guiding significance to my researches.

Part of the work was carried out under the Collaborative Research Project of the Institute of Fluid Science, Tohoku University. Their support in the use of their computational resources is greatly appreciated. Special thanks go to Dr. Hiroki Suzuki, Dr. Tomoaki Watanabe and Mr. Yi Zhou for their help in the numerical simulation.

I am also grateful to my beloved family for their encouragement and support all the time.

References

(1) Kim, J., Moin, P. and Moser, R., Turbulence statistics in fully developed channel flow at low Reynolds number, *J. Fluid Mech.*, Vol. 177, pp. 133-166, 1987.

(2) Splart, K., Direct simulation of a turbulent boundary layer up to $R_\theta = 1410$, *J. Fluid Mech.*, Vol. 187, pp. 61-98, 1988.

(3) Robinson, S. K., Coherent motions in the turbulent boundary layer, *Annu. Rev. Fluid Mech.*, Vol. 23, pp. 601-639, 1991.

(4) Kong, H., Choi, H. and Lee, J. K., Direct numerical simulation of turbulent thermal boundary layer, *Phys. Fluids*, Vol. 12, No. 10, pp. 2555-2568, 2000.

(5) Adrian, R. J., Hairpin vortex organization in wall turbulence, *Phys. Fluids*, Vol. 19, 041301, 2007.

(6) Hattori, H., Houra, T. and Nagano, Y., Direct numerical simulation of stable and unstable turbulent thermal boundary layer, *Int. J. Heat Fluid Flow*, Vol. 28, pp. 1262-1271, 2007.

(7) Li, Q., Schlatter, P., Brandt, L. and Henningson, D. S., DNS of a spatially developing turbulent boundary layer with passive scalar transport, *Int. J. Heat Fluid Flow*, Vol. 30, pp. 916-929, 2009.

(8) Lee, J. H. and Sung, H. J., Direct numerical simulation of a turbulent boundary layer up to $Re_\theta = 2500$, *Int. J. Heat Fluid Flow*, Vol. 32, pp. 1-10, 2011.

(9) Ovchinnikov, V., Choudhari, M. M. and Piomelli, U., Numerical simulations of boundary-layer bypass transition due to high-amplitude free-stream turbulence, *J. Fluid Mech.*, Vol. 613, pp. 135-169, 2008.

(10) Klebanoff, P. S., Tidstrom, K. D. and Sargent, L. M., The three-dimensional nature of boundary-layer instability, *J. Fluid Mech.*, Vol. 12, pp. 1-374, 1962.

(11) Knapp, C. F. and Roache, P. J., A combined visual and hot-wire anemometer

investigation of boundary-layer transition, *AIAA J.*, Vol. 6, pp. 29-36, 1968.

(12) Schlichting, H., *Boundary-layer theory*, McGraw-Hill, New York, 1979.

(13) Herbert, T., Secondary instability of boundary layer, *Ann. Rev. Fluid Mech.*, Vol. 20, pp. 487-526, 1988.

(14) Brandt, L., Schlatter, P. and Henningson, D. S., Transition in boundary layers subject to free-stream turbulence, *J. Fluid Mech.*, Vol. 517, pp. 167-198, 2004.

(15) Klebanoff, P. S., Effects of free-stream turbulence on a laminar boundary layer, *Bull. Am. Phys. Soc.*, Vol. 10, 1323, 1971.

(16) Kendall, J. M., Experimental study of disturbances produced in a pre-transitional laminar boundary layer by weak free stream turbulence, *AIAA paper*, 1695, 1985.

(17) Westin, K. J. A., Boiko, A. V., Klingmann, B. G. B, Kozlove, V. V. and Alfredsson, P. H., Experiments in a boundary layer subjected to free stream turbulence. Part 1. Boundary layer structure and receptivity, *J. Fluid Mech.*, Vol. 281, pp. 193-218, 1994.

(18) Andersson, P., Berggern, M. and Henningson, D. S., Optimal disturbances and bypass transition in boundary layers, *Phys. Fluids*, Vol. 11, pp. 134-150, 1999.

(19) Luchini, P., Reynolds-number independent instability of the boundary layer over a flat surface. Part 2. Optimal perturbations, *J. Fluid Mech.*, Vol. 404, pp. 289-309, 2000.

(20) Matsubara, M. and Alferdsson, P. H., Disturbance growth in boundary layers subjected to free-stream turbulence, *J. Fluid Mech.*, Vol. 430, pp. 149-168, 2001.

(21) Zaki, T. A. and Durbin, P. A., Mode interaction and the bypass transition, *J. Fluid Mech.*, Vol. 531, pp. 85-111, 2005.

(22) Brandt, L. and de Lange, H. C., Streak interaction and breakdown in boundary layer flows, *Phys. Fluids*, Vol. 20, pp. 1-16, 2008.

(23) Reiss, L. P. and Hanratty, T. J., An experimental study of the unsteady nature of the viscous sublayer, *AIChE J.*, Vol. 9, pp. 154-160, 1963.

(24) Kline, S. J., Reynolds, W. C., Schraub, F. A. and Runstadler, P. W., The structure of turbulent boundary layer, *J. Fluid Mech.*, Vol. 30, pp. 741-773, 1967.

(25) Smith, C. R. and Metzler, S. P., The characteristics of low-speed streaks in the near-wall region of a turbulent boundary layer, *J. Fluid Mech.*, Vol. 129, pp. 27-54, 1983.

(26) Chernyshenko, S. I. and Baig, M. F., The mechanism of streak formation in near-wall

turbulence, *J. Fluid Mech.*, Vol. 544, pp. 99-131, 2005.

(27) Corino, E. R. and Brodkey, R. S., A visual investigation of the wall region in turbulent flow, *J. Fluid Mech.*, Vol. 37, pp. 1-30, 1969.

(28) Kim, H. T., Kline, S. J. and Reynolds, W. C., The production of turbulent near a smooth wall in a turbulent boundary layer, *J. Fluid Mech.*, Vol. 50, pp. 133-160, 1971.

(29) Grass, A. J., Structural features of turbulent flow over smooth and rough boundaries, *J. Fluid Mech.*, Vol. 50, pp. 233-255, 1971.

(30) Davisdon, P. A., *Turbulence: An introduction for scientists and engineers*, Oxford University Press, UK, 2004.

(31) Theodorsen, T., Mechanism of turbulence, *Proc. Midwest. Conf. Fluid Mech., Ohio, Columbus*, pp. 1-18, 1952.

(32) Hinze, J. O., *Turbulence*, McGraw-Hill, New York, 1975.

(33) Morkovin, M. V., Reshotko, E. and Herbert, T., Transition in open flow system-a reassessment, *Bull. APS*, Vol. 39, No. 9, 1882, 1994.

(34) Saric, W. S., Reed, H. L. and Kerschen E. J, Boundary layer receptivity to freestream disturbances, *Annu. Rev. Fluid. Mech.*, Vol. 34, pp. 291-319, 2002.

(35) Fransson, J. H. M., Matsubara, M. and Alfredsson, P. H., Transition induced by free stream turbulence. *J. Fluid Mech.*, Vol. 527, pp. 1-25, 2005.

(36) Shahinfar, S. and Fransson, J. H. M., Effect of free-stream characteristics on boundary layer transition, *J. Phys.: Conference Series*, Vol. 318, 032019, 2011.

(37) Charnay, G., Mathieu, J. and ComteBellto, G., Response of a turbulent boundary layer to random fluctuation in the external stream, *Phys. Fluids*, Vol. 19, pp. 1261-1272, 1976.

(38) Hancock, P. E. and Bradshaw, P., Turbulent structure of a boundary layer beneath a turbulent free stream, *J. Fluid Mech.*, Vol. 205, pp. 45-76, 1989.

(39) Sharp, N. S., Neuscamman, S. and Warhsft, Z., Effects of large-scale free stream turbulence on a turbulent boundary layer, *Phys. Fluids*, Vol. 21, 095105, 2009.

(40) Nagata, K., Sakai, Y. and Komori, S., Effects of small-scale freestream turbulence on turbulent boundary layers with and without thermal convection, *Phys. Fluids*, Vol. 23, 065111, 2011.

(41) Maciejewski, P. K. and Moffat, R. J., Heat transfer with very high free-stream

turbulence: Part I - Experimental data, *J. Heat Transfer*, Vol. 114, pp. 827-833, 1992.

(42) Maciejewski, P. K. and Moffat, R. J., Heat transfer with very high free-stream turbulence: Part II - Analysis of the results, *J. Heat Transfer*, Vol. 114, pp. 834-839, 1992.

(43) Péneau, F., Boisson, H. C. and Djilali, N., Large eddy simulation of the influence of high free-stream turbulence on a spatially evolving boundary layer, *Int. J. Heat Fluid Flow*, Vol. 21, pp. 640-647, 2000.

(44) Kondjoyan, A., Péneau, F. and Boisson, H. C., Effects of high free stream turbulence on heat transfer between plates and air flows: a review of existing experimental results, *Int. J. Therm. Sci.*, Vol. 41, pp. 1-16, 2002.

(45) Li, Q., Schlatter, P. and Henningson, D. S., Simulations of heat transfer in a boundary subject to free-stream turbulence, *J. Turbulence*, Vol. 11, pp. 1-33, 2010.

(46) Squire, L. C., Interactions between wakes and boundary layers, *Prog. Aerospace Sci.*, Vol. 26, pp. 261-288, 1989.

(47) Kyriakides, N. K., Kastrinakis, E. G., Nychas, S. G. ans Goulas, A., Prediction of boundary layer transition induced by a Von Karman vortex street wake, *J. Aerosp. Eng.*, Vol. 210, pp. 167-179, 1996.

(48) Ovchinnikov, V., Piomelli, U. and Choudhari, M. M., Numerical simulations of boundary-layer transition induced by a cylinder wake, *J. Fluid Mech.*, Vol. 547, pp. 413-441, 2006

(49) Marumo, E., Suzuki, K. and Sato, T., A turbulent boundary layer disturbed by a cylinder, *J. Fluid Mech.*, Vol. 87, pp. 121-141, 1978.

(50) Marumo, E., Suzuki, K. and Sato, T., Turbulent heat transfer in a flat plate boundary layer disturbed by a cylinder, *Int. J. Heat Fluid Flow*, Vol. 6, pp. 241-248, 1985.

(51) Suzuki, H., Suzuki, K. and Sato, T., Dissimilarity between heat and momentum transfer in a turbulent boundary layer disturbed by a cylinder, *Int. J. Heat Mass Transfer*, Vol. 31, pp. 259-265, 1988.

(52) de Souza, F., Delville, J., Lewalle, J. and Bonnet, J. P., Large scale coherent structures in a turbulent boundary layer interacting with a cylinder wake, *Exp. Therm. Fluid Sci.*, Vol. 19, pp. 204-213,1999.

(53) Baskaran, V. and Bradshaw, P., Effect of bluff body wakes on skin friction and surface

heat transfer in a turbulent boundary layer, *J. Wind Eng. Ind. Aerod.*, Vol. 49, pp. 269-278, 1993.

(54) Trigui, T. and Guezennec, Y. G., Heat transfer reduction in manipulated turbulent boundary layers, *Int. J. Heat Fluid Flow*, Vol. 11, No. 3, pp. 214-219, 1990.

(55) Inaoka, K., Kigawa, H., Suzuki, H. and Suzuki, K., Heat transfer in a turbulent boundary layer with an insertion of a LEBU plate, *Trans. JSME, Series B*, Vol. 57, No. 537, pp. 210-215, 1991 (in Japanese).

(56) Hamdouni, A. and Bonnet, J. P., Effect of external manipulators on the heat transfer on a flat plate turbulent boundary layer, *Appl. Sci. Res.*, Vol. 50, pp. 369-385, 1993.

(57) Erm, L. P. and Joubert, P. N., Low-Reynolds-number turbulent boundary layers, *J. Fluid Mech.*, Vol. 230, pp. 1-44, 1991.

(58) Rizzetta, D. P. and Visbal, M. R., Direct numerical simulations of flow past an array of distributed roughness elements, *AIAA J.*, Vol. 45, pp. 1967-1976, 2007.

(59) Schlatter, P. and Örlü, R., Turbulent boundary layers at moderate Reynolds numbers: inflow length and tripping effects, *J. Fluid Mech.*, Vol. 710, pp. 5-34, 2012.

(60) Raupach, M. R., Antonia, R. A. and Rajagopalan, S., Roughness-wall turbulent boundary layers. *Appl. Mech. Rev.*, Vol. 44, pp. 1-25, 1991.

(61) Krogstad, P. A. and Antonia, R. A., Surface roughness effects in turbulent boundary layers, *Exps. Fluids*, Vol. 27, pp. 450-460, 1999.

(62) Lee, S. H. and Sung, H. J., Direct numerical simulation of the turbulent boundary layer over a rod-roughened wall, *J. Fluid Mech.*, Vol. 584, pp. 125-146, 2007.

(63) Friedrich, R., Hüttl, T. J., Manhart, M. and Wangner, C., Direct numerical simulation of incompressible turbulent flows, *Comput. Fluids*, Vol. 30, pp. 55-579, 2001.

(64) Moin, P., *Fundamentals of engineering numerical analysis*, Cambridge University Press, USA, 2010.

(65) Lele, S. K., Compact finite difference schemes with spectral-like resolution, *J. Comput. Phys.*, Vol. 10, pp. 16-42, 1992.

(66) Morinishi, Y., Lund, T. S., Vasilyev, O. V. and Moin, P., Fully conservative higher order finite difference schemes for incompressible flow, *J. Comput. Phys.*, Vol. 143, pp. 90-124, 1998.

(67) Kajishima T., Finite-difference method for convective terms using non-uniform grid,

Trans. JSME, Series B, Vol. 65, pp. 1607-1612, 1999 (in Japanese).

(68) Le, H. and Moin, P., An Improvement of fractional step methods for the incompressible Navier-Stokes equations, *J. Comput. Phys.*, Vol. 92, pp. 369-379, 1991.

(69) Van Der Vorst, H. A., Bi-CGstab: A fast and smoothly converging variant of Bi-CG for the solution of nonsymmetric linear system, *SIAM J. Sci. Stat. Comput.*, Vol. 13, pp. 631-644, 1992.

(70) Fathali, M., Klein, M., Breckhoven, T., Lacor, C. and Baelmans, M., Generation of turbulent inflow and initial conditions based on multi-correlated random fields, *Int. J. Numer. Meth. Fluids*, Vol. 57, pp. 93-117, 2008.

(71) Klein, M., Sadiki, A. and Janicka, J., A digital filter based generation of inflow data for spatially developing direct numerical or large eddy simulation, *J. Comput. Phys.*, Vol. 186, pp. 652-665, 2003.

(72) Kempf, A., Klein, M. and Janicka, J., Efficient generation of initial- and inflow-conditions for transient turbulent flows in arbitrary geometries, *Flow, Turbul. Combust.*, Vol. 74, pp. 67-84, 2005.

(73) Lee, S., Lele, SK. and Moin, P., Simulation of spatially evolving compressible turbulence and application of Taylors hypothesis, *Phys. Fluids A*, Vol. 4, pp. 1521-1530, 1992.

(74) Lund, T. S., Wu, X. and Squires, K. D., Generation of turbulent inflow data for spatially-developing boundary layer simulations, *J. Comput. Phys.*, Vol. 140, pp. 233-258, 1998.

(75) Xia, S., Ito, Y., Nagata, K., Sakai, Y., Suzuki, H., Terashima, O. and Hayase, T., DNS study on the development of boundary layer with heat transfer under the effects of external and internal disturbances, *J. Fluid Sci. Tech.*, Vol. 9, pp. 1-13, 2014.

(76) Grötzbach, G., Spatial resolution requirements for direct numerical simulation of the Rayleigh-Bénard convection, *J. Comput. Phys.*, Vol. 49, pp. 241-264, 1983.

(77) Nagata, K., Suzuki, H., Sakai, Y. and Hayase, T., Direct numerical simulation of turbulence with scalar transfer around complex geometries using the immersed boundary method and fully conservative higher order finite difference schemes, *Numerical Simulations - Examples and Applications in Computational Fluid*

Dynamics, edited by Angermann, L., INTECH, pp. 39-62, 2010.

(78) Suzuki, H., Nagata, K., Sakai, K., Hayase, T. Hasegawa, Y. and Ushijima, T., An attempt to improve accuracy of higher-order statistics and spectra in direct numerical simulation of incompressible wall turbulence by using the compact schemes for viscous terms, *Int. J. Numer. Meth. Fluids*, Vol. 73, pp. 509-522, 2013.

(79) Chauhan, K. A., Monkewitz, P. A. and Nagib, H. M., Criteria for assessing experiments in zero pressure-gradient boundary layers, *Fluid Dyn. Res.*, Vol. 41, 021404, 2009.

(80) Wu, X. H. and Moin, P., Direct numerical simulation of turbulence in a nominally zero-pressure-gradient flat-plate boundary layer, *J. Fluid Mech.*, Vol. 63, pp. 5-41, 2009.

(81) Schrader, L. U., Amin, S. and Brandt, L., Transition to turbulence in the boundary layer over a smooth and rough swept plate exposed to free-stream turbulence, *J. Fluid Mech.*, Vol. 646, pp. 297-325, 2010.

(82) Nolan, K. P., Walsh, E. J. and Mceligot, D. M., Quadrant analysis of a transitional boundary layer subject to free-stream turbulence, Journal of Fluid Mechanics, Vol. 658, pp. 310-335, 2010.

(83) Wu, X. and Durbin, P. A., Numerical simulation of heat transfer in a transitional boundary layer with passing wakes, Transactions of the ASME, Journal of Heat Transfer, Vol.122, pp. 248-257, 2000.

(84) Chen, C. P. and Blackwelder, R. F., Large-scale motion in a turbulent boundary layer: A study using temperature contamination, *J. Fluid Mech.*, Vol. 89, pp. 1-31, 1978.

(85) Holman, J. P., *Heat transfer*, McGraw-Hill, 1997.

(86) Xia, S., Ito, Y., Nagata, K., Sakai, Y., Suzuki, H., Terashima, O., Hayase, T., Study on the effects of grid-generated turbulence on the initial growth of boundary layer by direct numerical simulation, *Proc. 4th Int. Conf. on Jets, Wakes and Separated Flows, Nagoya, Japan*, paper No. 1169, 2013.

(87) Xia, S., Ito, Y., Nagata, K., Sakai, Y., Suzuki, H., Terashima, O., Hayase, T., DNS study on boundary layer with heat transfer affected by disturbances created by a grid and small cubes, *Proc. 10th Int. Conf. on Flow Dyn., Sendai, Japan*, pp. 128-129, 2013.

(88) Tennekes, H and Lumley, J. L., *A first course in turbulence*, The MIT press, 1997.

(89) Oberlack, M., On the decay exponent of isotropic turbulence, *PAMM Proc. Appl. Math. Mech.*, Vol. 1, pp. 294-297, 2002.

(90) Osaka, H., Kameda, T., and Mochizuki, S., Local skin friction coefficient evaluated by direct measurement method and mean flow quantities in a turbulence boundary layer, *Trans. JSME, Series B*, Vol. 62, pp. 138-145, 1996 (in Japanese).

(91) Xia, S., Ito, Y., Nagata, K., Sakai, Y. and Hayase, T., Numerical study on a boundary layer with heat transfer affected by a wake of a square bar, *J. Fluid Sci. Tech.*, 2014, accepted.

(92) Suzuki, H., Inoue, Y., Nishimura, T., Fukutani, K. and Suzuki, K., Unsteady flow in a channel obstructed by a square rod (crisscross motion of vortex), *Int. J. Heat and Fluid Flow*, Vol. 14, pp. 2-9, 1993.

(93) Suzuki, K. and Suzuki, H., Instantaneous structure and statistical feature of unsteady flow in a channel obstructed by a square rod, *Int. J. Heat and Fluid Flow*, Vol. 15, pp. 426-437, 1994.